Institute of Physics and Astronomy
Århus University
Ny Munkegade
8000 Århus C
Denmark

May 25, 1999

Master's thesis

β-delayed proton emission from ^{31}Ar

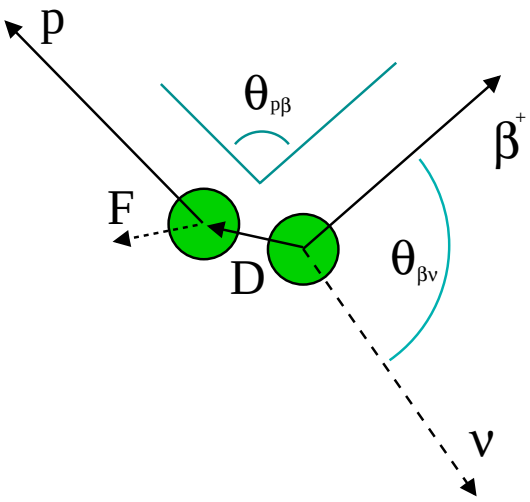

Supervisor: Karsten Riisager

John Thaysen

912459

May 25, 1999

Contents

Chapter 1

Introduction

This master's thesis is based on experimental studies of β-delayed protons from the nucleus ^{31}Ar. The experiment was performed at the ISOLDE facility at CERN.

The thesis contains three principal parts: A detailed examination of the detector-system, an investigation of the kinematic shift in β-delayed proton emission and an investigation of the β-delayed single proton emission of the nucleus ^{31}Ar.

If one wants to understand the output of a performed experiment, one has to know the experimental equipment well. In the experiment a double sided strip detector was used which provides accurate measurements of particle positions and good conditions for observations of multi-particle events. On the other hand, a strip detector also has some drawbacks, for instance interstrip losses. Phenomena as charge losses and charge sharing are both related to interstrip losses. These and other detector related issues will be discussed in chapter 3 and 4.

Since the detector-system is designed with a total solid angle of roughly 25% of 4π divided into 271 segments, it offers good conditions for observations of multi-particle events. The detector-system was actually designed for measurements of two proton coincidences. However, I had the idea to use the recorded data in an investigation of β-p coincidences.

The investigation performed on the β-p coincidences is a research of the kinematic shift of the protons emitted in β-delayed proton emission. The detector-system offers unique conditions for simultaneous measurements of the proton energy and the angle between the emitted proton and positron. This examination can be used to establish information about spin and isospin of the states involved. The study of the kinematic shift in β-delayed proton emission is given in chapter 5.

In chapter 6, the deduced half-lives of the three argon isotopes 31, 32 and 33 are presented. Last but not least, the experimental result of the decay of ^{31}Ar is

presented in chapter 7.

The nucleus ^{31}Ar is of great interest because it is a candidate for direct two-proton radioactivity and β-delayed simultaneous two-proton emission. None of these exotic decays have yet been observed, however β-delayed sequential two-proton emission and β-delayed single proton emission have been observed. In chapter 7, a decay scheme of β-delayed single proton emissions from ^{31}Ar is established. Moreover, the method described in chapter 5 is used in chapter 7 to deduce that the spin of the ground state of ^{31}Ar is equal to 5/2.

As the main achievement in this thesis I will emphasize the study of the kinematic shift in β-delayed proton emission. This investigation has led to a new method that I think will be very useful for assignments of spin, isospin and energy in the future.

In all formulas in this thesis I have used natural units, i.e. $c = \hbar = 1$, and vectors are boldfaced. I am thankful to my supervisor Karsten Riisager for good support during the preparation of this thesis and to Hans Otto Uldall Fynbo who has been like an assistant supervisor to me. I am also thankful to Anne Mette Holt for trying to improve my English grammar and for reading the proofs of this master's thesis.

The achieved results of the investigation of β-delayed two-proton emission of ^{31}Ar are in preparation for publication under the title: *"β-Delayed Particle Emission in the Decay of ^{31}Ar: The Mechanism of the Two-Proton Emission Resolved"* [1].

The investigation presented in this thesis of the kinematic shift in β-delayed proton emission are in preparation for publication under the title: *"Determination of the Spin of ^{31}Ar"* [2].

Chapter 2

The decay of exotic nuclei

2.1 Nuclear halos

Progress in the development of techniques in producing exotic nuclei have resulted in interesting new phenomena of nuclear structure, for instance the nuclear halo [3, 4, 5]. For loosely bound systems the mean radius will in general increase when the separation energy of the outermost nucleon(s) is(are) decreasing*. These large nuclei are called halo nuclei. At the present, ^{11}Li and ^{11}Be are the most carefully studied and the most distinct nuclear halos. Other neutron halo candidates are ^{6}He, ^{14}Be, ^{17}B and ^{19}C. The simplest example of a halo nucleus is ^{11}Be which to a good approximation may be considered as a two-body system consisting of a neutron coupled to the ^{10}Be core. If we approximate the interaction potential between the neutron and the core as a square well potential, the wavefunction of the s state will drop exponentially outside the core radius $r > R$: $\psi(r) = A\exp(-\kappa r)/r$, where A and κ are constants. The calculation showing this result is a classical exercise in quantum mechanics†, and one finds that κ is given by $\kappa = \sqrt{2\mu E_s}/\hbar$, where E_s is the neutron separation energy. This proves that the halo tail increases when the separation energy decreases. A more advanced deduction illustrates that the rms radius only diverge in the limit of vanishing separation energy E_s for low angular momentum ($l = 0, 1$), i.e. the large halos are expected to have low angular momentum [4].

The most frequently observed halo nuclei have a pair of neutrons in their halos. The most carefully studied case is the two-neutron halo of ^{11}Li. These two-neutron

*This is a very general fact, also known in atomic physics, e.g. negative ions.

†Used on the deuteron, to show that it has a large rms neutron-proton distance on about 4 fm.

halos have received much attention, especially as a test for the theoretical predictions for three-body systems. Since ^{10}Li is unbound, it is essential that the two neutrons are very correlated to bind ^{11}Li. This means that pure shell model states cannot explain these so-called Borromean halo nuclei.

A related subject is proton halos, ^{8}B and ^{17}F are two possible proton halo nuclei. So far, no proton halo has been observed with the same certainty as the neutron halos. This is because of the repulsive Coulomb interaction. The Coulomb potential has a long range ($1/r$), and the wavefunction is therefore very confined. As a consequence of the Coulomb barrier, all radial moments remain finite for all positive separation energies. This means that proton halos are not expected to have the same large radii as neutron halos*.

The observation of β-delayed particle emission from nuclear halos is another interesting phenomenon. Many different kinds of decays have been observed, e.g. β-delayed deuteron, triton, neutron, two-neutron and three-neutron emission. These decays have raised new interesting questions, and some of these have not yet been answered. For instance, how correlated are the two neutrons in a β-delayed two-neutron decay? Do the observations of two-particle emission give us new knowledge of the pairing interaction and the nuclear structure? Can the relatively decoupled structure of the halo and the core in the halo nucleus allow separate decay of core and halo? No adequate answers have yet been delivered to these questions.

With the aim to answer some of these questions one looks after parallel cases in proton-rich nuclei. Protons have the advantage that they have charge, which makes them much easier to detect than neutrons.

2.2 Two proton emission

Two-proton emission is either sequential or direct, which means the two protons are either emitted stepwise or simultaneously. Already in 1960, two-proton radioactivity† was suggested by Gol'danskii [6] as a possible exotic decay of proton-rich nuclei. A nucleus with an even number of protons (Z) may, as a consequence of the pairing force, be more tightly bound than the nucleus with one proton less. This would make it possible to find an even Z nucleus with a neutron deficit that is two-proton emission unstable but single proton emission stable. The direct two-proton emission has theoretically been described in two different ways. In the

*See the overview articles [3, 4, 5] and references therein for more details.

†Also called diproton emission, i.e. a kind of direct two-proton emission.

traditional diproton model, the two-protons are emitted in a ^{1}S state of ^{2}He which subsequently breaks up into two protons. In that model, the decay is thought of as a resonantly enhanced decay through the intermediate state ^{1}S of ^{2}He.

The other model is a simultaneous two-proton emission also called "democratic" emission. This model implies that the decay is a direct three-body breakup, and not a sequential decay as in the first model mentioned. The main difference between these two models is that in the latter the two protons do not have to be in a ^{1}S state.

Mass measurement of light nuclei indicates that ^{6}Be, ^{12}O and ^{16}Ne are ground-state two-proton emitters [7]. This means they are two-proton emission unstable but one proton emission stable. There is only one problem: In all three cases the width of the ground state and the width of the ground state of the one-proton daughter is known to be relatively large ($\sim$ 1 MeV). Consequently, the decay can happen by sequential two-proton emission through the tail of the ground state of the one-proton daughter, in spite of the fact that one-proton emission is impossible.

The experimental study of ^{12}O [8, 9] shows no evidence for ^{2}He emission and it is most probably a sequential two-proton decay. In the case of ^{6}Be [10], the result shows only a little probability for ^{2}He emission.

Further experiments are needed before the direct two-proton decay can be fully understood, but the model of simultaneous two-proton emission seems to be the best to describe the still very uncertain experimental fact of direct two-proton emission. Therefore, one seeks nuclei that are two-proton unstable but single proton stable, and have longer lifetimes. In the region Z=13-20, the nuclei ^{22}Si, ^{31}Ar and ^{34}Ca are predicted to have these features [11, 12]. It is still unconfirmed experimentally that ^{31}Ar should be two-proton radioactive, but even if it is two-proton radioactive the probability of observing two-proton radioactivity is very small because of the low Q-value.

Since the observation of β-delayed two-neutron emission in ^{11}Li in 1979 [13], β-delayed two-neutron emission has been observed in many other nuclides. As a consequence of these observations, β-delayed two-proton decay was predicted by Gol'danskii [14] as a mirror-process to the neutron case. Once again, ^{31}Ar was predicted to be a good candidate for this process, which is fully confirmed in the experiments [15, 16, 17, 18, 19, 20, 21]. Since the first observation in 1983 of β-delayed two-proton emission from the precursor ^{22}Al [22], β-delayed two-proton emission has been observed in many nuclides, e.g. ^{22}Al, ^{23}Si, ^{26}P, ^{27}S, ^{31}Ar, ^{35}Ca, ^{39}Ti and ^{43}Cr. See Blank *et al.* (1997) [23] and references therein.

Figure 2.1 is an illustration of the possible two-proton emissions of nuclei that

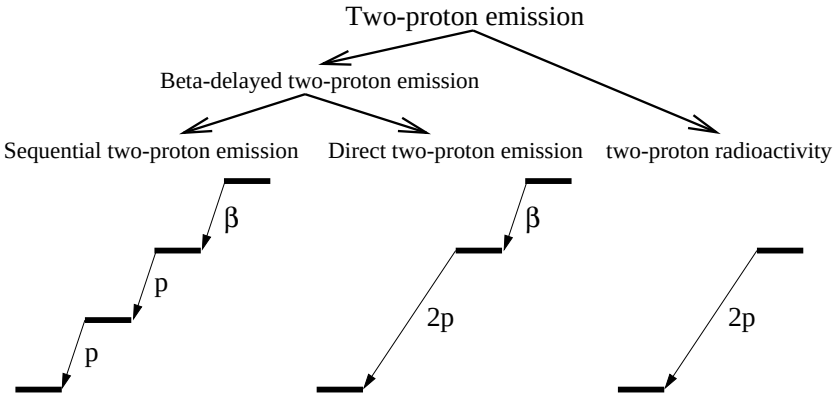

Figure 2.1: An illustration of the possible two-proton emissions of nuclei stable to single proton emission.

are stable to single proton emission. The two-proton radioactivity has already been discussed. The β-delayed two-proton emission is observed in many different kinds of nuclides. In a sequential emission, the decay involves an intermediate state. Sequential two-proton emission can be identified by looking at the width of the proton peaks. The first emitted proton has a narrow linewidth, while the second is Doppler broadened because the one-proton daughter nucleus is in motion as a consequence of the recoil from the first proton. The most interesting cases are β-delayed simultaneous two-proton emission. Until now, there is no evidence for these processes. A reason for this is that after the β-decay the daughter nucleus is often in an excited state, which means there is probably an intermediate state in the one-proton daughter through which a sequential two-proton emission can take place. Sequential two-proton emission is therefore the dominating decay channel of β-delayed two-proton emission, and still the only one observed experimentally.

In trying to distinguish between the three different models of two-proton emission, one has measured the two-proton angular correlation [24]. Moreover, on the basis of these measurements one has tried to make spin assignments of the states involved. This method has yet not been very successful, even in our new experiment where the detector setup is constructed for such an investigation we observe only isotropic distributions which confirms the sequential structure of the two-proton emission. Furthermore, it has not been possible to use this method for spin assignment of the states involved [1].

However, by measuring the kinematic shift of β-delayed protons it is possible to make spin and isospin assignments of the states involved. This will be proven in chapter 5, and in chapter 7 the method will be used on the ground state of ^{31}Ar.

2.3 The β-ν angular correlation

The β-ν angular correlation is described in details in chapter 5, only a brief introduction is given here. An experimental determination of the β-ν angular correlation can be used to establish the relative contributions of Gamow-Teller and Fermi matrix elements to a particular transition. Moreover, it can be used as a test of the charged weak current which, according to the Standard Model, has a V-A form.

Since neutrinos are nearly undetectable, they are unobserved in any experiment measuring the β-ν angular correlation. One is therefore forced to use other more sophisticated techniques, wherein one indirectly observes the β-ν angular correlation. This can for instance be done by measuring the recoil of the daughter nucleus, which for instance was done by Johnson *et al.* [25] and Allen *et al.* [26].

However, this technique is very limited because the amount of energy delivered to the daughter nucleus is rather small, and one can therefore only use gaseous sources in which possible scattering with the source material is strongly reduced.

It is planned to use magneto-optical traps on β-decaying nuclei to measure both position and energy of the emitted β-particle and of the recoiling daughter nucleus [27]. Such an experiment would make it possible to calculate the direction and amplitude of the neutrino momentum. However, this method has to my knowledge still not given any results of the β-ν angular correlation, and low statistics is expected.

The phenomenon of β-delayed particle emission provides a second means of exploring the β-ν angular correlation*. If a particle is emitted in flight from the recoiling daughter nucleus, it will undergo a kinematic energy shift that reflects the motion of the daughter nucleus. One advantage of the β-delayed particle experiment is that energetic heavy particles are observed, in contrast to experiments where the recoiling daughter is directly detected.

In deducing the β-ν angular correlation in a β-delayed particle experiment, one can either study the recoil broadening of the β-delayed particles or measure β-p coincidences. In this thesis the last mentioned method will be used on ^{33}Ar and ^{32}Ar in chapter 5, and on ^{31}Ar in chapter 7. Moreover, the method I have used, will be explained in details in chapter 5.

*Measurements of β-γ angular correlation is a third method of exploring the β-ν angular correlation, e.g. Egorov *et al.* [28] and Bowers *et al.* [29].

2.4 The three argon isotopes

The knowledge found in previous experimental studies of β-delayed protons from the three argon isotopes 31, 32 and 33 is presented in this section. The ^{31}Ar isotope is of main interest, but we have also collected data of the two other isotopes.

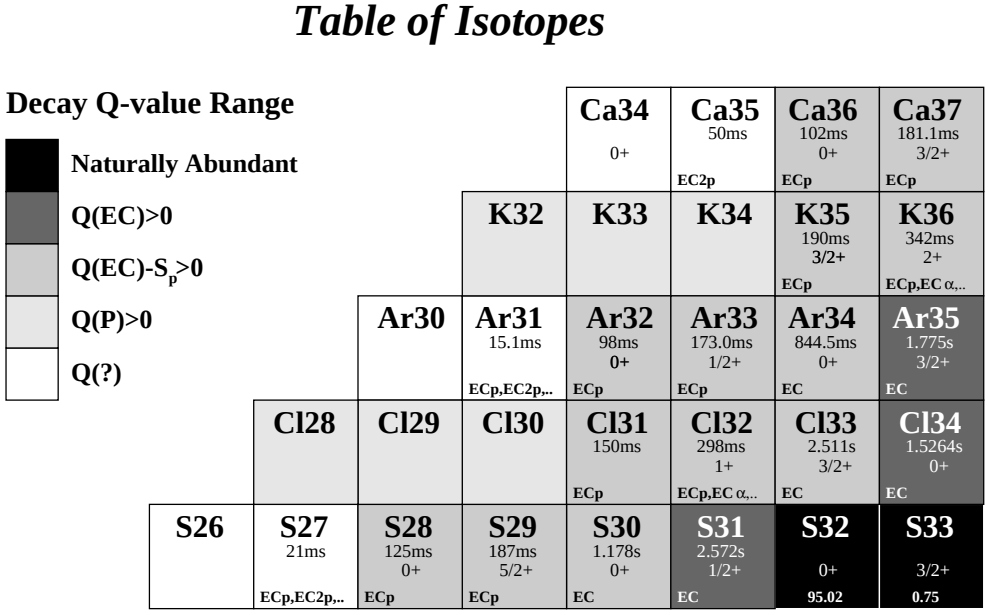

Figure 2.2: A region of the Tables of Isotopes [30].

Figure 2.2 illustrates a section of the table of isotopes including the three argon isotopes studied in this thesis. For each nuclide the half-life, the spin-parity assignment for the ground state and the main decay branches are shown.

Table 2.1: The isospin and proton separation energies of the argon isotopes

A no.	N no.	$N-Z$ no.	T	T_z	$T_{1/2}$ (ms)	$S(p)$ (keV)	$S(2p)$ (keV)	Q_{EC} (MeV)
31	13	-5	5/2	-5/2	15.1(12)[a]	406(75)[b]	−3(110)[c]	18.48(11)[c]
32	14	-4	2	-2	98(2)[d]	2400(70)[e]	2690(50)[e]	11.15(5)[e]
33	15	-3	3/2	-3/2	174.1(11)[f]	3340(30)[e]	4910(30)[e]	11.62(3)[e]

[a] Bazin *et al.* (1992) [19]
[b] Cole (1998) [12]
[c] Axelsson *et al.* (1998) [20]
[d] Björnstad *et al.* (1985) [31]
[e] Audi and Wapstra (1993) [7]
[f] Borge *et al.* (1987) [32]

In table 2.1, the isospin, the half-life, the proton separation energy and the Q_{EC}-value are shown for each of the three isotopes. In the first three columns, the

number of nucleons (A), the neutron number (N) and the difference between the number of neutrons (N) and the proton number (Z) are displayed. In the next two columns, the isospin T and T_z are shown: $T_z = (N - Z)/2$ and T is equal to the absolute value of T_z for the nuclear ground states. The third column displays the half-lives and the fifth and sixth column display respectively the single proton and the double proton separation energy. In the last column, the Q-value for electron capture is shown*. Each of the isotopes will be examined in the following.

2.4.1 The case of ^{33}Ar

The isotope ^{33}Ar has $N - Z = 15 - 18 = -3$, i.e. it has isospin $T_z = (N - Z)/2 = -3/2$ and the ground state has $T = 3/2$. Mainly three experimental investigations of ^{33}Ar have been undertaken [32, 33, 34]. The half-life of ^{33}Ar is measured to 174.1(11) ms in [32] and 173(2) ms in [33]. The daughters after β-decay and β-delayed proton emission from ^{33}Ar are ^{33}Cl($T_{1/2} = 2.51s$) and ^{32}S(stable). Neither of these nuclides are precursors for β-delayed proton emission. Precise energy levels in ^{33}Cl were measured in [32, 33, 34] and the observations were repeated once again in [35]. In [34], precise measurements of the line broadening, caused by the β-ν recoil motion of the daughter nucleus, were used to obtain spectroscopic information about the transitions and the excited states involved.

In the investigation presented in this thesis, we have used two proton energies from the ^{33}Ar spectrum for the energy calibration. Furthermore, the three most clear proton lines in the ^{33}Ar spectrum are used as a test of the spectroscopic method given in chapter 5, and this test shows that for instance the energy level at 6.25 MeV in ^{32}Cl probably is a $1/2^+$ state. Finally, the half-life is deduced and presented in chapter 6.

2.4.2 The case of ^{32}Ar

β-delayed protons from ^{32}Ar were initially observed by Hagberg *et al.* (1977) [36]. In the first experiment, the Isobaric Analog State (IAS) was the only energy level observed in ^{32}Cl. The half-life was then deduced to be 75(50) ms. In 1985 a detailed study of the energy levels and the half-life were done by Björnstad *et al.* [31]. The new half-life measurement gave the value 98(2) ms. The spin assignments done in [31] was tested by the already mentioned method of β-ν recoil line broadening in Schardt and Riisager [34].

*Remember that $Q_{\beta^+} \cong Q_{EC} - 2\,m_e$, where m_e is the electron mass.

In the examination of ^{32}Ar, likewise the case of ^{33}Ar, we have used the three most clear lines in a test of the method of spin and isospin assignment outlined in chapter 5. Moreover, the half-life of ^{32}Ar is also measured.

2.4.3 The case of ^{31}Ar

As already explained in section 2.2, ^{31}Ar was and still is predicted to have a negative two proton separation energy but a positive one proton separation energy. Cole (1998) [12] estimates that S_p=406(75) keV and $S_{2p} = -277(126)$ keV. Different experimental groups started the investigation of ^{31}Ar hoping to observe a direct two-proton emission from ^{31}Ar.

In 1986, Langevin *et al.* [37] started experiments at GANIL on the proton drip-line $T_z = -5/2$ nuclei: ^{23}Si, ^{27}S, ^{31}Ar and ^{35}Ca. Shortly thereafter, the first investigation of β-delayed protons from ^{31}Ar was done at GANIL [15]. In this experiment the radioactive isotopes where implanted in a silicon detector. This silicon detector was part of a detector telescope that was used to detect β-delayed protons. In the first experiment, no evidence for β-delayed two-proton emission was found but β-delayed protons were observed and a half-life of 15(3) ms was deduced. From GANIL, two other experimental investigations of β-delayed protons from ^{31}Ar are published, one from 1991 by Borrel *et al.* [17] and the other from 1992 by Bazin *et al.* [19].

At CERN, the first experiment on ^{31}Ar was performed in 1991 by Borge et al. [18]. This experiment showed evidence for β-delayed two-proton emission. The experiment was repeated at CERN, and the results are published in Axelsson *et al.* [20, 21]. No evidence for direct two-proton decay of ^{31}Ar was observed, and an upper limit on the absolute branching ratio for direct two-proton emission was deduced to be 6.0×10^{-4}. This corresponds to a partial half-life of 25(3) s [20]. A calculation established on this result gives the following limit on the two-proton separation energy: $S_{2p} \geq -390$ keV [20].

At GANIL, the half-life of ^{31}Ar was measured to be 15(3) ms [17] and 15.1(12) ms [19]. In Borrel *et al.* [17], they observed β-delayed two-proton emission of ^{31}Ar, however Bazin *et al.* [19] claimed to have done the first observation of β-delayed three-proton emission. The three-proton emission of ^{31}Ar is not confirmed in any of the newer experiments, and an upper limit on the branching ratios for possible β-delayed three-proton branches is about 1.1×10^{-3} [38].

In all, three different groups have performed experiments on ^{31}Ar: The group at GANIL, the one at CERN and one at Berkeley. At Berkeley, an exotic experimental

equipment called a fast in-beam recoil catcher wheel was used to detect for instance β-delayed two-proton emission from ^{31}Ar [16]. Only very few β-delayed two-proton events from ^{31}Ar were observed at Berkeley. However, their experiment was the first small evidence of β-delayed two-proton emission of the precursor ^{31}Ar.

In the experiment by Axelsson *et al.* [20, 21], a detailed examination of the decay of ^{31}Ar was established. However, the β-delayed two-proton emission was not totally understood, and a decisive proof in favor of sequential β-delayed two-proton emission with respect to simultaneous β-delayed two-proton emission was not found. This was the main reason for repeating the experiment at CERN. The study of the two-proton and three-proton emission will be presented in the Ph.D. thesis of Hans Otto Uldall Fynbo.

In this thesis, the investigation of β-delayed single proton emission will be presented in chapter 7. The examination of β-delayed single proton emission is quite complicated when there is a background of β-delayed two-proton emission.

The decay scheme of β-delayed single proton emission will be constructed, and we will go through each kind of criteria used in the energy assignment. The method of measuring the kinematic energy shift of β-delayed proton emission will be used to show that the spin of the ground state of ^{31}Ar is $5/2^+$. Moreover, the same method will be used in spin assignments of states in ^{31}Cl in chapter 7, and in chapter 6 the half-life of ^{31}Ar will be derived.

Chapter 3

Experimental and analytical equipment

3.1 The ISOLDE-CERN facility

The experiment is performed at the ISOLDE facility at CERN. The facility is based on high-energy protons from the Proton-Synchrotron-Booster (PSB) which delivers proton pulses every 1.2 s with energy of 1 GeV. In one proton pulse there are 3.2×10^{13} protons and the pulse-length is 2.4 μs [39]. The protons are fired into a CaO-target where isotopes of various elements are produced. For instance, ^{31}Ar is most probably produced in the spallation reaction: ^{40}Ca+p$\rightarrow$^{31}Ar+3p+7n. The produced elements are transferred through a water-cooled line kept at 30°C, in this way only gases are admitted to the plasma ionization source [40]. Ions are produced by discharge ionization processes and are accelerated over a voltage gap of 60 kV to the General Purpose Separator (GPS). The ions are separated in the GPS by methods of magnetic mass-spectroscopy with a mass resolution given by $M/\Delta M = 2400$.

Before the ions reach the experimental hall, the beam passes through the so-called "switch-yard" which is used to switch the beam down the desired beam-line. The switching is performed by electrostatic deflection. The switch-yard can send ion beams of neighboring isotopes into three different beam-lines with a mass range of $\pm$15%. The selected ions* are subsequently sent to the experimental area and after 100 ms the switch-yard is turned off†. This is done to reduce the amount

*In this case one of the Argon Isotopes 31, 32 or 33.

†This time interval is called the beam-gate.

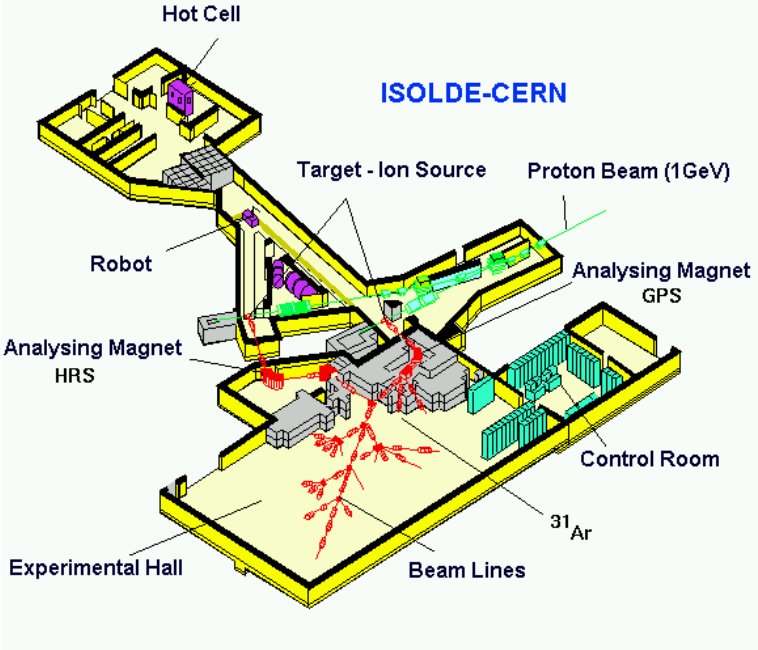

Figure 3.1: A 3D-view of the ISOLDE facility. The whole area, except the experimental hall, is buried under up to 8 m earth.

of non-selected isotopes that reach the collection foil. The ions are put to rest in a thin carbon collection foil (40 μg/cm^2) that is surrounded by different kinds of detectors. The total number of collected ^{31}Ar atoms was about 1.0×10^6 atoms which originate from a yield of about 3 atoms/s. Figure 3.1 shows the ISOLDE facility.

3.2 The detector-system

The detector-system consisted of a double-sided silicon strip detector, 15 silicon PIN diode detectors (FUTIS), a silicon surface barrier detector (ESI), and a High Purity Germanium γ-detector (HPGe). Figure 3.2 shows the used detectors except for the HPGe gamma detector.

3.2.1 The FUTIS detectors

The Finish FUTIS detectors consist of 15 silicon PIN diode detectors specially designed in a semi-sphere space-configuration. Each of the 15 detectors are telescope detectors consisting of a thin gas-detector just in front of a cylindrical Si detector with an effective diameter of 22.4 mm and a nominal thickness of 300 μm [41].

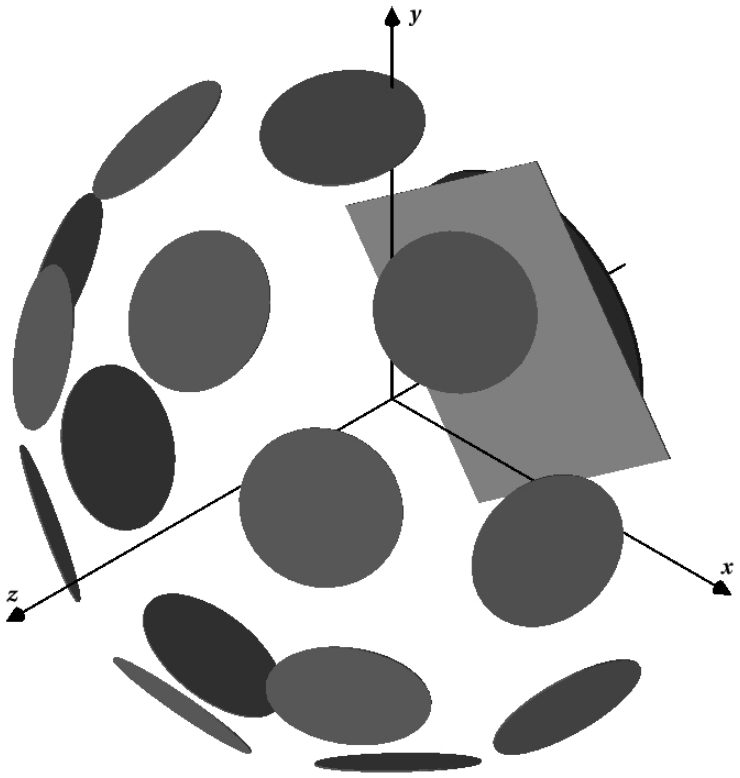

Figure 3.2: A 3D-view of the detector-system. The ion beam comes in from the left in the negative z-direction. 15 FUTIS detectors are situated to the left, and the collection foil (not shown) is placed at the origin. The strip detector is just behind the foil, and behind the strip detector you hardly see the thick Si detector. The HPGe gamma detector is not shown in the figure.

Just before the experiment started it was realized that the mylar windows in the FUTIS detectors were leaking, which made it impossible to use the gas detectors. Unfortunately, this deprives us of the great advantage for particle selection that a telescope detector offers*. In addition, the FUTIS detector 4 and 13 are excluded from this analysis because of problems with the preamplification.

The nominal positions of the 15 Si detectors are shown in table 3.1, the origin is chosen to be the same as in figure 3.2

3.2.2 The strip detector

The strip detector is a double sided 16×16 strips Si detector. Each strip has a nominal thickness of 276 μm, a width of 3 mm, and a length of 50 mm. According to the log book the strip detector is placed 33 mm behind the collection foil and

*This kind of detector telescope is also called a ΔE-E detector.

	Coordinates		
	x	y	z
1	−51.7024	7.0467	18.4486
2	−29.7294	17.1643	44.9367
3	−31.9538	−18.4486	41.2522
4	−48.1033	−27.7724	10.6081
5	−19.8280	−48.2661	18.4486
6	0	−34.3286	44.9367
7	19.7486	−48.2990	18.4486
8	31.9538	−18.4486	41.2522
9	48.1033	−27.7724	10.6081
10	51.7136	6.9615	18.4485
11	29.7294	17.1643	44.9367
12	31.9538	41.2522	18.4486
13	0	55.5463	10.6078
14	0	36.8971	41.2522
15	−31.8856	41.3046	18.4486

Table 3.1: Coordinates of the Finish detectors (mm).

rotated approximately 35° around the z-axis, according to the same coordinate system as used in figure 3.2 and table 3.1.

Silicon strip detectors are manufactured by implanting strips of doped silicon into a silicon wafer. The implants can be either positively or negatively doped. Positively doped implants are also called p-type implants. They have a majority of positive carriers (holes). Negatively doped implants, also called n-type implants, have a majority of negative carriers (electrons). A double sided silicon strip detector has implants on both sides. The n-side has n-type implants while the other, the p-side, has p-type implants. At the junction area, the negative carriers (electrons) can diffuse into the p-type silicon and neutralize the positive carriers (holes), leaving behind ionized impurity atoms on either side of the junction. This creates a region around the junction which is free of charge carriers and wherein there is a strong electric field. This region is called the depletion region.

A positive voltage is placed on the n-type implant and negative carriers are attracted to it, conversely a negative voltage is placed on the p-type implant to attract positive carriers. When a particle passes through the detector it liberates electron-hole pairs. The holes are attracted to the p-side by the negative voltage, and the electrons are attracted to the n-side by the positive voltage [42]. These signals are then amplified and recorded. The n-side we call the back-strips because

they are on the back-side of the detector, i.e. the side away form the decay site. Conversely, the p-side we named the front-strips because it is on the front-side of the detector, the side pointing into the decay site.

3.2.3 The surface barrier detector (ESI)

The Si surface barrier detector has a thickness of 700 μm, and a diameter of 50.7 mm. The Si detector is placed 3 mm behind the strip detector, in this way the most energetic protons have enough energy to go through the strip detector and subsequently enter the ESI detector. We can then correct the proton energy spectrum, obtained by the strip detector, to include the high-energy protons that passed through the strip detector. For these events we even have a ΔE-E selection possibility, in such a way that β particles are excluded.

3.2.4 The trigger logic

The trigger is the electronic unit which defines the conditions for the events that are recorded. The trigger in the experiment was build up with OR-gates in the following way.

The strip detector: We use an OR-gate in between the output signal of the front and the back strip of each strip, and an OR-gate in between the signal of each strip.

The FUTIS detector: OR-gates are used in between all the FUTIS detectors.

In this way, an event is defined to be a hit in at least one of the sides in one or more of the strip detectors, or a hit in at least one of the FUTIS detectors. The Si surface barrier detector and the HPGe gamma detector are not included in the trigger. The signal of each of these components are simply read out when the trigger is released. After the trigger is released there is a short time interval in which all signals have to arrive in order to be part of the event. This time interval is 8 μs long.

Furthermore, there is a low energy cutoff on each of the detectors, these low energy cutoffs are not chosen but they originate in the electronic. For the strip detector the low energy cutoff is about 350-550 keV, and for the FUTIS detectors they are roughly 200-300 keV.

The amplification of the detectors changed twice in the experiment, which made it necessary to use three different energy calibrations for the three different parts of the experiment.

3.3 Applied Software

3.3.1 Physics Analysis Workstation (PAW)

At the beginning of 1986 the Physics Analysis Workstation project (PAW) was launched at CERN [43]. The first public release of the program was made at the beginning of 1988, and new updated versions were made frequently until January 1999, where the project stopped. PAW runs on mainframes, workstations and PC's. At present, PAW runs on the majority of the computer systems used in the High Energy Physics community (HEP). PAW is conceived as an instrument to assist physicist in the analysis and presentation of their data. It provides interactive graphical presentation and statistical or mathematical analysis, working on objects like histograms, ntuples (event files), vectors etc.
PAW combines different tools and packages, i.e. KUIP, HBOOK, HPLOT, HIGZ, ZEBRA, MINUIT, COMIS and SIGMA.

KUIP: (Kit for a User Interface Package) The package handling the dialogue between the user and the program.

HBOOK: (Histogram BOOKing) The package providing the implements for data handling and the data storage structure, i.e. histograms and ntuples.

HPLOT: (Histogram PLOTting) The old data plotting package.

HIGZ: (a High level Interface to Graphics and Zebra) The package in between PAW and HPLOT and the basic graphics packages on a given system.

ZEBRA: The data structure management system, Input/Output manager.

MINUIT: The function minimization and error analysis package. The principal applications are computing the best-fit and deducing the uncertainties.

COMIS: The FORTRAN interpreter, it allows to execute FORTRAN routines interactively.

SIGMA: (System for Interactive Graphical Mathematical Applications) The mathematical and theoretical tool for array manipulation.

PAW is a fully developed program with a very long list of application possibilities. It has many good facilities and it can be used interactively and non-interactively. PAW includes a variety of callable Fortran subroutines which have been developed over the years. Besides that, it is possible to call uncompiled and compiled FORTRAN code from PAW, which makes it very flexible. PAW uses ntuples, a data structure designed for event files, see next section 3.3.2. Moreover, it has a high quality of graphical presentation. But beside these positive qualities, there are also some negative things to say about PAW. First of all, it is not very easy to use sometimes you have to try to solve your problem just by trying again and again. Moreover, PAW is a commando based program, a new version PAW++ using Graphics Window is made, but for a trained user it just slows down the working process. In addition, PAW is based on FORTRAN-77 a very old program language, which belongs to the past. Two new projects are launched at CERN called Libraries for HEP Computing (LHC++) and ROOT, which are both object-oriented software bases on C++. While ROOT is a fully developed program, LHC++ is still only a prototype. The team developing LHC++ is substantially larger than the ROOT team and LHC++ includes commercial packages. Both programs are thought to take over after PAW.

3.3.2 Ntuples

Ntuples are the basic type of data structure used in PAW. Before we started analyzing the experimental data, it was transformed to the ntuple structure. The best way to imagine an ntuple is to think on a matrix or a table. Imagine that y different physical parameters are measured in x different events, then we have a $x \times y$ matrix where each event is a row and the observed variables are columns. If we store the data this way, we have no information loss, and any possibly combination of observations can still be studied.
In principle, all computer data is stored in one long row. We use Column-wise-Ntuples (CWN), which means the columns are put after each other to build a long sequence. Below in table 3.2, you can see the ntuple-structure we have used in this experiment, the only difference is that the table shows the variables row-wise and not column-wise.

In each event, the number of hits in the FUTIS detectors is labelled NFIN, and the number of hits in the strip detector on the front and back side are respectively NF and NB. NDFIN, EFIN and TFIN are vectors with NFIN elements, i.e. one element for each hit in the FUTIS detector-system. NSF, EF and TF are vectors

Ntuple		
No.	Range	Variable
1	[0,15]	NFIN
2	[0,15]	NDFIN(1,2, ... ,NFIN)
3	[0,4096]	EFIN(1,2, ... ,NFIN)
4	[0,4096]	TFIN(1,2, ... ,NFIN)
5	[0,16]	NF
6	[0,16]	NB
7	[0,16]	NSF(1,2, ... ,NF)
8	[0,16]	NSB(1,2, ... ,NB)
9	[0,4096]	EF(1,2, ... ,NF)
10	[0,4096]	EB(1,2, ... ,NB)
11	[0,4096]	TF(1,2, ... ,NF)
12	[0,4096]	ESI
13	[0,4096]	EGAM
14	[0,4096]	TSI
15	[0,4096]	CLOCKS

Table 3.2: The used ntuple structure.

with NF components, one for each hit on the front side of the strip detector. NSB and EB are vectors with NB elements, i.e. an element for each hit on the back side of the strip detector. The vectors NDFIN, NSF and NSB are vectors containing the specific detector number in which the hits did happen. For instance NDFIN is a vector with NFIN elements, each with a number on the specific FUTIS detector in which the specified hit did happen. In the same way EFIN, EF and EB are vectors containing the energy of the specific hit of respectively the FUTIS detector system, the front side and the back side of the strip detector.*

Moreover, TFIN and TF are likewise vectors containing the time from the release of the trigger to the specific hits in respectively the FUTIS detector and the front side of the strip detector. ESI is the energy measured in the surface barrier detector. EGAM is the energy of the HPGe gamma detector. TSI is the time signal of the ESI detector and CLOCKS is the time from the production of the isotope to the specific event.

*All energies mentioned in this table are channel numbers, i.e. yet not calibrated.

Chapter 4

Checks and calibrations

4.1 Calibration of the ESI detector

The Si surface barrier detector (ESI) is calibrated by using a mixed ^{239}Pu-^{241}Am-^{244}Cm alpha-source. The spectrum of ^{239}Pu has three principal energies: 5105.5(8)

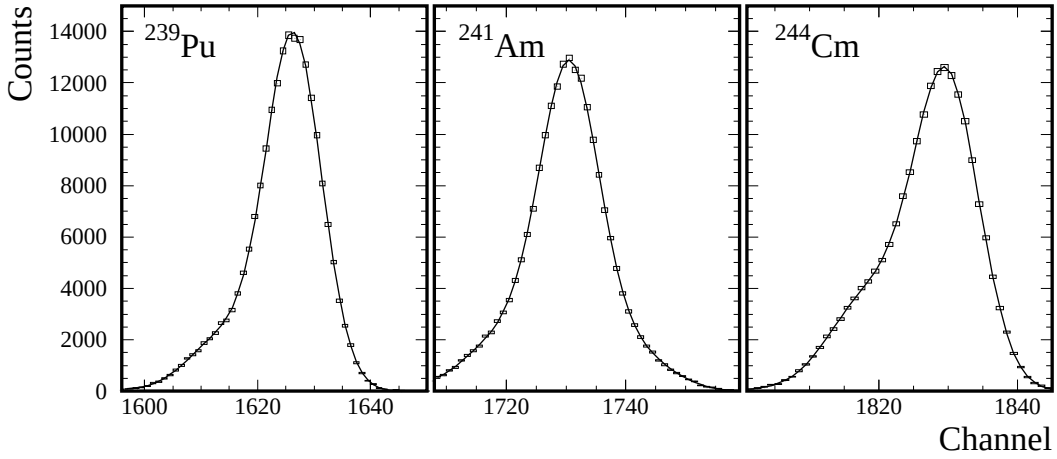

Figure 4.1: Intensity spectrum of the triple alpha source using the Si surface barrier detector. The smooth curves display fits using a sum of Gaussian plus a linear background. In the fit of ^{239}Pu a sum of two Gaussian has been used, in the case of ^{241}Am three Gaussian, and in ^{244}Cm a sum of two Gaussian.

keV, 5144.3(8) keV and 5156.59(14) keV. The last two peaks are very close in energy and thus, due to the low resolution of the detector, inseparable. In the case of ^{241}Am the lowest energy is 5388(1) keV, see table 4.1. This energy is not used in the fit, and it is outside the part of the spectrum seen in figure 4.1. The next four energies: 5442.90(13) keV, 5485.60(12) keV, 5512(2) keV and 5544(1) keV are used in a triple Gaussian fit, the branching ratios of the last two peaks are so small

Triple alpha source		
Source	Energy	Ratio
^{239}Pu	5105.5(8) keV	11.5(8) %
	5144.3(8) keV	15.1(8) %
	5156.59(14) keV	73.3(8) %
^{241}Am	5388(1) keV	1.4(2) %
	5442.90(13) keV	12.8(2) %
	5485.60(12) keV	85.2(8) %
	5512(2) keV	0.20(5) %
	5544(1) keV	0.34(5) %
^{244}Cm	5762.70(3) keV	23.6(2) %
	5804.82(5) keV	76.4(2) %

Table 4.1: Energies and Branching ratios for the triple α-source, from the Table of Isotopes [30].

that they are represented as only one peak. The spectrum of ^{244}Cm has only two clear lines, one at 5762.70(3) keV and the second at 5804.82(5) keV. Only the five clearest lines have been used in the energy calibration. The others are included in the Gaussian fit in order to get a more precise channel determination of the five clear peaks: 5156.59(14) keV, 5442.90(13) keV, 5485.60(12) keV, 5762.70(3) keV and 5804.82(5) keV. Notice that this is an α-calibration of a silicon detector which is only useful for α-energy determination. When we observe protons we are forced to include some corrections [44, 45]. The mean energy required to create an electron-hole pair in silicon is different for protons and for alpha particles. This effect is called the pulse height defect (PHD). If E is the energy of a particle before it stops in the detector, we can write the effective energy deposited in the detector as: $E^{'} = E - \Delta E_n$. The energy $E^{'}$ is associated with inelastic processes and contributes to the creation of electron-hole pairs, i.e. $E^{'}$ contributes to the measured signal. The energy loss ΔE_n is energy associated with elastic collision which leads to radiation damage and excitation of the crystal lattice. In the used energy interval, the mean difference in ΔE_n for an alpha and a proton particle is roughly $\Delta E_{n,\alpha} - \Delta E_{n,p} \cong 11(2)$ keV. For fission fragments the pulse height will fall with increasing Z, but for low Z the behavior is opposite. The mean energy required to create an electron-hole pair in silicon is called ϵ, the anomalous fact is that $\epsilon_\alpha/\epsilon_p = 0.986(3)$ [44, 45]. The calibration points are all in a small interval, wherefore we use a linear calibration. The alpha-calibration is given by:

$E_\alpha = a_\alpha \cdot Ch + b_\alpha$. The proton-calibration turns out to be:

$$\begin{aligned} E_p &= \frac{\epsilon_p}{\epsilon_\alpha}\Big(a_\alpha \cdot Ch + b_\alpha - \Delta E_{n,\alpha}\Big) + \Delta E_{n,p} \\ &\cong \frac{\epsilon_p}{\epsilon_\alpha} a_\alpha \cdot Ch + \frac{\epsilon_p}{\epsilon_\alpha}\Big(b_\alpha - (\Delta E_{n,\alpha} - \Delta E_{n,p})\Big) \\ &= a_p \cdot Ch + b_p \end{aligned} \tag{4.1}$$

The result of the calibration is:

$$a_p = 3.229(10) \quad \text{keV/channel} \tag{4.2}$$

$$b_p = -37(11) \quad \text{keV} \tag{4.3}$$

From the measured standard deviation(σ) of the peaks in figure 4.1 we can estimate the resolution of the ESI detector. Since α radioactive matter have very long half-lives, the natural linewidth of α-lines are extremely narrow. This is the reason why the resolution is equal to the observed widths. After the proton correction we get a resolution equal to $\sigma = 16.0(18)$ keV or 38(4) keV (FWHM)*.

4.2 Calibration of the strip and FUTIS detectors

4.2.1 Energy calibration

The histograms used in the energy calibration has the following off-line cuts

Front strip: { nf>0, nb=nf and 0<clocks<1000

Back strip: { nb>0, nf=nb and 0<clocks<1000

FUTIS: { nfin>0 and 0<clocks<1000

These cuts are used to produce a histogram for each of the 16 front-strips, 16 back-strips and the 15 FUTIS detectors in all 47 times!

The energy calibration of the β-delayed proton spectra are based on two internal points from the well known ^{33}Ar spectrum(^{33}Cl* $\rightarrow^{32}$S+p), as in [32, 34]. These kinetic energies are E_p=1643.4(14) keV and E_p=3167.6(12) keV. They are calculated by using the proton separation energy of ^{33}Cl: S_p=2276.8(7) keV, measured

*For a Gaussian the full width at half maximum (FWHM) is equal to $\sigma \cdot 2\sqrt{2ln(2)}$.

in the reaction: ^{32}S+p$\rightarrow^{33}$Cl+γ [46], and the known excitation energy of two ^{33}Cl levels: the $3/2^+$ level at 3971.9(12) keV, and the isobaric analogue state (IAS) of ^{33}Ar at 5544(1) keV [46]. The Q-value for the reaction: ^{33}Cl* $\rightarrow^{32}$S+p is equal to the difference of the excitation energy (E_x) and the proton separation energy (S_p): $Q = E_x - S_p$. If the ^{33}Cl nucleus is at rest, it follows from conservation of linear momentum that the non-relativistic kinetic proton energy is:

$$E_p = \frac{Q}{1 + M_p/M_R} \tag{4.4}$$

For comparison the relativistic kinetic proton energy is (in natural units):

$$E_p = \sqrt{\frac{Q\Big(Q + 2(M_p + M_R)\Big)\Big(Q\Big(Q + 2(M_p + M_R)\Big) + 4M_pM_R\Big)}{4\Big((M_p + M_R)^2 + Q\Big(Q + 2(M_p + M_R)\Big)\Big)} + M_p^2} - M_p \tag{4.5}$$

With Taylor series expansion, expanded to the second order in Q:

$$E_p = \frac{1}{1 + M_p/M_R}Q - \frac{1}{2}\frac{M_R - M_p}{(M_p + M_R)^2}Q^2 + \cdots \tag{4.6}$$

From this, it is seen that for $M_R > M_p$, the relativistic correction is negligible as long as $M_R \gg Q$. This condition is fulfilled in the above case, where the relativistic correction is on the last digit and within the uncertainty.
In appendix A, the energy calibration is shown in the tables A.1, A.2 and A.3.

4.2.2 Test of calibration

After the 47 histograms have been calibrated (see subsection 4.2.1), they are added together in three different groups: the front strips, the back strips and the FUTIS detectors. This is done separately for every part, in this way there are $3 \times 3 = 9$ histograms. Thereafter, the 13 most conspicuous peaks in the ^{33}Ar spectrum are located in each of the 9 histograms and they are compared with the same energies found in Schardt and Riisager [34]. The two calibration points are included in the 13 peaks. In figure 4.2, you can see the comparison of the FUTIS detectors in part 3 with the values taken from [34]. In appendix B, the figures B.1, B.2 and B.3 show the comparison of the remaining parts and detectors with the same values taken from Schardt and Riisager.

The first point at 1.32 MeV is a slightly lower than in [34], but the value 1317(3) keV found in Borge *et al.* [32] fits very well. The second point is a calibration point

so it better have to fit. The third point at about 1.70 MeV is not so precisely observed, because it has a low intensity and it is partly overlapped by the calibration peak at 1.64 MeV. The fifth point is measured to have a too high energy, this is because the peak 2.10 MeV includes a peak with a slightly higher energy of 2.12 MeV which is hardly seen because of the resolution. Points number four, six and eight fit very well and the seventh point is the second calibration point. The last

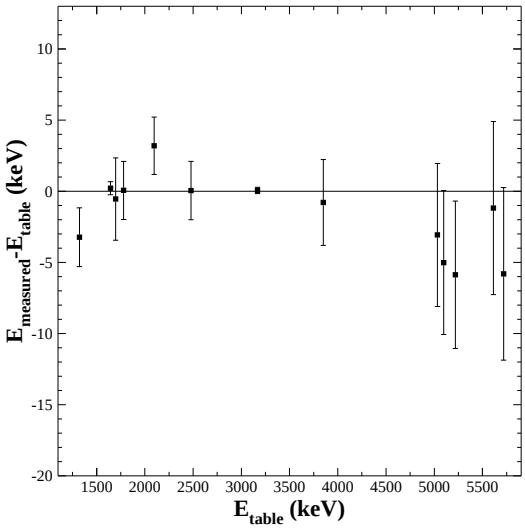

Figure 4.2: Check of the energy calibration, FUTIS part 3. The result in Schardt and Riisager [34] is used as table values.

5 points at high energies have all a slightly lower energy than in [34].

There seems to be small non-linear effect in the (Channel,Energy)-function. This effect is systematically seen in all the test figures, which indicates that the energy determination is slightly inaccurate. If we consider all the data in this subsection, the general conclusion would be that the energy calibration is reliable to the order of 10 keV.

4.2.3 The energy resolution of the strip detector.

A double sided strip detector has an interesting feature: it generates not only one but two electronic pulses for each hit in it, one on the n-side (front-strips) coming from the electron cluster and one on the p-side (back-strips) generated by the cluster of holes. This feature makes it possible to make an estimate of the resolution of the strip detector. We simply take the difference of the energy measured in the front and the back strip. For each case we get an approximate Gaussian distribution, an example of this is seen in the left part of figure 4.3.

The histograms used are produced with the following off-line cuts

$$\textbf{Strip detector:} \begin{cases} \text{nf=1, nb=1} & \text{and} \\ 0<\text{clocks}<600 \end{cases}$$

A histogram is made including all energies, and other histograms are made include only one of the energy intervals: 0-1 MeV, 1-2 MeV, 2-3 MeV, ..., 5-6 MeV. Each histogram includes all parts and it is repeated for each of the isotopes ^{31}Ar, ^{32}Ar and ^{33}Ar. The result of this analysis is shown in figure 4.3. From the table in

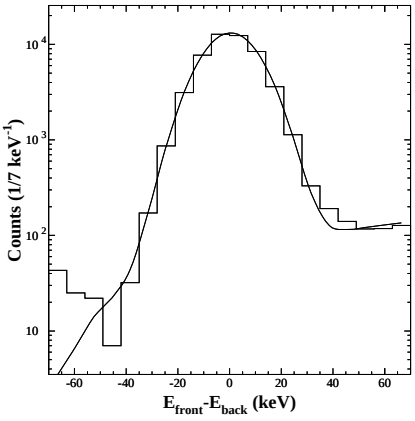

Energy in keV	Width parameter of the Difference		
	^{31}Ar	^{32}Ar	^{33}Ar
all	13.019(10)	10.841(13)	10.36(2)
0-1000	13.124(9)	12.93(5)	13.37(7)
1000-2000	11.61(5)	11.11(8)	10.82(7)
2000-3000	10.56(4)	10.56(2)	10.60(4)
3000-4000	10.22(7)	10.370(16)	10.247(12)
4000-5000	10.10(8)	10.39(11)	10.2(3)
5000-6000	10.62(8)	11.09(15)	10.50(9)

Figure 4.3: To the left you can see an example of the difference in energy of the front and the back strip, this example is of ^{33}Ar in the energy interval 2000-3000 keV. On the right side the width parameters for all the histograms are shown, the width parameters in the table are the standard deviation σ obtained by fitting the data to a Gaussian distribution with a linear background. The errors includes only errors derived from the fit, the errors coming from in the calibration is not included.

figure 4.3 it can bee seen that, for the intervals 0-1 MeV, 1-2 MeV, 2-3 MeV, 3-4 MeV and 4-5 MeV, the width parameter is decreasing as a function of energy. This makes it possible to conclude that the resolution of the strip detector is a slowly decreasing function of energy. For high proton energies (5-6 MeV) some protons pass through the detector and the obtained width parameter for these protons is therefore more uncertain.

At the same time, we observe that for the lowest group 0-1 MeV the width parameter is much higher than in the other groups. This is because there is a great amount of β-particles detected at low energies. High energy β-particles (> 1 MeV) pass through the strip detector with only a minor energy loss. Since we have a low signal cutoff on about 350-550 keV, many β-particles are not detected and the obtained β-particle spectrum is very distorted.

At this point the question is: What is the resolution of proton detection?

If we assume that the two signals are independent measurements of the same particle we can argue in this way: The front strip energy distribution is a Gaussian and the back strip energy distribution is a Gaussian with the same standard deviation σ. The difference of the distributions is then a Gaussian with standard deviation a factor $\sqrt{2}$ larger, and the standard deviation of each of the two distributions front and back is a factor $1/\sqrt{2}$ smaller than the standard deviation of the difference of the two distributions.

The signals deviation are not totally independent but we assume that the dependency is small. If this happens to be untrue, this resolution study can only be regarded as an estimate of the order of the resolution.

	Width of the difference		Single width	
	σ	FWHM	σ	FWHM
Positron	13.1(10) keV	31(2) keV	9.3(7) keV	21.8(17) keV
Proton	10.4(8) keV	24.4(19) keV	7.3(6) keV	17.2(14) keV

Table 4.2: Widths and resolutions of the strip detector.

By taking the values of the interval 0-1 MeV it is possible to obtain an estimate on the width parameter for positron detection. By taking the values of the intervals 2-3 MeV, 3-4 MeV, one can obtain an estimate on the strip detector's resolution for detecting protons. In table 4.2, the result is illustrated with the calibration errors included.

Beside these results, we have the resolution in which the spectra are recorded. This resolution depends on the energy calibration and it is equal to the bin size the spectra was recorded with. The maximum bin size is on 6.04 keV. However, the histograms are easier to use with integer bin sizes, this is why we have usually used bin sizes of 7 keV or 10 keV.

4.3 Examinations of the strip detector

As already explained in section 4.2.3, the strip detector generates not only one pulse per hit, but actually two pluses, one moving to each side of the detector. Figure 4.4 shows the distribution of E_{back} versus E_{front}, produced by traversing protons from the decay of the IAS of ^{33}Ar.

Due to the fact that some of the destroyed events can be either reconstructed to real events or excluded from the analysis, we are going to have a closer look at the

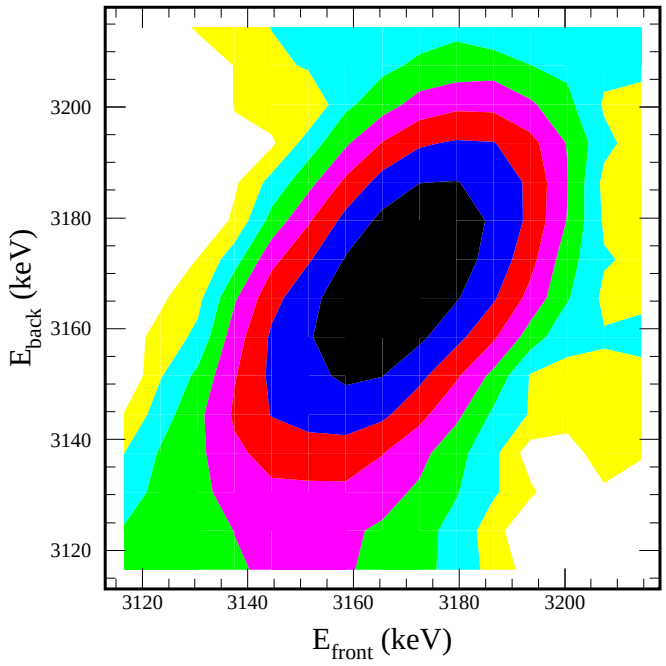

Figure 4.4: Protons from IAS of ^{33}Ar. The contour grey-levels are equidistant on a logarithmic scale, the levels are roughly 0-4, 4-14, 14-54, 54-210, 210-780, 780-2900, 2900-11000 and 11000-42000 counts per 7×7 keV^2.

losses of hits. The events can have many different kinds of losses. In the following sections, an analysis is given of the effects which entail the losses.

4.3.1 Charge loses and events in accidental coincidences

The events that we are looking at here are recorded as exactly one hit in only one of the front-strips, and as one hit in only one of the back-strips (nf=1 and nb=1). In figure 4.5, the energy correlation between the front and the back strips in the case of ^{31}Ar is shown. To the left, the plot without any cuts is illustrated and to the right you have the plot with all the cuts. Except for cut 1, all cuts are a result of unwanted effects in the strip detector. In the following we will go through the various types of effects resulting in the spread out of events. In an ideal double-sided strip detector with no accidental coincidences the events would be on the diagonal. This occurs most frequently. However, some hits fall far away from the diagonal. These hits are mostly events with very low energies ($E < 1200$ keV), i.e. mostly β-particles. At very low energies there is a very high number of hits, and for this reason also many accidental coincidences. These accidental coincidences are spread out over a large area, as seen in the low energy part of figure 4.5.

Figure 4.5: Protons from ^{33}Ar

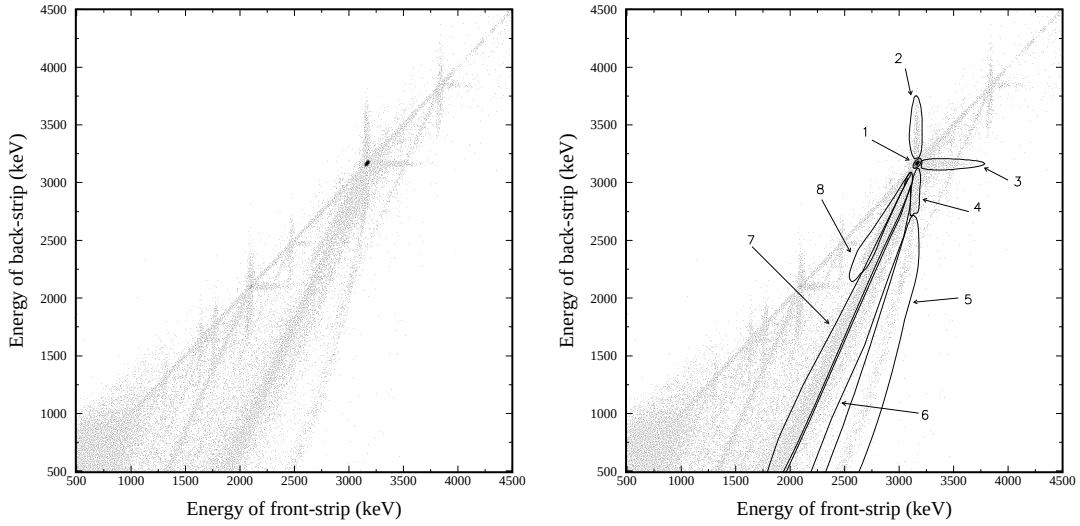

(a) without the cuts

(b) with the cuts

On the diagonal, two points are easily seen, one at $E = 2096$ keV and one at $E = 3168$ keV, the latter originate from protons from the IAS of ^{33}Ar. See figure 4.4 for a zoom of the spot from the IAS. To every proton peak on the diagonal there are some tails, one tail upwards (cut 2), one to the right (cut 3), one tail downwards (cut 4) and some tails obliquely downwards (cut 5-8). In the right part of figure 4.5 all these tails are shown. They originate from the decay of the IAS of ^{33}Ar and are generated by various unwanted effects in the detector. All the different cuts are shown in appendix B in the figures B.4 and B.5.

Cut number 1 illustrates the spot and in figure 4.6 you see the strip distribution of this spot. From figure 4.6, you can see that most hits occur at the center of the strip-detector (strip 8 and 9). This is because the solid angle of a fixed area becomes larger the closer it gets to the decay site, and because the central strips are closest to the decay site.

Figure 4.7 illustrates the effect of coincident summing with β-particles. Due to accidental coincidences it sometimes happens that a β-particle arrives at the same strip at the same time as a proton, and for this reason the observed energy is the sum of the energy of the β-particle and the proton. If a summation occurs in both the front and the back strip, the event is on the diagonal of figure 4.5 and cannot be distinguished from a real proton with the same energy.

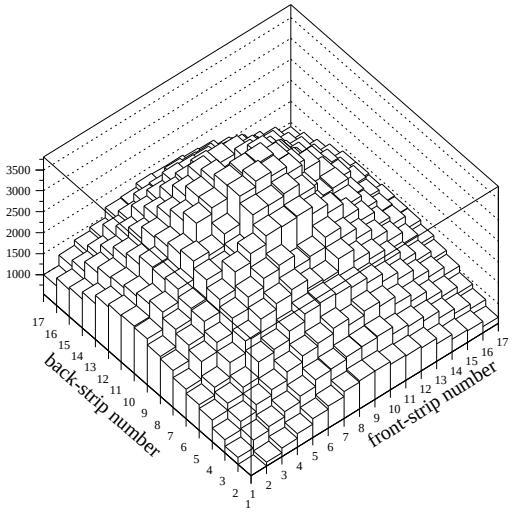

Figure 4.6: The strip-distribution of cut 1.

Figure 4.7: Examination of cut 2 and cut 3

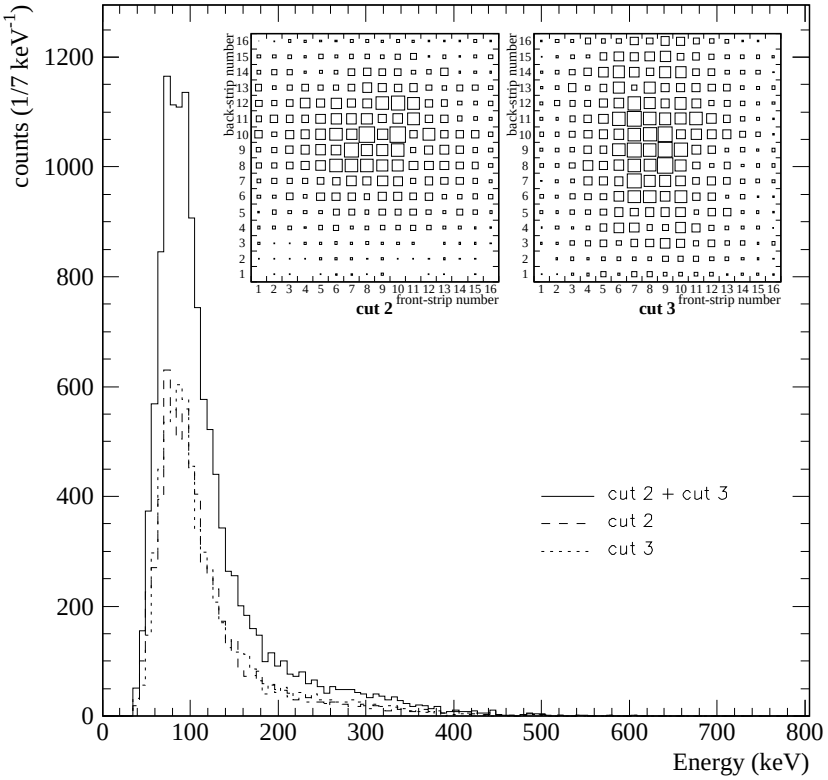

Coincident summing with β-particles

Most frequently the summation only happens in one of the two sides of the detector. In these cases, the effect looks like the tails in cut 2 and cut 3 of figure 4.5. The strip distribution of cut 2 is illustrated in the upper left part of figure 4.7. In that figure, the hits are more focused towards the center on the back side than on the front side. This indicates that the effect in cut 2 comes from the sum-effect. The probability of an energy summation is equal to the product of the probability distribution of protons and β-particles. The product of the distributions will have sharper edges and is more peaked at the center, which is exactly what is seen in the figure. In the upper right part of figure 4.7, the same plot is shown for cut 3 where the same effect can be seen. The only difference is that in cut 3 the sum-effect happens in a front strip. In the lower part of figure 4.7, a plot of counts versus $E_{back} - E_{IAS}$ of cut 2, and a plot of counts versus $E_{front} - E_{IAS}$ of cut 3 are drawn. The two curves look very alike, which leads to the conclusion that the two cuts have the same origin.

The sum of the two curves is also illustrated, this curve shows the deposited energy of β-particles in coincident summing with a proton. From this curve we can see that most β-particles deposit an energy below the low energy cutoff which is on about 350-550 keV. This conclusion is in good agreement with the fact that the strip-detector has a low thickness of 300 μm, wherefore most high energy β-particles go through the strip-detector with only a minor energy loss.

The effect behind cut 4 will be explained in section 4.3.2. The events in cuts 5-8 are all related to energy loss, to be more precise there is a larger energy loss in the back-strips than in the front-strips. At first sight, it looks very remarkable that nearly all the events spread out in figure 4.5 are under the diagonal. This effect is due to the construction of the detector which is a double sided silicon strip detector where the two different sides cannot be mirror images of each other.

Strip detectors are normally made on the basis of an n-type substrate. P-type strips are placed on the front side, they are already isolated because of the n-type substrate. On the backside, highly doped strips of n-type are used to create n^+-n contacts and not diodes, therefore poor interstrip isolation is expected on the backside. A worsening factor is the amount of electrons accumulated in a layer connecting the n^+ strips together, which makes it essential that this connection is broken, so that signals are not distributed over many elements [47]. In order to disconnect the n^+ strips one uses a highly doped p^+ region in between the strips [48]. These p^+ isolation implants will as a side effect enlarge the signal loss on the back-strip side.

In figure 4.8, the strip distribution of events in cut 5-8 is shown. It is seen

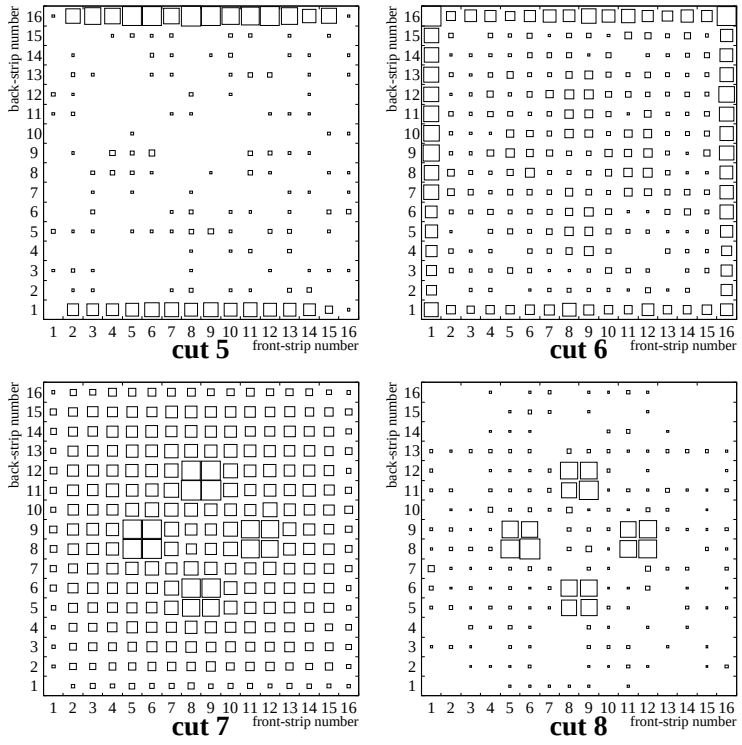

Figure 4.8: The strip-distribution of cut 5-8.

that cut 6 contains hits with energy losses which originate from protons with a trajectory passing one of the edges of the detector.

However, cut 5 is more remarkable because these hits are only in the back-strip number 1 and 16 and not in the correspondent front strips number 1 and 16. This effect must be related to the difference in geometry of an edge that is parallel to the back strips longitudinal direction with one that is not parallel to the back strips.

In cut 7, about 90% of the events have an energy loss caused by the normal interstrip space, the last 10% are an increased number of events in four regions. In these regions the metallic interstrip space is enlarged, this is why there is a larger energy loss there. Cut 8 contains only events from the regions with enlarged interstrip space.

To my knowledge it is still unknown why the different events in cuts 5-8 are found in different lines in figure 4.5, and why the lines have the depicted slope.

4.3.2 Charge sharing

Charge sharing is a phenomena related to events where one hit is spread out over two neighbouring strips. The analysis of charge sharing is done on the back strips

of the detector. The same effect happens at the front side, just with a much lower probability*. In figure 4.9, events with one hit in one front strip and two hits in two different back strips are drawn.

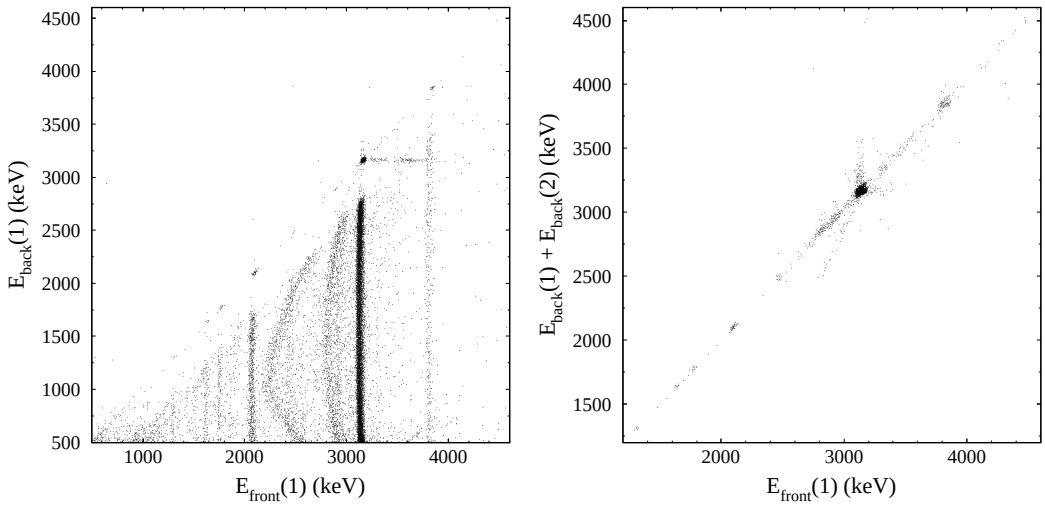

Figure 4.9: Charge sharing

To the left, you have an $E_{back}(1)$ versus $E_{front}(1)$ plot. It is seen that the events are spread down in lines under the diagonal. To the right you have an $E_{back}(1) + E_{back}(2)$ versus $E_{front}(1)$ plot, which looks very similar to the plots shown in figure 4.5.

The plot to the right in figure 4.9 has been cleaned up a bit by two additional conditions: The first condition is a low energy cutoff ($E > 1200$ keV) for each of the three energies $E_{front}(1)$, $E_{back}(1)$ and $E_{back}(2)$, which is used to exclude β-particles. The other condition is that if $E_{back}(1)$ or $E_{back}(2)$ is equal to $E_{front}(1)$ within a maximum difference of 21 keV†, the hit is kept in the plot.

In the left part of figure 4.9, you can see that there is a bare gap between the diagonal and the filled area of events. This is due to the low energy cutoff on about 350-550 keV which is included in the electronic setup. This effect is easily understood: Imagine a charge sharing event in which we have one hit on the front side but two hits on the back side. If the energy is spread out on two back strips in such a way that one strip gets an energy under the cutoff, the event will not bee seen in a plot like the one in figure 4.9, but it will be seen as an nb=1 and

*this is explained in section 4.3.1

†The 21 keV is equal to 2 times the resolution of the difference of the strips which correspond to a 95.4% confidence level, see section 4.2.3.

nf=1 event which is precisely what you can see in cut 4 of figure 4.5. Cut 4 is actually the missing events in the left side of figure 4.9. Another evidence for the same conclusion is seen in the right part of figure 4.9. Here, there is no tail vertical downwards i.e. there is no tail corresponding to cut 4 in figure 4.5, which means that the effect that causes cut 4 is not present. This conclusion is in full agreement with the explanation given above.

Finally figure 4.10 illustrates that out of all the nb=2 and nf=1 events, 90.2 ± 0.9 % are in neighbouring back strips, hence these events comes from the charge sharing effect.

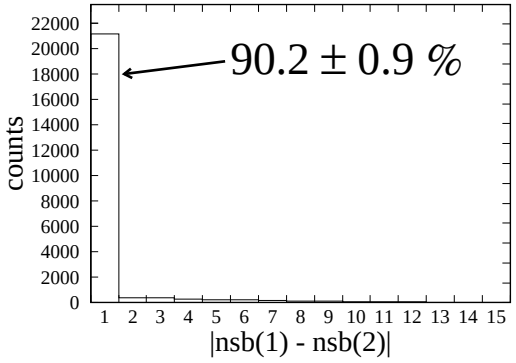

Figure 4.10: Charge sharing. The figure shows the absolute value of the difference in the strip numbers of the two back strip hits. In 90.2 ± 0.9 % of the events with nb=2 and nf=1, the two back strips are neighboring strips. This, once again, proves that these events have their origin in the charge sharing effect.

4.3.3 Summary of the different effects

Here, a summary is given of all the unwanted effects in the strip detector. For further reading about interstrip effects, especially charge sharing, see for instance Yorkston *et al.* [49].

Accidental coincidences: Accidental coincidences will always be present. Actually the number of Accidental coincidences is strongly reduced because of the low production rate on 3 atoms/s for ^{31}Ar.

coincident summing: Coincident summing is strongly reduced because of the small area of each strip. Since coincident summing often happens only in the back or the front strip, it is possible to remove many of these events by inserting a cut on the energy difference of the front and back strip energy.

Charge loses: Charge loses is an interstrip and a boundary effect. Events with charge loses are removed by using a cut on the energy difference of the front and the back side. The only disadvantage is the reduced efficiency of the strip detector.

Charge sharing: Charge sharing is an interstrip effect. By using limits on the energy difference of couples of front and back energies, one can strongly reduce this effect. Drawback: Reduced efficiency of the strip detector.

From the study of all the different effects in section 4.3, one finds that about 14% of the events are changed as a consequence of one of these effects. One can exclude a majority of these events by using a cut on the energy difference of the front and the back energy. This method was actually used, and as mentioned the only disadvantage was that the efficiency of the strip detector is reduced.

4.4 Correction of high energy protons

High energy protons (about $E > 5827$ keV) travel through the strip detector and stop in the Si surface barrier detector (ESI). The ESI detector is placed behind the strip detector. This means that for high energy protons only a part of the energy is deposited in the strip detector, the rest is put in the ESI detector. This $\Delta E - E$ detector, also called a telescope, gives us a E_{strip} versus E_{ESI} spectrum as shown in figure 4.11.

In the low energy part of figure 4.11, you can see both repeated detection of β particles and accidental β-β coincidences. The repeated detection of β particles are β particles that first enter the strip detector and then subsequently enter the ESI detector. Next to the E_{strip} axis, the p-β coincidences are placed. In these events, the protons are detected in the strip-detector and the β particles are detected in the ESI detector. In between the solid curves, we observe the protons which are repeated detected. You can see that the events originating in repeated detection lie on oblique lines, these are of course constant $E_{total} = E_{strip} + E_{ESI}$ lines.

With numerical methods, it is possible to calculate the energy loss in the strip detector [50]. The difference of the top and the bottom curve comes from the solid angle and the thickness of the strip detector. Imagine that you are at the collection foil and that θ is half the angle the strip detector shade your outlook. If a proton passes through the periphery of the strip detector it will be in silicon a distance that is a factor $1/\cos(\theta)$ greater than the detector thickness. The angle θ is about

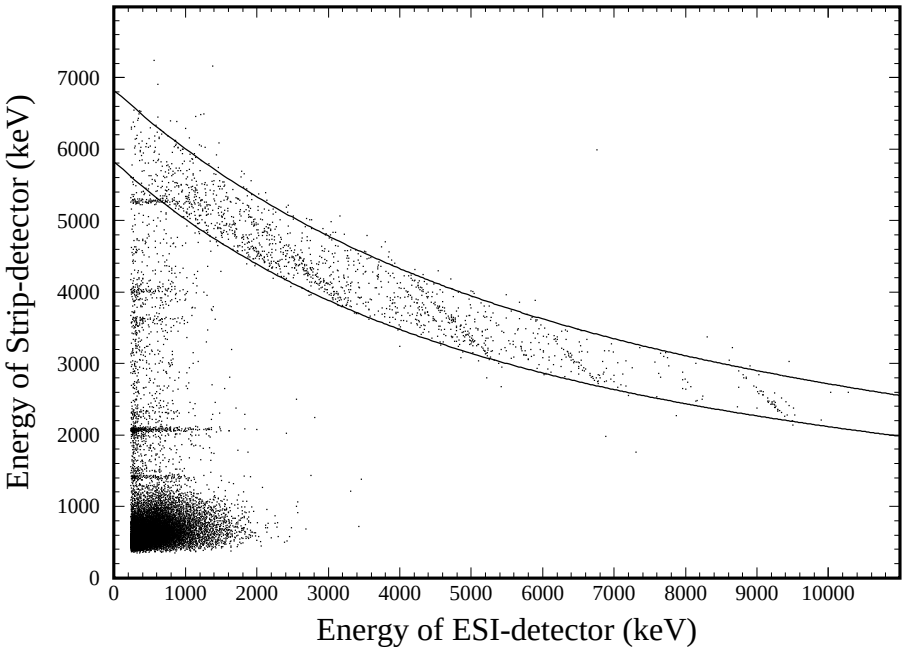

Figure 4.11: Coincidences of the strip and the ESI detector in the case of ^{31}Ar. In between the solid lines are the proton events of interest. The solid lines are numerical calculated curves extrapolated from data of proton ranges in silicon [50].

40^o which gives us a maximal effective thickness that is a factor 1.3 larger than the thickness. Protons that pass through the detector close to the edges have therefore an energy loss that is lot higher than protons with a trajectory perpendicular to the detector surface.

Beside a graphical cut, cutting out the region in between the two solid curves, we use a low energy cutoff: $E_{ESI} > 700$ keV to prevent against p-β coincidences. In addition we have placed some boundaries on the time of flight, i.e. on the time difference of TSI and TF. Unfortunately the broadening effect in effective thickness, also enlarge the difference in effective distance between the strip and the ESI detector. The allowed time of flight of the protons is therefore broaden so much, that these boundaries cannot be used to exclude all unwanted events.

We do not observe many high energy protons, for instance in all the data recorded for the precursor ^{31}Ar, there is roughly only 2000 events of repeated proton detection.

Chapter 5

Study of the kinematic shift in β-delayed proton emission

In a β-decay, the daughter nucleus gets a small recoil energy. Moreover, if it is unstable to particle emission it will breakup shortly thereafter. The particle-emitting states populated in the β-decay have very short lifetimes, and therefore nearly no collisions with neighboring atoms take place before the particle emission. The kinetic energy of a β-delayed particle will therefore be Doppler shifted as a consequence of the recoiling motion of the daughter nucleus. The size of the shift is in general of the order of 10 keV. The shift contains information about the decay chain, back to the β-decay. It is therefore possible to perform assignments of isospin, spin and energy of the intermediate states populated in the β-decay. In the following, this kinematic shift will be studied in further detail.

5.1 Theory

Since Pauli in 1930 made the then outlandish proposal of the existence of a very penetrating new neutral particle of vanishing small mass, the "neutrino" [51], it is known that in β-decay not only a β-particle is emitted but also a (mostly) unobserved neutrino. Since the discovery of the neutrino, many interesting phenomena have been observed in connection with β-decay, among others parity non-conservation. In 1956, Lee and Yang [52] started to examine parity (P) non-conservation of the weak interaction, and they established that so far no experiment had been undertaken to verify the standing hypothesis that the weak interaction should be invariant under space inversion (P). They therefore proposed experiments to clarify if parity is conserved in the weak interaction. One of their suggestions was

to measure the distribution of emitted β-particles with respect to polarized nuclei in β-decay. In 1957, Wu and coworkers [53] used polarized ^{60}Co nuclei to observe a large asymmetry of β-particles emitted with respect to the nuclear spin direction in an allowed Gamow-Teller decay [$\Delta J = 5-4 = 1$ (no)], i.e. the conclusion is that parity symmetry is violated in the weak interaction. This is an example of how the angular distribution of the emitted particles in β-decay have played an important role in nuclear physics.

5.1.1 The β-ν angular correlation

Valuable information about the weak interaction can be obtained by studying the angular correlation between the electron and the neutrino. The β-ν angular correlation is given by [51]

$$W(\theta_{\beta\nu}) = 1 + a\frac{p_\beta}{E_\beta}cos\,\theta_{\beta\nu} \tag{5.1}$$

where $\theta_{\beta\nu}$ is the angle between the β-particle and the neutrino and p_β/E_β is the ratio between the momentum and the total energy of the β-particle*. The coefficient a describes the β-ν angular correlation and is given by [51]

$$a = \frac{g_V^2 B_F - \frac{1}{3}g_A^2 B_{GT}}{g_V^2 B_F + g_A^2 B_{GT}} \tag{5.2}$$

where g_V and g_A are the vector (Fermi) and axial-vector (Gamow-Teller) weak coupling constants, and B_F and B_{GT} are the reduced β-decay matrix elements.

Figure 5.1 illustrates the difference between the β-ν angular correlation of allowed Fermi and Gamow-Teller decays in the extreme relativistic limit. In appendix E the selection rules for allowed β-decay are summarized. From the upper half of figure 5.1, we can conclude that in Fermi decays ($a = 1$) the momenta of the neutrino and the β-particle have an enhanced probability of being aligned in the same direction, whereas in Gamow-Teller decays ($a = -1/3$) the momenta have an enhanced probability of being in diametrically opposite directions.

The same conclusion can be drawn from a very simple argument using a one dimensional model as shown in the lower half of figure 5.1. The illustrated decay is a β^+-decay, the argumentation for β^--decay is similar. A relativistic positron is right-handed which is also called a positive helicity state†. A neutrino is left-handed which is likewise called a negative helicity state. One of the selection rules

*The ratio p_β/E_β is equal to v_β/c, the velocity of the β-particle in units of the speed of light. Notice the use of natural units in which the speed of light c is equal to 1.

†The helicity is the projection of the spin along the direction of motion:$\lambda = \boldsymbol{S}\cdot\boldsymbol{p}/|\boldsymbol{p}|$.

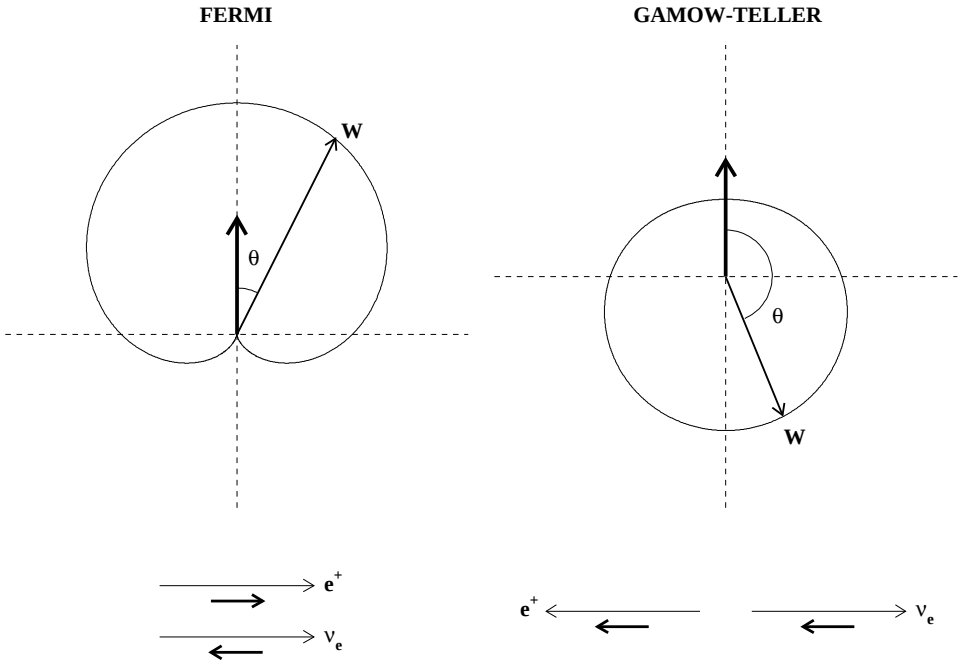

Figure 5.1: Comparison of the β-ν angular correlation of Fermi and Gamow-Teller decays. The plots are of the extreme relativistic case where even the mass of the β-particle is negligible. This approximation simplifies the $W(\theta)$-function to $1 + a\ cos(\theta)$. The upper half of the figure displays the β-ν angular distribution W as a function of the angle θ between the β-particle and the neutrino. The short arrow represents the direction of the momentum of one of the two emitted particles and the long thin arrow represents the direction of the momentum of the other particle emitted, but the length of the long thin arrow is put equal to the value of the $W(\theta)$-function. The lower half of the figure illustrates the most probable directions of momenta of the β-particle and the neutrino in a simple one dimensional model. The long thin arrows represent the direction of the momenta of the particles and the short arrows represent the helicities of the particles. For simplicity, only the β^+-decay is shown.

for allowed Fermi decay is that the total intrinsic spin of the β-particle and the neutrino is equal to zero ($S = 0$). This is why, the spin of the β-particle and the neutrino are pointing in opposite directions in allowed Fermi decays. Add to this that the β-particle and the neutrino are in opposite helicity states. We can thereby deduce that they cannot have opposite direction of motion, but they will most probably have aligned momenta. In Fermi decay, we can hereby conclude that the probability for $\theta_{\beta\nu} = 180^o$ is equal to zero in the extreme relativistic limit.

Notice that this result is independent of the parent nucleus spin direction because the intrinsic spin of the β-particle and the neutrino is a zero vector which has no direction. We can therefore also conclude that the distribution of β-particles

and neutrinos relative to the spin direction of the parent nucleus is isotropic even for polarized nuclei.

In allowed Gamov-Teller decay, the total intrinsic spin of the β-particle and the neutrino is equal to one ($S = 1$) with respect to the parent nucleus spin direction. Since we are looking at unpolarized nuclei, we have to take the average over all the possible nuclear spin directions. Here, only a simple argument is presented. The total intrinsic spin of the β-particle and the neutrino is $S = 1$, hence $S_z = -1, 0, 1$. We cannot exclude any of these spin-states. However, the spin of the β-particle and the neutrino is parallel in 2 out of 3 of these states. Since the emitted β-particle and the neutrino is having opposite helicity they will most probably have the opposite direction of motion. This is a very loose argument for the displayed β-ν angular correlation in figure 5.1, for more detailed calculations see "Beta decay" by Wu and Moszkowski [51].

We have now seen that in allowed Fermi decay the β-particle and the neutrino have a higher possibility for alignment of momenta contrary to allowed Gamov-Teller decay where the β-particle and the neutrino more frequently have reversed directions of motion. From this we can conclude that allowed Fermi decay result in a higher recoil energy of the β-daughter nucleus than an equivalent allowed Gamow-Teller decay, and hence also a higher kinematic shift of an eventually β-delayed particle. Allowed Fermi and Gamow-Teller decays can therefore be separated by looking on the kinematic shift of emitted β-delayed particles. However, There are many other factors that can enhance or reduce the kinematic shift which we will turn to in section 5.1.2.

5.1.2 The kinematic shift of β-delayed protons

The process of β-delayed proton emission is shown in figure 5.2. In the following, a simple model for the kinematic shift of the β-delayed proton will be presented. Let $\mathbf{v}$ be the velocity of the proton in the reference frame of the β-daughter nucleus, $\Delta\mathbf{v}$ the velocity of the daughter nucleus in the laboratory frame and m_p the mass of the proton. The proton and the β-daughter nucleus are both to a good approximation non-relativistic. The kinetic energy T_p of the proton can hereby be written as follows in the laboratory frame [54]

$$\begin{aligned} T_p &= \frac{1}{2} m_p (\mathbf{v} + \Delta\mathbf{v})^{\mathbf{2}} \\ &= \frac{1}{2} m_p v^2 + m_p \mathbf{v} \cdot \Delta\mathbf{v} + \frac{1}{2} m_p (\Delta v)^2 \end{aligned} \tag{5.3}$$

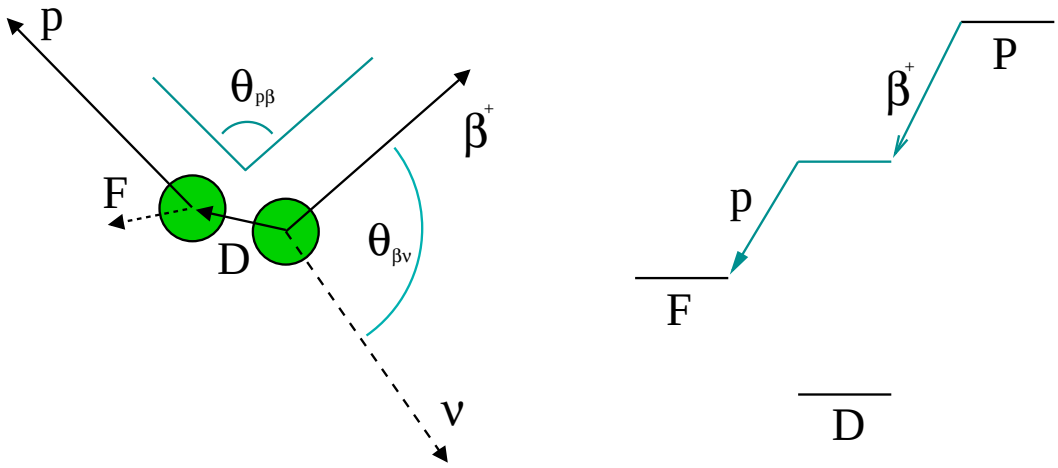

Figure 5.2: Schematic representation of β-delayed proton emission. The left half of the figure shows the kinematics involved in this decay process while the right half shows a simplified decay scheme. The precursor (P) populates an excited state in the β-daughter nucleus (D). The recoiling daughter subsequently emits a proton and transmutes into the final nucleus (F) of the decay process. The angle $\theta_{p\beta}$ is a directly measurable quantity whereas the angle of interest, $\theta_{\beta\nu}$, is not because the neutrino is unobserved.

The first term is equal to the kinetic energy of the proton in the rest frame of the β-daughter nucleus. The second term is the dominating contribution to the kinematic shift, and the last term is neglected because $\Delta v \ll v$.

Let the momentum of the β-particle be $\mathbf{p}_\beta$, the momentum of the neutrino $\mathbf{p}_\nu$, and the momentum of the β-daughter nucleus $M\Delta\mathbf{v}$, where M is the mass of the β-daughter nucleus. It follows from momentum conservation ($M\Delta\mathbf{v}+\mathbf{p}_\beta+\mathbf{p}_\nu=\mathbf{0}$) that the kinematic shift (t) is given by

$$\begin{aligned} t &= m_p\mathbf{v}\cdot\Delta\mathbf{v} \\ &= \frac{m_p}{M}\mathbf{v}\cdot(-\mathbf{p}_\beta-\mathbf{p}_\nu) \\ &= -k(p_\beta\cos\theta_{p\beta}+p_\nu\cos\theta_{p\nu}) \end{aligned} \tag{5.4}$$

where the proportionality constant k is

$$k=\frac{m_p v}{M}=\frac{\sqrt{2m_pT_{p,D}}}{M}=\sqrt{\frac{2Q_pm_p(M-m_p)}{M^3}} \tag{5.5}$$

In this formula, $T_{p,D}$ is the kinetic energy of the proton and Q_p is the energy release in the proton emission. Both energies are in the rest frame of the β-daughter nucleus.

The neutrino is unobserved in the experiments measuring the kinematic shift. We are therefore as a minimum forced to take the average over all the neutrino

angles. However, the angular distribution in β-delayed particle emission is more complicated than the β-ν angular distribution of β-decay, especially in Gamow-Teller decays. This is because the β-daughter nucleus is polarized in Gamow-Teller decays.

Imagine a case where we observe a positron of a Gamow-Teller β^+-decay in the extreme relativistic limit. The relativistic positron has positive helicity and the neutrino is left-handed (has negative helicity). Moreover, in Gamow-Teller decay the direction of the neutrino momentum is most probably opposite to the positron motion*. If we chose the positron direction of motion as the quantization axis, we can conclude that the intrinsic spin of the β-ν couple with largest probability is equal to one ($S_z = 1$), and the β-daughter nucleus is hereby polarized in the direction opposite to the motion of the positron. Hence, in a Gamow-Teller decay the β-daughter nucleus is polarized, even when the parent nucleus is unpolarized.

Let the emitted β-delayed proton carry orbital angular momentum L. If $L > 0$ we have a distribution of emitted protons that is not isotropic with respect to the spin direction of the β-daughter nucleus. Therefore, if the β-daughter nuclei are polarized, as they are in Gamow-Teller decays, the distribution of β-delayed protons are affected by the polarization of the β-daughter nuclei. We are therefore forced to introduce the β-ν-p triple angular correlation.

The β-ν-p angular correlation was first derived by Morita [55], and a more complete form was given by Holstein [56]. Holstein made some small misprints which were corrected in Clifford [54]. A simplified version of the triple angular correlation only including the dominating terms is given by†

$$W = 1 + \frac{1}{2}(3a - A)\frac{p_\beta}{E_\beta}\cos\theta_{\beta\nu} + \frac{3}{2}(A - a)\frac{p_\beta}{E_\beta}\cos\theta_{p\beta}\cos\theta_{p\nu} \tag{5.6}$$

where a and A are given by

$$a = \frac{g_V^2 B_F - \frac{1}{3}g_A^2 B_{GT}}{g_V^2 B_F + g_A^2 B_{GT}} \qquad A = \frac{g_V^2 B_F - (\frac{1}{3} + \frac{2}{30}\tau\Theta)g_A^2 B_{GT}}{g_V^2 B_F + g_A^2 B_{GT}} \tag{5.7}$$

In Clifford *et al.* [54], the coefficient A is called the triple-correlation coefficient and in Schardt and Riisager [34] it is called the asymmetry parameter. The two new parameters τ and Θ depend on the spin sequence in the β-decay and the proton emission, and they are defined in appendix C.

*See section 5.1.1

†The result is actually derived for β-delayed α-particles in the papers of Morita [55] and Holstein [56], but the formula for delayed protons is identical.

Notice that if $A = a$ the triple angular correlation W is equal to equation 5.1. The product $\tau\Theta$ is only different from zero if the proton carries orbital angular momentum ($L > 0$), i.e. the triple angular correlation W is only different from the β-ν angular correlation if the proton carries orbital angular momentum ($L > 0$) and the allowed β-decay is of the Gamow-Teller type. In allowed Fermi decay, the triple angular correlation is always equal to equation 5.1. Of course these results are in the lowest order approximation.

The kinematic shift averaged over all neutrino angles is given by

$$< t >_\nu = \frac{\int t\, W\ d\Omega_\nu}{\int W\ d\Omega_\nu} \tag{5.8}$$

Many terms of the integrals are zero and one easily finds that the only nonzero terms are the following

$$\begin{aligned} < t >_\nu = -k\Bigg(& p_\beta \cos\theta_{p\beta} + \frac{1}{2}(3a - A)\frac{p_\beta p_\nu}{E_\beta} < \cos\theta_{\beta\nu}\cos\theta_{p\nu} >_\nu \\ & + \frac{3}{2}(A - a)\frac{p_\beta p_\nu}{E_\beta}\cos\theta_{p\beta} < \cos^2\theta_{p\nu} >_\nu \Bigg) \end{aligned} \tag{5.9}$$

It is easily shown that $< \cos^2\theta_{p\nu} >_\nu = 1/3$, but the term $< \cos\theta_{\beta\nu}\cos\theta_{p\nu} >_\nu$ is a bit more complicated. Let the proton direction of motion define the z-axis, and the direction of the β-particle be in the yz-plan. Then $\theta_{p\nu}$ is the polar angle and ϕ is the azimuthal angle of the neutrino direction of motion. By using the law of cosines for a spherical triangle, we can write

$$\cos\theta_{\beta\nu} = \cos\theta_{p\beta}\cos\theta_{p\nu} + \sin\theta_{p\beta}\sin\theta_{p\nu}\cos\phi \tag{5.10}$$

Since $\theta_{p\nu}$ and ϕ are independent spherical coordinates defining the direction of the neutrino, we can conclude that there is no contribution to the integral from the last term in the above formula. We hereby get

$$< \cos\theta_{\beta\nu}\cos\theta_{p\nu} >_\nu = \cos\theta_{p\beta} < \cos^2\theta_{p\nu} >_\nu = \frac{1}{3}\cos\theta_{p\beta} \tag{5.11}$$

We therefore reach the following result

$$< t >_\nu = -k\cos\theta_{p\beta}(1 + \frac{1}{3}A\frac{p_\nu}{E_\beta})p_\beta \tag{5.12}$$

The above derivation is inspired by the formulation of Clifford *et al.* [54]. In the work of Clifford *et al.* [57, 54], the kinetic energy of the α-particle and the β-particle was measured in three different angles ($\theta_{\alpha\beta} = 45^o, 90^o, 180^o$).

By neglecting the recoil of the β-daughter nucleus one finds that

$$Q_\beta = E_x + T_\beta + T_\nu = E_x + T_\beta + p_\nu \tag{5.13}$$

Thus, by knowing the energy release in the β-decay (Q_β), the excitation energy (E_x), and the kinetic energy of the β-particle (T_β), one can calculate the kinetic energy of the neutrino. The energies T_β and T_ν can be rewritten as:

$$T_\beta = E_\beta - m_\beta = \sqrt{p_\beta^2 + m_\beta^2} - m_\beta \qquad\qquad T_\nu = E_\nu = p_\nu \tag{5.14}$$

Where m_β is the mass of the β-particle.

We can therefore conclude that it is possible to deduce the triple angular correlation (A), when T_p, T_β and $\theta_{p\beta}$ are measured, and Q_β and E_x are known. In other terms; information about isospin and spin can be deduced from the above formulas, if T_p, T_β and $\theta_{p\beta}$ are observed quantities. However, it is tricky to measure the energy of β-particles in a silicon detector because one has to know the response function of the detector very well. We have used many detectors, and we do not know the response functions that well.

I have therefore chosen a different approach to that of Clifford. Instead of measuring the kinetic energy of the β-particles, I will use a simple approximation whereby it is unnecessary to know the kinetic energy of the β-particles. This approximation gives a simple formula, that can easily be used to derive qualitative observations of the interesting triple-correlation coefficient A. Let us first rewrite the derived formula of $< t >_\nu$ in terms of the kinetic energy of the β-particle (T_β):

$$< t >_\nu = -k \cos\theta_{p\beta} \left(1 + \frac{A}{3}\left(\frac{T_{\beta,max} - T_\beta}{T_\beta + m_\beta}\right)\right) \sqrt{T_\beta(T_\beta + 2m_\beta)} \tag{5.15}$$

where $T_{\beta,max}$ is the maximal kinetic energy of the β-particle ($T_{\beta,max} = Q_\beta - E_x$). The formula of $< t >_\nu$ can be simplified by rewriting it in terms of the total energy of the β-particle (E_β):

$$< t >_\nu = -k \cos\theta_{p\beta} \left(1 + \frac{A}{3}\left(\frac{E_{\beta,max} - E_\beta}{E_\beta}\right)\right) \sqrt{E_\beta^2 - m_\beta^2} \tag{5.16}$$

where $E_{\beta,max}$ is the maximal energy of the β-particle ($E_{\beta,max} = T_{\beta,max} + m_\beta$). Figure 5.3 shows how the kinematic shift depends on the kinetic energy of the β-particle and the triple correlation coefficient (A). You can see that we can approximate the curves to straight lines. The low energy limit in figure 5.3 is defined as the minimum energy so that the asymptotes are reliable approximations of the curves.

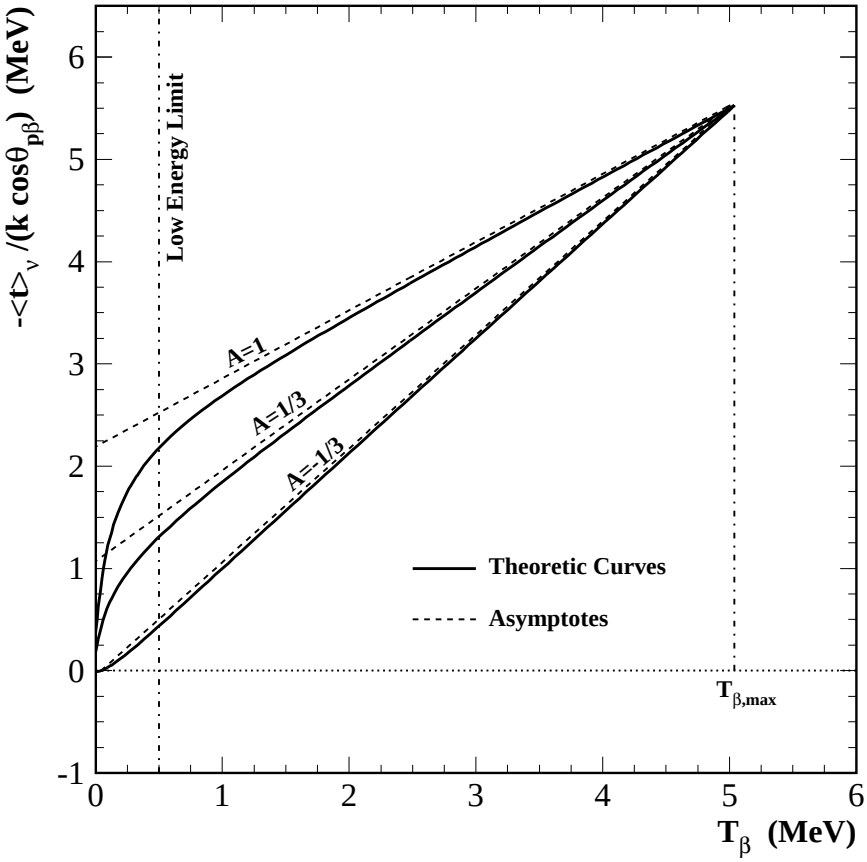

Figure 5.3: The figure illustrates the function: $- < t >_\nu \ /(k \cos\theta_{\beta\nu})$. In this example, a $T_{\beta,max}$ value of the IAS of ^{33}Ar is used. Three curves are shown, one for Fermi decays ($A = 1$) and two for Gamow-Teller decays. The two Gamow-Teller curves are for β-delayed protons with orbital angular momentum $L = 0$ ($A = -1/3$) or for β-delayed protons in the transition $1/2^+ \rightarrow 3/2^+$ ($A = 1/3$) with orbital angular momentum $L = 2$. All the curves approach the asymptotes very fast, and for kinetic energies larger than the low energy limit the asymptotes give a good approximation to the real value.

In the experiment, the low energy cutoffs are respectively at 350-550 keV for the strip detector and 200-300 keV for the FUTIS detectors. It should however be noticed that these low energy cutoffs are on the deposited energy of the β-particles. The total kinetic energy of the β-particles are mostly a lot larger than the deposit energy. I therefore expect that the kinetic energy of the detected β-particles are larger than the low energy limit of the straight line approximation. From the approximation to straight lines, we thus get:

$$\begin{aligned} < t >_\nu &\cong -k \cos\theta_{p\beta}(\frac{A}{3}E_{\beta,max} + (1 - \frac{A}{3})E_\beta) \\ &= -k \cos\theta_{p\beta}(\frac{A}{3}T_{\beta,max} + (1 - \frac{A}{3})T_\beta + m_\beta) \end{aligned} \tag{5.17}$$

Instead of measuring T_β, one can take the average of $< t >_\nu$ over the beta spectrum. Since we do not precisely know how efficient the β-particles actually are detected by the detector-system, and since each detector has a different response function, we cannot deduce the kinetic energy of the β-particles. Moreover, we cannot expect the spectrum of the detected β-particles to be undistorted by the response functions.

Therefore, I have decided to use a qualitative model which cannot be used to precise quantitative observations. In this model, we use some approximations which are given in the following. In the limit $T_{\beta,max} \gg m_\beta$, we can rewrite equation 5.17 to

$$< t >_\nu \cong -k\, T_{\beta,max} \cos\theta_{p\beta} \left(\frac{A}{3} + (1 - \frac{A}{3}) \frac{T_\beta}{T_{\beta,max}}\right) \tag{5.18}$$

Moreover, it is assumed that the detection efficiency of observing β-particles is nearly uniform and that the the effect of the Fermi-function is negligible ($F = 1$). Beside that, it follows from the assumption: $T_{\beta,max} \gg m_\beta$, that the average kinetic energy of the β-spectrum is approximately $< T_\beta >= 1/2\, T_{\beta,max}$. We thus finally reach an approximation of the kinetic energy shift averaged over all directions of the neutrino and β-particle energies:

$$\bar{t} \cong -k\, T_{\beta,max} \cos\theta_{p\beta} \left(\frac{3 + 2A}{12}\right) \qquad \text{for } T_{\beta,max} \gg m_\beta \tag{5.19}$$

This is the approximation we will use in the next section 5.2.

5.2 Analysis and results

One of the advantages of this experiment in respect to previous experiments studying the kinematic shift is that we have detectors spread out over a sphere surrounding the collection foil. This means that we can measure the kinematic shift of the β-delayed protons at any angle between the β-particle and the proton ($\theta_{p\beta}$). To my knowledge this has not been done before.

Only double hit events in which the one hit has an energy in an energy window around the proton peak and the other hit is in coincidence and has an energy E_β(low energy cutoff$< E_\beta <$ 1200 keV), are accepted as p-β coincidences. Other cuts, for instance on the energy difference of the front and back strips, are used to reduce effects caused by interstrip loses, see section 4.3.

The data is grouped in angles with bin-size 20^o, and an average over all the events with the specified angle is put in each bin. Only peaks with many events can be used because good statistic is needed in the averaging over the β energy

spectrum. The test analysis presented in this chapter is therefore based on the 6 largest peaks in the spectra of ^{32}Ar and ^{33}Ar.

The result of this analysis is shown in Figure 5.4. Each of the 6 plots in figure 5.4 are fitted to

$$T_p = T_{p,\perp} - \varepsilon \cos\theta_{p\beta} \tag{5.20}$$

The result of these fits are shown in table 5.1 The energy $T_{p,\perp}$ is the mean energy of protons emitted perpendicular to the β-particle: $T_{p,\perp} = T_p(\theta_{p\beta} = 90^o)$.

Fitting results				
No.	Precursor	Events	$T_{p,\perp}$	ε
1	^{32}Ar	3460	2125.7(3) keV	3.7(5) keV
2	^{32}Ar	6263	2422.9(3) keV	2.8(5) keV
3	^{32}Ar	20086	3352.05(8) keV	5.68(15) keV
4	^{33}Ar	3209	2100.5(3) keV	3.5(5) keV
5	^{33}Ar	40070	3168.46(6) keV	5.50(10) keV
6	^{33}Ar	1089	3849.5(3) keV	2.6(6) keV

Table 5.1: Table showing the fit results. In the third column the total number of events is shown. In the last two columns the fit results of $T_{p,\perp}$ and ε are shown. The errors on $T_{p,\perp}$ is only from the fit procedure and do not include the calibration errors.

For comparison with the theory from section 5.1.2, we use equation 5.19. We are forced to use this approximation, even though the condition $T_{\beta,max} \gg m_\beta$ is not completely fulfilled, because we do not know the response function well enough to make a better approximation. From equation 5.4, we can conclude that the absolute value of the maximal kinetic shift is:

$$t_{max} = k\, p_{\nu,max} = k\, T_{\beta,max} \tag{5.21}$$

The maximal kinetic shift (t_{max}) is not an average value, but an extreme value only established under certain kinematic conditions. Thus, equation 5.19 can be rewritten as:

$$\bar{t} = -t_{max} \cos\theta_{p\beta} \left(\frac{3+2A}{12}\right) \tag{5.22}$$

The approximation $T_{p,D} \cong T_{p,\perp}$ is used in calculating t_{max}, i.e. the kinetic energy in the frame of the β-daughter nucleus is approximately equal to the mean proton kinetic energy at $\theta_{p\beta} = 90^o$ in the laboratory frame. We can hereby use that:

$$t_{max} = k\, T_{\beta,max} \cong \frac{\sqrt{2m_p T_{p,\perp}}}{M} T_{\beta,max} \tag{5.23}$$

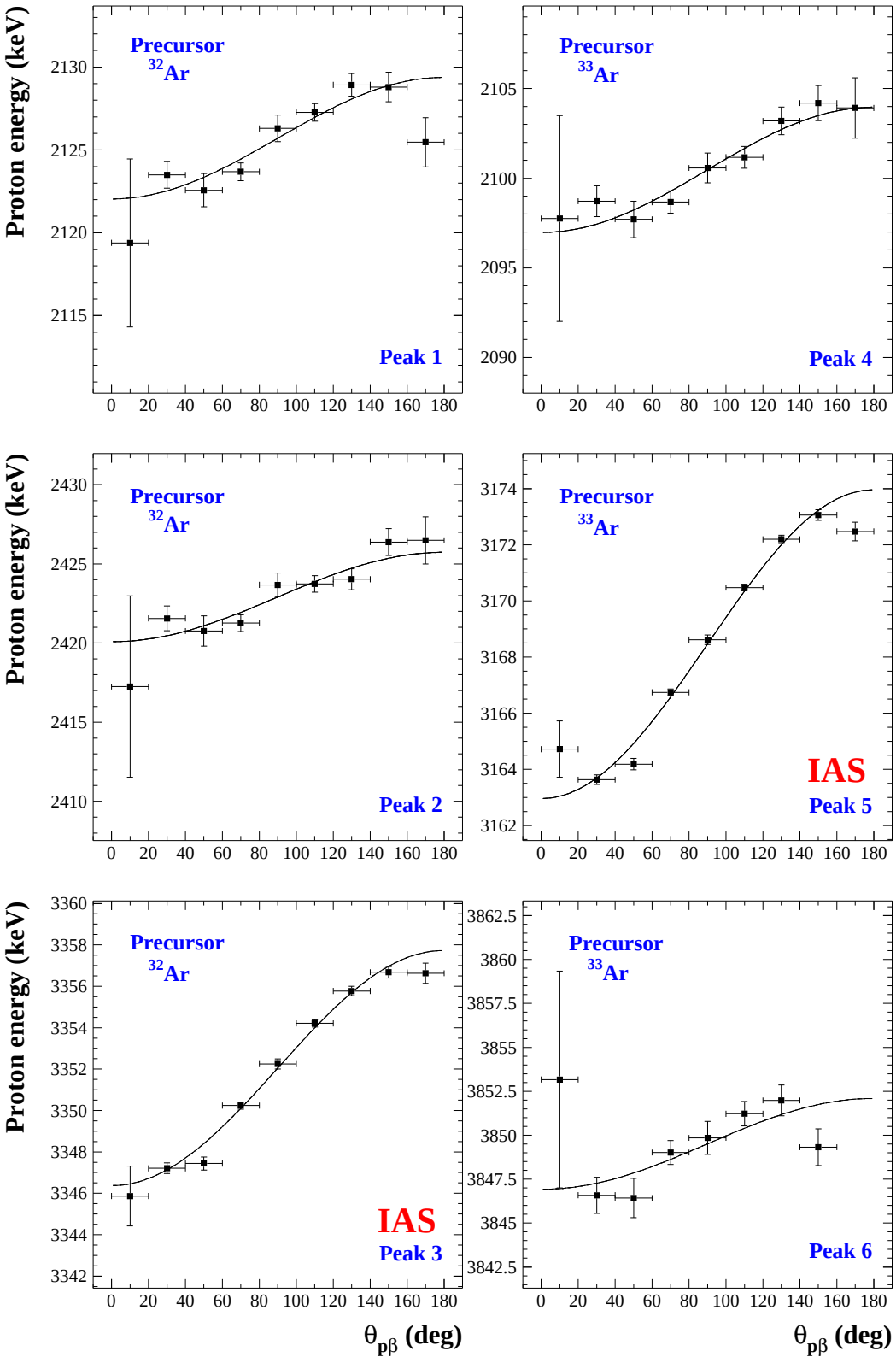

Figure 5.4: The kinetic energy shift. In all, there are 6 peaks, three from each of the two precursors ^{32}Ar and ^{33}Ar. The displayed curves are functions fitted to the data.

The assignments of the β-delayed protons in the 6 peaks are taken from Schardt and Riisager [34] and Björnstad *et al.* [31]. The assignments are shown in table 5.2. Q-values and excitation levels used to calculate $T_{\beta,max}$ are taken from Endt [46]. In calculating k, mass excesses are taken from Audi and Wapstra [7]. In appendix C, one can see how the triple correlation coefficient A is calculated.

Table of assignments						
No.	$T_{p,\perp}$	$T_{\beta,max}$	t_{max}	β-decay	p-emission	A
1	2126(2) keV	6369(22) keV	13.50(5) keV	$0^+ \to 1^+$	$1^+ \to 1/2^+$	-1/3
		5112(22) keV	10.84(5) keV	$0^+ \to 0^+$	$0^+ \to 3/2^+$	1
2	2423(2) keV	6057(21) keV	13.71(5) keV	$0^+ \to 1^+$	$1^+ \to 1/2^+$	-1/3
3	3352(3) keV	5112(22) keV	13.61(6) keV	$0^+ \to 0^+$	$0^+ \to 1/2^+$	1
4	2100(2) keV	6146(7) keV	12.560(16) keV	$1/2^+ \to 1/2^+$	$1/2^+ \to 0^+$	-1/3
		6120(7) keV	12.509(16) keV	$1/2^+ \to 3/2^+$	$3/2^+ \to 0^+$	1/3
5	3168(2) keV	5040(7) keV	12.651(18) keV	$1/2^+ \to 1/2^+$	$1/2^+ \to 0^+$	1
6	3850(3) keV	4336(8) keV	12.00(2) keV	$1/2^+ \to 1/2^+$	$1/2^+ \to 0^+$	-1/3

Table 5.2: Table showing the assignments. Unfortunately two of the peaks have small overlapping peaks. The parameter $T_{p,\perp}$ is taken from table 5.1, but now the calibration errors are included. $T_{\beta,max}$ is a calculated value and t_{max} is calculated by knowing $T_{p,\perp}$ and $T_{\beta,max}$. In the fifth column, the spin(parity) of the β-decay is shown, and in the sixth, the spin(parity) of the proton emission. In the last column, the triple correlation coefficient A is displayed. $A = 1$ for Fermi decays, $A = -1/3$ for Gamow-Teller decays with delayed s-wave protons ($L = 0$) and $A = 1/3$ for Gamow-Teller decays $1/2^+ \to 3/2^+$ with $L = 2$ protons emitted in the decay $3/2^+ \to 0^+$. The assignments are taken from Schardt and Riisager [34] and Björnstad *et al.* [31].

Notice that in table 5.2, peak 1 is assigned to by mainly s-wave protons from the decay $1^+ \to 1/2^+$ ending up in the ground state of ^{31}S. However, a small part of these protons originate in the decay of the IAS in ^{32}Cl to the first exited state of ^{31}S ($0^+ \to 3/2^+$). These protons are as a minimum $L = 2$ protons, but since the beta decay to the IAS is a Fermi decay we anyhow have $A = 1$. In [58] the branching ratios of these decays are listed as 4.3(5)% for the decay: $1^+ \to 1/2^+$ and 0.2(1)% for the decay: $0^+ \to 3/2^+$. In Schardt and Riisager [34], one can see that peak 4 is actually also two peaks, both peaks are originating from Gamow-Teller decays. The dominating peak comes from the decay $1/2^+ \to 1/2^+ \to 0^+$, and the other decay is a $1/2^+ \to 3/2^+ \to 0^+$ decay.

Moreover, in Schardt and Riisager [34] there is a small misprint in table 1. The peak 2121(2) keV which is assigned to by a part of the decay sequence $1/2^+ \to 3/2^+ \to 0^+$, must at least have $L = 2$ protons, we can therefore deduce that

$A = 1/3$ and not $A = -1/3$.

According to Endt [58], the branching ratios of the decays $1/2^+ \rightarrow 1/2^+ \rightarrow 0^+$ and $1/2^+ \rightarrow 3/2^+ \rightarrow 0^+$ in peak 2100 keV are respectively 2.89(2)% and 0.423(8)%.

In table 5.3 and figure 5.5, you can see a comparison of the measured amplitude of the kinetic shift (ε), divided by t_{max} and the theoretical expectations. The values fit very well, actually a lot better than one could expect of the very rough model. In the two special cases i.e. peaks 1 and 4, the values are corrected for the overlapping peaks. The correction is done on the theoretical values. However, the error on the simple model is not included and an estimate of this error is $m_\beta/T_{\beta,max}$. From the

The triple-correlation coefficient			
No.	ε/t_{max}	(3+2A)/12	A
1	0.27(3)	0.200(3)	-1/3 (1)
2	0.21(3)	0.19444	-1/3
3	0.417(11)	0.41667	1
4	0.28(4)	0.2085(3)	-1/3 (1/3)
5	0.435(8)	0.41667	1
6	0.22(5)	0.19444	-1/3

Table 5.3: Comparison with theory. It can be seen that the values of the second and the third column fit very well. We can those conclude that the shown assignments are in full agreement with the measured kinematic shifts. Notice that the theoretical values in peaks 1 and 4 are corrected for overlapping peaks. Moreover, the errors coming from the approximations done in the simple model are not included.

comparison we can conclude that the assignments are consistent with this analysis. More specifically we can recognize peaks 3 and 5 as Fermi-decays to the isobaric analog states (IAS) and the other 4 peaks as mainly Gamow-Teller decays followed by s-wave emission. Since the excitation energy of the intermediate state in the β-daughter nucleus affects the value of $T_{\beta,max}$ ($T_{\beta,max} = Q_\beta - E_x$), it is also a test of this assignment.

5.3 The new method and previous results

In the previous section, a method for the investigation of the kinetic energy shift of β-delayed protons was outlined. The method is based on the measurements of the proton kinetic energy and the angle between the β-particle and the proton while the unobserved β-energy and the direction of the neutrino are averaged out. The investigation was used to deduce the p-β-ν angular correlation, and hence the β-ν

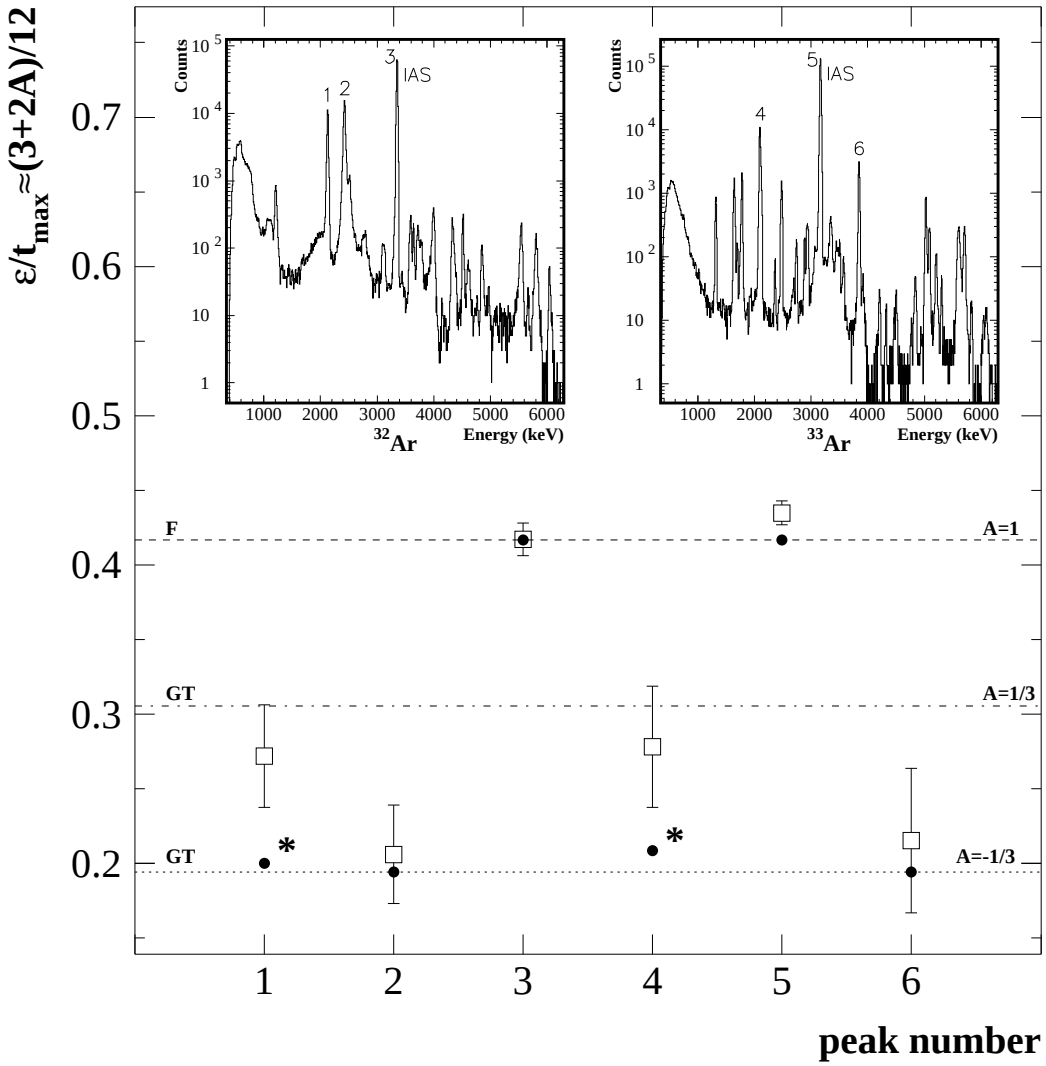

Figure 5.5: Comparison with theory. In the main part of the figure, you can see the experimental results of ε/t_{max} as open squares. The theoretical points $(3+2A)/12$ are shown as black dots. The black dots for peaks 1 and 4 are marked by an asterisk because they are changed by overlapping peaks. Moreover, it is seen that this correction does not explain the main deviation of the peaks 1 and 4. However, the error of the simple model is not included, therefore all the deviations are reasonable. In the upper left corner, the spectrum of ^{32}Ar is displayed and in the upper right corner that of ^{33}Ar. In the spectra the 6 studied peaks are emphasized.

angular correlation.

Two principal different methods have previously been used. In the first technique one only measures the kinetic energy of the β-delayed particle. By studying the line broadening one can deduce the triple correlation coefficient. This technique was used for instance by Macfarlane *et al.* [59], Nyman *et al.* [60] and Schardt and

Riisager [34]. This technique has the advantage of good statistics, but it also has many drawbacks. For instance, a high detector resolution is necessary and the spectral line-shapes may easily be distorted by drifts in the electronics and by source thickness effects [54]. Moreover, one has to take the natural line shape (Breit-Wigner distribution) into account, include the recoil broadening and thereafter fold the distribution with the detector response (approximately a Gaussian). This is a complicated procedure. Imagine you have found an error in the final result, it is then hard to deduce where in the calculations the error arose.

The second technique requires coincident measurements of the β-particle and the delayed particle. This kind of experiment was used for instance by Barnes *et al.* [61] in the special decay: $^{8}\mathrm{Li} \rightarrow \beta^{-} + \alpha + \alpha$, and by McKeown *et al.* [62] in a study of the decays: $^{8}\mathrm{Li} \rightarrow \beta^{-} + \alpha + \alpha$ and $^{8}\mathrm{B} \rightarrow \beta^{+} + \alpha + \alpha$. Furthermore, this technique was also used in an experiment performed on ^{20}Na by Clifford *et al.* [57, 54], and in the research presented in this thesis. This is to my knowledge the first time this technique has been used on β-delayed protons.

In this technique, the kinematic shift is measured as a function of one or more parameters of the β-particle, for instance the angle between the β-delayed particle and the β-particle. Thus, here one is looking for a difference in the proton energy between events with different values of the β-parameters. Moreover, the measurements of the kinematic shift with different values of the β-parameters are done simultaneously, which makes this technique insensitive to gain drifts or target thickness effects [54].

However, the β-particle and the proton are observed in coincidence, which means that the number of events are strongly reduced. Besides, good statistics is needed to successfully perform the averaging. It is thus not entirely without problems to use this method.

Clifford *et al.* measured both the kinetic energy of the β-delayed particle and the β-particle, and the angle between the β-particle and the β-delayed particle ($\theta = 45^{o}, 90^{o}, 180^{o}$), and from this they deduced the triple correlation coefficient. It is difficult to determine the β-particles energy, one has to know the response function of the detector very well. Since the neutrino is unobserved they needed to average over many events to find the mean shift for a given angle between the β-particle and the β-delayed particle. It is therefore not with great losses, if one takes the averages over the beta energy spectrum as well.

In my investigation, I have therefore averaged the kinetic energy shift of the β-delayed protons over the β energy spectrum as well as over the unobserved neutrino direction. Moreover, it has been proven possible to use a simple approximation,

that makes it unnecessary to know the detectors response function for positrons. In this way, a relatively easy method for qualitative measurements of spin and isospin is achieved. This is what I have called the new method.

Chapter 6

Half-life determination of ^{31}Ar, ^{32}Ar and ^{33}Ar

Figure 6.1: Half-life of ^{31}Ar

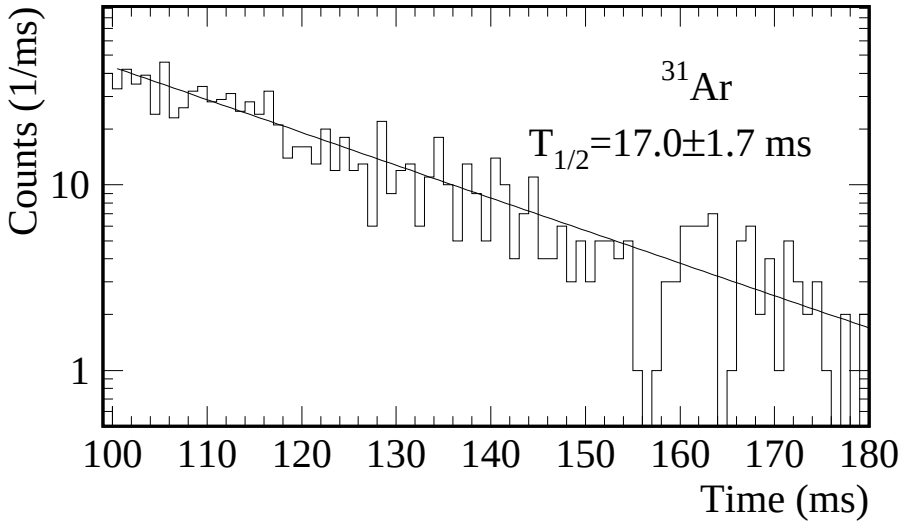

This experiment is not intended as an experiment for half-life measurements, nevertheless it is possible to use the "clocks", to make quite precise half-life determinations. For background exclusion, an energy window is used for each of the three isotopes. For the ^{33}Ar isotope the energy window is put around the peak at 3168 keV*, for ^{32}Ar is it put around 3354 keV† and for ^{31}Ar the window is around

*This proton energy is descended from the decay of the isobaric analogue state (IAS) in ^{33}Cl, to the ground state in ^{32}S.

†This proton energy comes from the decay of the isobaric analogue state (IAS) in ^{32}Cl, to the ground state in ^{31}S.

the peak at 5280 keV*. In figure 6.1, 6.2 and 6.3, the results of this analysis are shown.

Figure 6.2: Half-life of ^{32}Ar

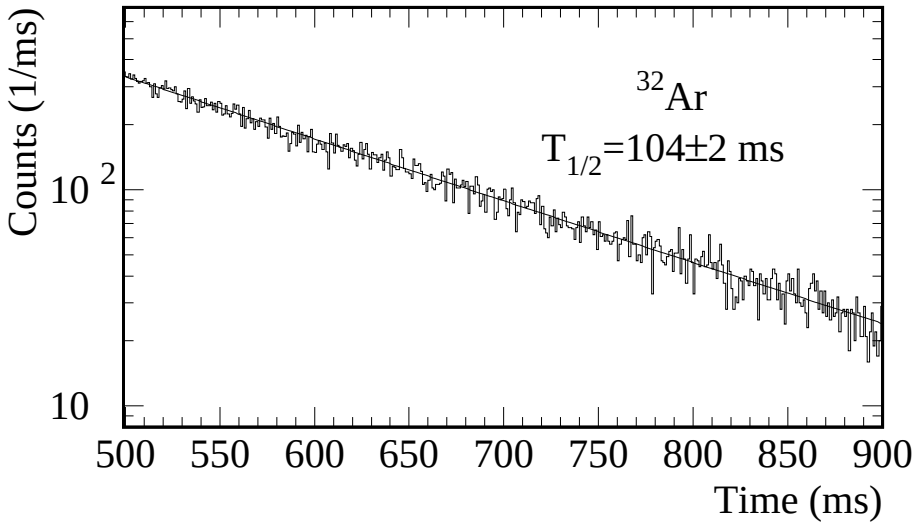

Figure 6.3: Half-life of ^{33}Ar

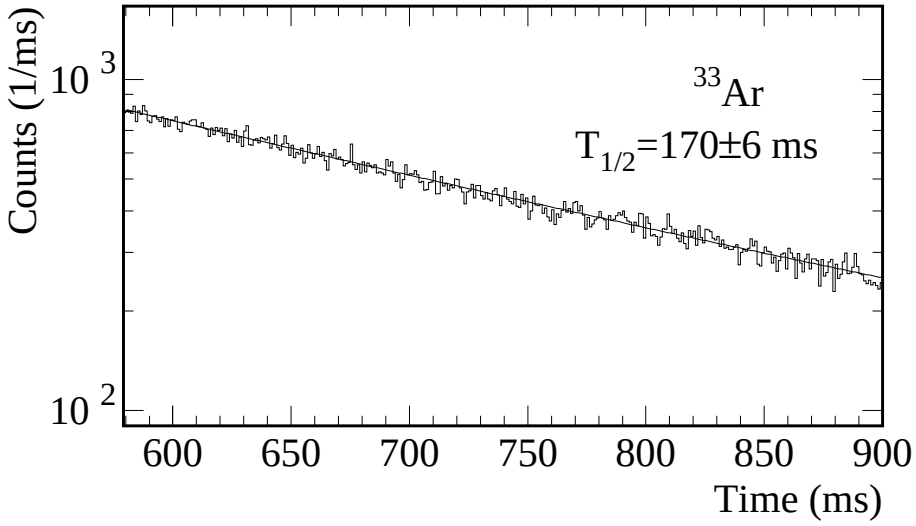

The results are very fine, the shown uncertainties are statistical and originate in the exponential fit with a constant background. The fitting procedure is minimization of an approximated χ^2 function. The χ^2 function is based on the Maximum

*This proton energy is descended from the decay of an excited state in ^{31}Cl, to the ground state in ^{30}S.

Likelihood function of Poisson distributed elements, a more detailed explanation is given in appendix D.

In all three cases it has been necessary to include only a part of the time interval. First of all, we are forced to exclude the first 100 ms, this time interval is the beam-gate. Secondly, there has been some destruction of the decay spectrum caused by a time delay in the data-buffer transport. This effect makes the spectrum look like it has some bumps, therefore these time-intervals are excluded. This effect yields small systematic errors which are not included, an estimate of the size of these errors is 2 ms.

Table 6.1: Half-lives of argon isotopes

Half-life		
^{31}Ar	^{32}Ar	^{33}Ar
17.0(17)ms[a]	104(2) ms[a]	170(6) ms[a]
15.1(12)ms[b]	98(2) ms[d]	174.1(11)ms[f]
15(3) ms[c]	75(50) ms[e]	173(2) ms[g]

[a] This work.
[b] Bazin *et al.* (1992) [19]
[c] Borrel *et al.* (1987) [15]
[d] Björnstad *et al.* (1985) [31]
[e] Hagberg *et al.* (1977) [36]
[f] Borge *et al.* (1987) [32]
[g] Hardy *et al.* (1971) [33]

In table 6.1, the result of this experiment is compared with previous experiments. It is seen that the new results fit very well with the previous values.

Chapter 7

The decay of ^{31}Ar

In this chapter the results of the experimental examination of ^{31}Ar are presented. This isotope has been studied previously, see section 2.4. The most recent experiment is described in [20, 21]. In that investigation, the decay scheme, and especially the β-delayed two-proton decay, was not fully understood, this is why the experiment has been repeated.

Figure 7.1: Spectrum of ^{31}Ar

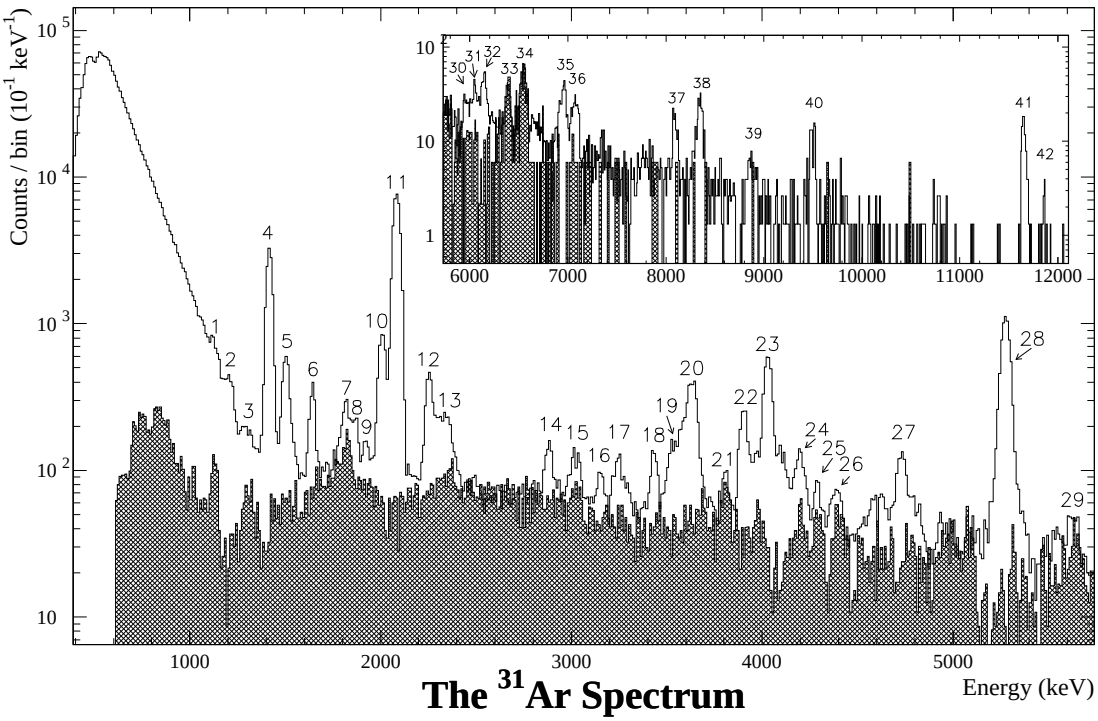

7.1 The β-delayed single proton spectrum

In figure 7.1, the single proton spectrum and the two-proton spectrum are displayed. The two-proton spectrum is the spectrum of all coincident two-proton events and it is plotted as a hatched curve in the foreground of the figure, and the single proton spectrum is displayed in the background. The two-proton spectrum is scaled up to correct for the difference in detection efficiency and is constructed by Fynbo [1].

Each clear peak in the single proton spectrum has a number, in all 42 peaks are observed. Of course, in between these peaks there are also many unresolved peaks. The major bulge at low energies is the β-background, and the number of β counts with energy larger than 1200 keV is strongly reduced, wherefore the majority of counts above 1200 keV are protons.

From figure 7.1, one can observe that in the part of the single proton spectrum roughly above 1200 keV the majority of counts in the smoothed background are protons coming from β-delayed two-proton emissions. The investigation presented here is mostly on the β-delayed single proton emission. The investigation on the β-delayed two-proton emission will be presented in [1].

Out of the 42 peaks in this single proton spectrum some are identified as the first emitted proton in a β-delayed sequential two-proton emission, namely number 1,3,7,9,21,24,25,26,29,30,33 and 34. This conclusion can be drawn for the majority of these peaks by inspecting figure 7.1.

The single proton spectrum is constructed on the basis of hits in the strip detector because the strip detector has a resolution on 17.2(14) keV (FWHM), which is a lot better than the FUTIS detectors resolution, which is estimated to be about 30 keV. All hits with an energy difference between the front and the back strip larger than 31 keV* are excluded, this cut is included because it reduces charge loss effects in the strip detector. See section 4.3 for more details about the charge loss effects in the strip detector. Moreover, any event investigated in this chapter has to fulfill a time gate condition on less than 170 ms from production to observation.

The insert in the upper right part of figure 7.1 is constructed by the method of correction for high energy protons which is explained in section 4.4. In this insert, the protons are repeatedly measured which means that they are first detected in the strip detector and afterwards in the ESI detector. Thus, in this insert all β-particles are excluded by the methods described in section 4.4. Moreover, the ESI

*The 31 keV is equal to 3 times the resolution of the difference in energy of the strips (3σ) which correspond to a 99.7 % confidence level, see section 4.2.3 for more details.

detector covers only 76(6) % of the strip-detector's solid angle. The intensities of protons detected in the strip-ESI telescope system are therefore multiplied by a factor 1.32(11).

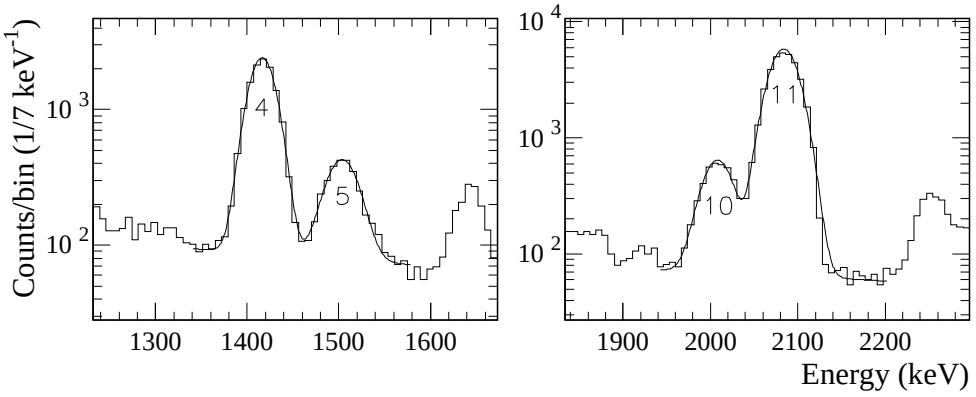

Figure 7.2: Examples of the fitting procedure. The two parts of this figure show the spectrum in the region around peaks 4 and 5, and around peaks 10 and 11. All of these peaks belong to the category of intensive peaks. In the two parts of this figure the experimental data is shown as histograms, and the fitting results are displayed as continuous curves.

In figure 7.2, two examples of the fitting procedure are shown. Each peak is fitted to a Gaussian with a linear background. Sometimes the peaks are very close in energy which makes it necessary to include more than one peak in the fit. Thus, up to three peaks are sometimes included in a single fit. The natural lineshape of a proton peak is of cause not a Gaussian but has a Breit-Wigner form*. However, the natural lineshape is broadened as a consequence of the recoil broadening and the broadening effects in the detector, which make the final lineshape look approximately like a Gaussian. Hence, there is a small bias, which over estimates the center of the peaks in favour of the wings of the distribution, however this bias is quite small.

Since the measurements of the radioactive nuclei are achieved by counting events, the counts in the histograms are distributed according to Poisson statistic. The fitting and the uncertainties are therefore based on the Poisson likelihood χ^2-function derived by Baker and Cousins [63]. This statistical method is described in details in appendix D.

In table 7.1, the observed peaks in the β-delayed single proton spectrum are shown. The results are compared with the results obtained in Axelson *et al.* [21].

*The Breit-Wigner form is identical to the Lorentzian lineshape.

	Present work			From Axelson et al. [21]	
No.	E (keV)	σ (keV)	Intensity	E (keV)	Intensity
1	1131(5)	20(7)	2.7(16)	1133(15)	2.0(4)
2	1211(4)	17(3)	1.7(5)	1212(9)	1.0(3)
3	1300(13)	27(21)	0.7(11)	1289(9)	1.0(2)
4	1416(2)	13.92(16)	34.0(3)	1415(5)	37.4(12)
5	1504(2)	17.0(6)	6.2(2)	1502(10)	7.0(6)
6	1643(2)	12.8(6)	2.88(14)	1641(8)	3.0(6)
7	1819(3)	23(3)	3.0(4)	1814(10)	3.3(7)
8	1870(3)	11(2)	0.8(2)		
9	1923(3)	11(3)	0.44(14)		
10	2008(2)	16.5(4)	10.0(2)	2010(8)	10.8(10)
11	2084(2)	16.55(14)	100.0(6)	2081(3)	100(3)
12	2253(2)	14.9(9)	4.0(3)	2265(25)	5(2)
13	2327(4)	41(3)	5.1(4)		
14	2881(3)	16(2)	0.99(13)	2866(20)	1.7(9)
15	3020(3)	22(2)	1.08(14)		
16	3153(4)	14(2)	0.44(10)		
17	3249(4)	25(3)	1.17(15)	3242(12)	2.2(8)
18	3432(3)	14.2(16)	0.89(11)	3416(12)	1.4(3)
19	3561(11)	42(7)	3.6(8)	3534(10)	2.4(4)
20	3634(3)	24.7(16)	6.1(8)	3624(9)	9.2(7)
21	3806(4)	16(3)	0.53(13)		
22	3902(3)	15.8(9)	2.22(14)	3903(9)	3.5(6)
23	4030(3)	17.6(5)	7.0(2)	4027(6)	8.9(8)
24	4200(4)	20(3)	1.09(18)	4187(9)	2.6(7)
25	4289(4)	10(3)	0.31(8)		
26	4389(5)	22(4)	0.59(11)	4386(12)	1.2(2)
27	4730(5)	24(3)	1.68(18)	4743(9)	1.7(3)
28	5276(5)	21.9(4)	17.6(3)	5280(7)	20.6(9)
29	5632(6)	20(4)	0.37(9)	5686(9)	0.31(5)
30	5952(7)	15(5)	0.19(6)		
31	6049(9)	36(10)	0.51(12)		
32	6145(7)	20(3)	0.51(12)	6175(12)	2.8(12)
33	6386(7)	12(2)	0.26(5)		
34	6540(8)	27(3)	0.84(11)	6555(11)	1.1(2)
35	6950(9)	31(3)	0.70(9)	6960(13)	1.4(3)
36	7074(9)	29(3)	0.49(7)	7100(13)	0.7(2)
37	8092(14)	23(3)	0.25(4)	8095(12)	0.55(14)
38	8347(15)	30(3)	0.51(6)	8342(14)	0.82(16)
39	8860(19)	55(27)	0.22(19)		
40	9493(20)	37(4)	0.30(4)	9379(13)	0.33(20)
41	11654(28)	20.3(13)	0.27(4)	11657(25)	0.23(11)
42	11858(29)	8.97(13)	0.034(3)		

Table 7.1: Peaks in the ^{31}Ar spectrum. In the first column, the peak numbers are displayed. In all, 11 new peaks have been observed. In the second column, the kinetic energies of the proton peaks are shown, and in the third the observed widths σ are displayed. In the forth column, the relative intensities are shown. In this column, peak number 11 is normalized to have a relative intensity of 100. In the last two columns, the results obtained in Axelson *et al.* [21] are displayed for comparison. The new results are concordant with the results of Axelson *et al.* [21].

7.2 Constructing a decay scheme

When a decay scheme has to be constructed, a list of criteria that can be used to assign which proton energy belongs to which transition is essential. In our case, the β-delayed two-proton daughter nucleus is ^{29}P. ^{29}P has well known low energy levels which are taken from [46]. The energy levels in the β-delayed single-proton daughter nucleus ^{30}S are taken from Paddock [64] and Yokota *et al.* [65], except for a few new levels observed in our investigation.

Out of these energy levels and the proton kinetic energies observed in the single proton spectrum, one can deduce some of the energy levels in the β-daughter nucleus ^{31}Cl. In the following, a sorted list of criteria are given in such a way that the most important criteria are mentioned first.

7.2.1 Assignment criteria

p-p coincidences: In cases with a two-proton coincidence, we can calculate the state fed in ^{31}Cl from the two-proton daughter state which most frequently are the ground or the first excited state in ^{29}P.

p-γ coincidences: If a gamma transition in ^{30}S is seen in coincidence with a proton emission, we can deduce which level in ^{30}S is fed by the β-delayed proton emission, and thereby find the level in ^{31}Cl fed by the β-decay. As well as the existence of a coincidence, the lack of coincidences can be used in assignments.

Energy coherence: The simple puzzle of known proton energies and states in the proton daughter nucleus can be used as an argument for an energy level in the nucleus ^{31}Cl.

Mirror nucleus: For the low lying state in $^{31}_{17}\mathrm{Cl}_{14}$, one has an idea of where the states ought to be by looking at the mirror nucleus $^{31}_{14}\mathrm{Si}_{17}$.

Of course, it is not alway easy to make the assignments and some of them are not that reliable. Which means that the result presented is more considered as a proposal than a final determination. Beside these criteria, the selection rules for proton emission, β-decay and γ-decay have been used, and they are summarized in appendix E.

7.2.2 β-delayed two-proton emission

In [1], the full investigation of the β-delayed two-proton emission will be presented. In each β-delayed two-proton event the energy of the protons and the angle between them can be used to derive the recoil energy of the final nucleus and hence reconstruct the full decay energy (Q_{2p}) of the event. One can then pick out a specific Q_{2p}-value to study the multiplicity 2 events with precisely that Q_{2p}-value. This is the main method used in [41, 1]. The Q_{2p}-value is given by [41]:

$$Q_{2p} = E_1 + E_2 + \frac{m_p}{M_F}\Big(E_1 + E_2 + 2\sqrt{E_1 E_2}\, cos\,\theta_{pp}\Big) \tag{7.1}$$

This formula is a consequence of energy and momentum conservation in non-relativistic two-proton emission. The parameters E_1 and E_2 are the kinetic energies of the two emitted protons. The masses m_p and M_F are respectively the proton mass and the mass of the final nucleus. θ_{pp} is the angle between the two emitted protons. Instead of using the Q_{2p}-method, I have chosen to proceed in another way in this thesis, just to double check the results obtained in [1].

In all the investigated β-delayed two-proton data from ^{31}Ar, no evidence for direct two-proton emission was found. Instead, it is possible to assign the majority of the observed two-proton events to sequential two-proton decays [1]. Moreover, in the observed β-delayed two-proton events of ^{31}Ar, the energy of the first emitted proton is nearly always larger than the energy of the second emitted proton. I have therefore tried to make two histograms for the multiplicity 2 events. One containing the maximum energy of the two hits and one containing the minimum energy. Hence, the spectrum with the maximum energy most frequently contains the energy of the first emitted proton and the minimum energy spectrum contains that of the second emitted proton.

Of course, I have also included a low energy cutoff of 600 keV to reduce β-p coincidences, and a limit on 31 keV on the energy difference of the front and the back strip to reduce interstrip effects.

In sequential two-proton emission, the first emitted proton is emitted from a nucleus at rest, wherefore the lineshape of the first emitted proton is narrow. However, the second emitted proton is emitted from a nucleus in motion and has therefore a Doppler broadened lineshape. We therefore expect narrow peaks in the maximum energy spectrum and broad coincident peaks in the minimum energy spectrum.

We can thus pick out a peak in the maximum energy spectrum and put an energy window on the selected peak. By observing the coincident hits with the se-

lected peak, one can observe the recoil effect. Notice that this recoil shift is roughly of the order 100-200 keV, the recoil from the β-decay can therefore be neglected in this study. A calculation similar to the one used in deriving equation 5.3 and 5.4, wherein non-relativistic kinematic is used, gives the following result for the kinetic energy of the second emitted proton in a sequential two-proton emission:

$$E_2 = E_2^{'} + Q_1^{'} - 2\sqrt{E_2^{'} Q_1^{'}}\, cos\,\theta_{pp} \tag{7.2}$$

The energies $Q_1^{'}$ and $E_2^{'}$ are given by:

$$Q_1^{'} = Q_1 \left(\frac{m_p}{M_D}\right)^2 \qquad\qquad E_2^{'} = \frac{Q_2}{1 + m_p/M_F} \tag{7.3}$$

Where the Q-values of respectively the first and second emitted proton are Q_1 and Q_2, and the mass of the single proton daughter nucleus is M_D. Notice that $E_2^{'}$ is the energy of the second emitted proton in the rest frame of the single proton daughter nucleus.

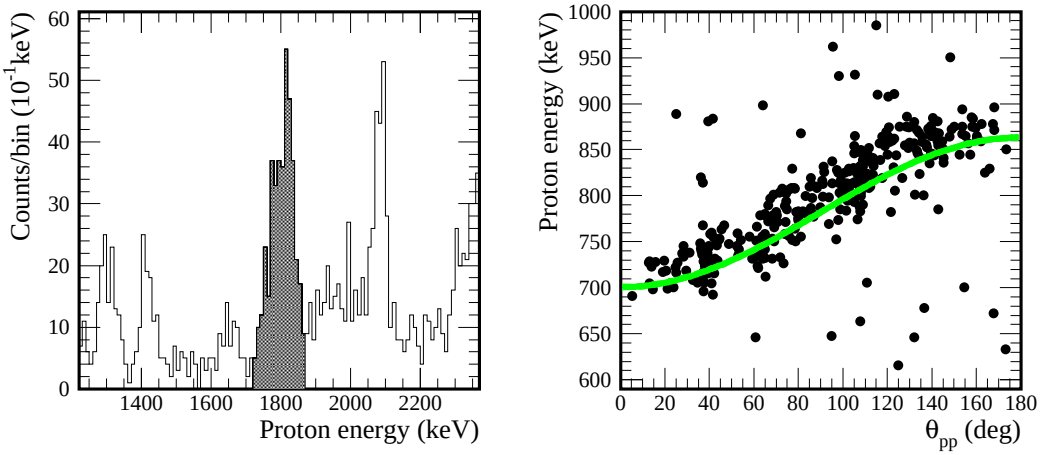

Figure 7.3: The Doppler shift in 2p emission. In the left part of this figure, a cutout of the maximum energy spectrum is shown. The first emitted proton energy is restricted to the interval 1723-1864 keV, as illustrated by the hatched peak. This peak is in the region of peak 7 in the single proton spectrum. In the right part of the figure, the coincident minimum proton energies are plotted as a function of the angle between the two protons. One can clearly see the energy shift. Moreover, a theoretical curve overlapping the data points is plotted, which is in full agreement with the energy shift. The theoretical curve is plotted with: $Q_2 = 807$ keV and $Q_1 = 1880$ keV.

We will now go to some examples using this method to investigate sequential two-proton emission. The first example is shown in figure 7.3.

In the left part of the figure, an energy window is put on the hatched peak. In the right part of the figure, the coincident hits of the hatched peak are shown in a plot of the energy as a function of the angle between the two hits.

One can without doubt see the clear energy shift in the right part of figure 7.3. However, the peak hatched in the left part of figure 7.3 is rather broad. This is because the selected peak originates in a group of close lying levels in ^{31}Cl fed by the β-decay. In order to be completely sure of the structure of this particular two-proton emission, I have plotted the energy of the first emitted proton as a function of the angle between the two protons. This plot is displayed in figure 7.4.

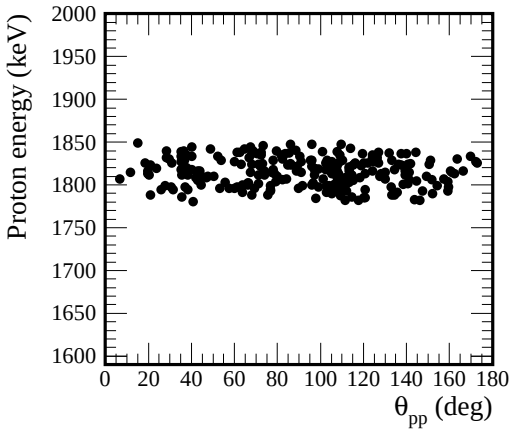

Figure 7.4: The kinetic energy of the peak: 1723-1864 keV in the maximum energy spectrum as a function of the angle between the coincident emitted protons. No significant energy shift is observed.

The plots shown in figure 7.3 and 7.4 are very clear evidences for the sequential structure of this particular β-delayed two-proton emission, and so far I have not seen any illustration that shows β-delayed sequential two-proton emission more clearly.

The next example is the peak at 2041-2115 keV in the maximum energy spectrum. This peak is at the same place as peak 11 in the single proton spectrum, which is the most intensive peak in the single proton spectrum. It is therefore not expected to originate from true 2p-coincidences, but rather p-β coincidences. The result of the investigation of peak 11 is shown in figure 7.5.

As expected, this peak originates from p-β coincidences, wherefore this method equally can be used to reject wrong 2p-coincidences.

The last example shown here is the peak 3762-3836 keV which is seen as peak number 21 in the single proton spectrum. Figure 7.6 is made in the same way as

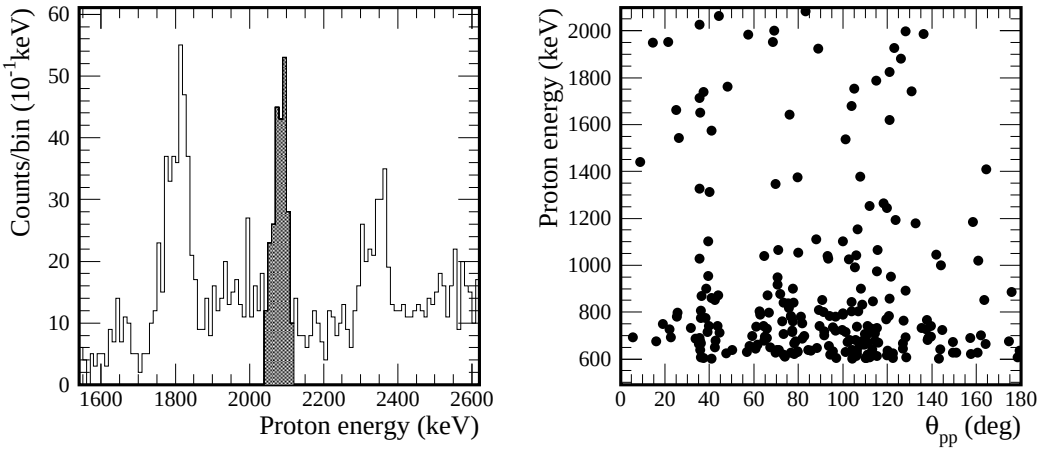

Figure 7.5: Second example of recoil shift in 2p emission. The figures are generated on multiplicity 2 events. To the left, the maximum energy spectrum is displayed and to the right, the minimum proton energy is plotted as a function of θ_{pp}. The maximum energy is restricted to 2041-2115 keV which is illustrated by the hatched peak. In the right part of the figure only coincident hits are included, and there is no significant accumulation of points on cosine curves. Moreover, the intensity of hits is highest closest to the low energy cutoff on 600 keV. The observed coincidences are therefore p-β coincidences.

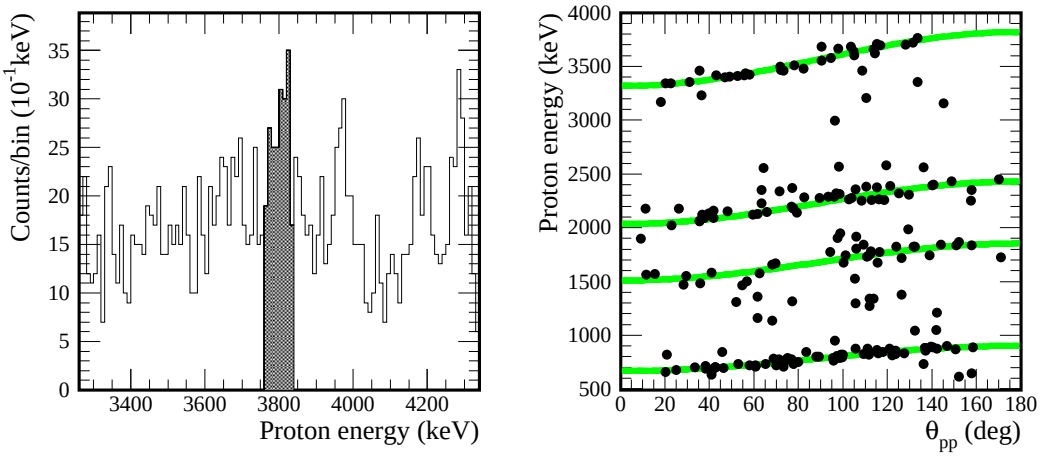

Figure 7.6: Third example of recoil shift in 2p emission. The hatched peak in the left part of the figure is restricted to 3762-3836 keV, in the right part of the figure 4 cosine curves have been identified and theoretical curves are plotted under the data points.

the previous two examples. The four theoretical curves in figure 7.6 are based on the following Q-values: Q_1=3933 keV and Q_2=807, 1735, 2305 and 3689 keV. Q_1 is calculated by using the observed proton energy of the first emitted proton which is equal to $E_1 = 3806(4)$ keV, and the Q_2-values are calculated by using the already known levels in ^{30}S and ^{29}P. An energy level in ^{30}S is only calculated on the basis

of the energy of a second emitted proton, if a new level in ^{30}S is observed, as for example in the case of the 8.09 MeV level.

For the coincidences observed in figure 7.6, the proposed decay scheme is displayed in figure 7.7. In this third example, we see another feature of the investiga-

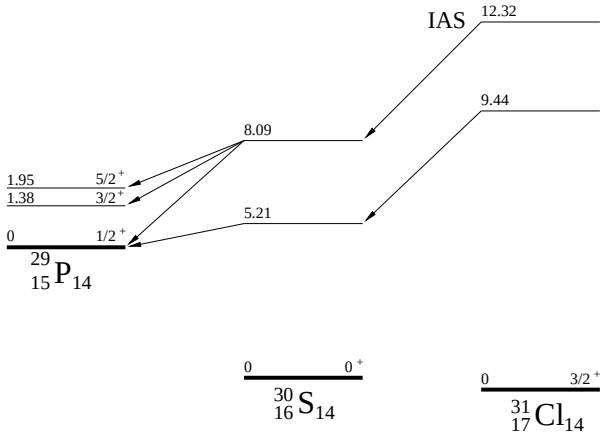

Figure 7.7: The proposed decay scheme for the observed 2p-coincidences in the third example. The energy level at 8.09 MeV is a new level which is observed in this investigation.

tion method. We can observe coincidences of a specific energy of the first emitted proton with second emitted protons going to the ground state, the first exited state and the second exited state at the same time. Cases like this therefore have much more reliable energy assignments.

In this way, all significant peaks in the maximum energy spectrum have been examined. In the interest of the investigation of the single proton spectrum, all the peaks already seen in the single proton spectrum are investigated. The results of this investigation are summaries in table 7.2.

In the research presented in table 7.2, the energy levels in ^{29}P are taken from [46]. The energy levels of the β-delayed single-proton daughter ^{30}S are from Yokota *et al.* [65] and Paddock [64], except for the two new levels: 7.693(4) MeV and 8.089(2) MeV, which are observed for the first time [1]. Other peaks in the single proton spectrum are assigned to be mostly single proton peaks, however they may also originate in two-proton emission. This is the case for peaks 13, 14 and 15. Apart from this, peak 9 is a bit unsure.

Moreover, the level at 12.32 MeV is assigned to be the Isobaric Analog State (IAS). This assignment is partially based on shell model calculations [21]. The energy level at 12.32 MeV is a precursor of many two-proton emissions, which is in good agreement with the assumption that the energy level 12.32 MeV in

peak no.	^{31}Cl state	^{30}S state		^{29}P state	
1	6.67	5.21	(0^+)	0	$1/2^+$
3	6.84	5.21	(0^+)	0	$1/2^+$
7	7.39	5.21	(0^+)	0	$1/2^+$
9	7.50	5.21	(0^+)	0	$1/2^+$
21	9.44	5.21	(0^+)	0	$1/2^+$
	12.32	8.09		0	$1/2^+$
	12.32	8.09		1.38	$3/2^+$
	12.32	8.09		1.95	$5/2^+$
24	12.32	7.69		1.38	$3/2^+$
	12.32	7.69		1.95	$5/2^+$
25	12.32	7.57		1.38	$3/2^+$
26	12.32	7.48		0	$1/2^+$
26	12.32	7.48		1.38	$3/2^+$
29	12.32	6.22		0	$1/2^+$
30	12.32	5.91	(4^+)	0	$1/2^+$
33	12.32	5.43	(1,2)	0	$1/2^+$
34	12.32	5.21	(0^+)	0	$1/2^+$

Table 7.2: Table of assignments of two-proton emission. The table shows, the peaks in the single proton spectrum which has been assigned to be the first emitted proton of a β-delayed two-proton emission. The energy levels are listed of respectively the β-daughter nucleus ^{31}Cl, the one-proton daughter nucleus ^{30}S and the two-proton daughter nucleus ^{29}P. Only the principal branches are displayed. All energies are in MeV. The spin and parity of states in ^{30}S and ^{29}P are indicated if they are known.

^{31}Cl is the IAS of the ground state of ^{31}Ar. However, this subject is much more complicated. Because two-proton decays of the IAS to a $T = 1/2$ state in ^{29}P are actually isospin forbidden as a consequence of total isospin conservation (T). The decay can therefore only take place via small isospin impurities, for instance in the wavefunction of the IAS.

7.2.3 Coincidences with gamma rays

Only two gamma lines are observed in coincidence with protons, namely the 1192 keV and 2211 keV lines. In [66] a detailed study of the gamma spectrum from the decay of ^{31}Ar is presented. The known branching ratios of gamma decays in the nucleus ^{30}S are shown in figure 7.8.

The proton separation energy of ^{30}S is S_p=4400(3) keV [7], states above the shown levels in figure 7.8 will therefore most probably decay by proton emission if it is allowed by the selection rules. Two peaks in the single proton spectrum are

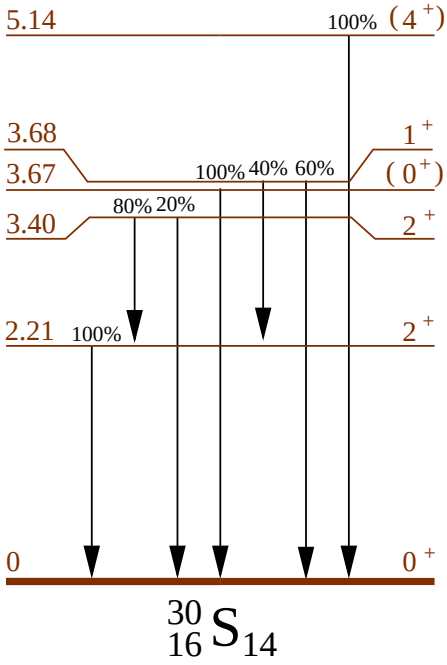

Figure 7.8: Gamma ray branching ratios of ^{30}S levels. The values are taken from [67]. Energy levels are given in MeV. The two observed decays are: the 2211 keV line from 2.21 MeV $\rightarrow$ 0 MeV and the 1192 keV line from 3.40 MeV $\rightarrow$ 2.21 MeV.

seen in coincidences with γ rays, these are peaks 10 and 19. Both proton energies are seen in coincidences with both the 1192 keV and the 2211 keV gamma rays. These two proton-decays are therefore most probably to the energy level 3.40 MeV in ^{30}S.

We only see two proton energies in coincidences with γ rays. Nevertheless it is possible to use the lack of coincidences in assignments. For instance, the very intensive proton peaks, with numbers 4, 11, 23 and 28 in the single proton spectrum, are neither seen in p-p coincidences or in p-γ coincidences*. These decays therefore have the ground state of ^{30}S as their final state.

Another criteria used in energy assignments is energy comparison, i.e. if two different decay branches are assigned to come from the same energy level, this energy level is probably a true level. I have made a FORTRAN routine that produces proposals for energy coherences, and these proposals have made it possible to make an assignment for each of the 42 peaks in the single proton spectrum. In table 7.3, a proposal is shown for the decay scheme to the 6 lowest levels in ^{30}S.

*Actually, there is a small underlying proton peak in 28, which comes from a two-proton emission.

		Final states (keV)					
No.	E	0	2210.6(5)	3402.6(5)	3666.3(13)	3676(3)	5136(2)
	(keV)	0^+	2^+	2^+	(0^+)	1^+	(4^+)
2	1211(4)						6677(4)
4	1416(2)	1754(3)					
5	1504(2)		4055(3)				
6	1643(2)			5390(3)			
8	1870(3)			5626(3)			
10	2008(2)			5768(2)$^\gamma$			
11	2084(2)	2444(2)					
12	2253(2)	2619(2)					
13	2327(4)	2695(4)					
14	2881(3)			6670(3)			
15	3020(3)		5623(4)				
16	3153(4)		5760(4)				
17	3249(4)	3649(4)					
18	3432(3)				7504(3)		
19	3561(11)			7373(11)$^\gamma$			
20	3634(3)	4046(4)					
22	3902(3)		6533(3)				
23	4030(3)	4455(3)					
27	4730(5)		7390(5)				
28	5276(5)	5743(5)					
31	6049(9)	6542(9)					
32	6145(7)	6642(7)					
35	6950(9)	7474(9)					
36	7074(9)	7602(10)					
37	8092(14)					12330(15)	
38	8347(15)			12320(16)			
39	8860(19)	9448(19)					
40	9493(20)		12313(21)				
41	11654(28)	12336(29)					
42	11858(29)	12547(30)					

Table 7.3: Proposed decay scheme to the 6 lowest levels in ^{30}S. The uncertainty on the energy levels do not include the error on the ground state difference of ^{30}S and ^{31}Cl. The proton separation energy of ^{31}Cl is S_p=290(50) keV [7]. Assignments of energy levels in ^{31}Cl made on the basis of p-γ coincidences are marked with a $^\gamma$.

7.2.4 Comparison with the mirror nucleus ^{31}Si

The lowest energy levels in $^{31}_{17}\mathrm{Cl}_{14}$ ought to be similar to the energy levels in the mirror nucleus $^{31}_{14}\mathrm{Si}_{17}$.

In figure 7.9, the lowest energy levels observed in ^{31}Cl are compared with energy levels in ^{31}Si. It follows from the comparison with the mirror nucleus, that the first exited state in ^{31}Cl ought to be at about 600-800 keV. However, it has not been possible to observe this proton peak because of the large β-background at low energies. Moreover, if the spin of the ground state of ^{31}Ar is $5/2^+$, which is a result we will return to in section 7.4, the transition to the first excited state with

$J^{\pi}=1/2^{+}$ is a second forbidden β-decay, which of course has a strongly reduced branching ratio compared to allowed decays. No forbidden β-decays are observed in this investigation, however it was also not expected.

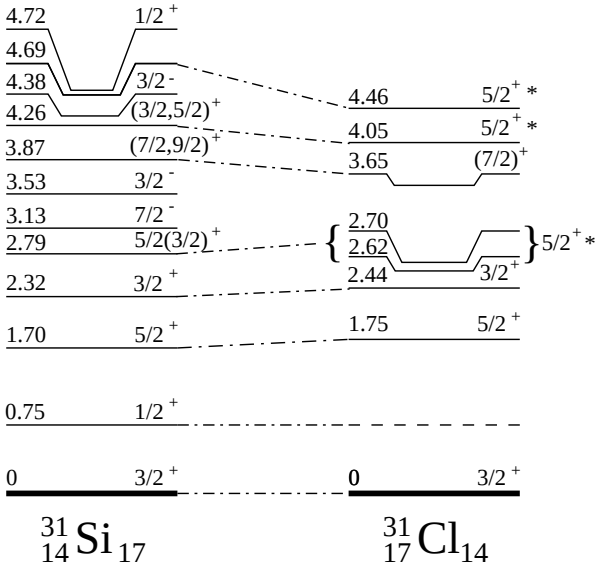

Figure 7.9: Low lying levels in ^{31}Cl and in the mirror nucleus ^{31}Si. The four levels marked with an asterisk have a spin assignment based on the investigation presented in section 7.4.1.

The second exited state in ^{31}Cl is on 1.75 MeV and the third exited state is on 2.44 MeV. These states are based on the very clear peaks 4 and 11, and their spin and parity are assigned by looking at the mirror nucleus. The next two levels at respectively 2.62 MeV and 2.70 MeV are a bit more doubtful, these levels originate in peaks 12 and 13. The energy level at 3.65 MeV is a companion to peak 17, and it is most probably a $7/2^{+}$ state since the transition to a $9/2^{+}$ state is a forbidden β-decay. The next energy level at 4.05 MeV is based on peak 20, and the energy level at 4.46 MeV originates in peak 23. The energy levels 2.62 MeV, 2.70 MeV, 4.05 MeV and 4.46 MeV are assigned to be $5/2^{+}$ states. These assignments are results of the investigation of the recoil energy shift in β-delayed proton emission, which is presented in section 7.4.1. All in all, the results fit well with the states known in the mirror nucleus ^{31}Si.

7.3 The decay scheme of ^{31}Ar

In the previous section, it was illustrated how the different transitions have been identified. The calculation of the branching ratios is problematic because the β-

decay to the ground state of ^{31}Cl is unobserved. Moreover, the total production rate of ^{31}Ar is not precisely measured in our experiment. We are therefore forced to use the results from previous experiments done at GANIL.

The branching ratios are found by using the observed branching ratios for the 2.1 MeV proton group measured in two previous experiments [17, 19]. In these earlier measurements, the energy resolution was not high enough to separate the peaks 2.008 MeV and 2.084 MeV. They measured that the 2.1 MeV proton group had a branching ratio on respectively 26(5)% in [17] and 30(3)% in [19].

The branching ratio to the ground state is taken from [20] and is on 23(8)% or 30(10)%, these values are derived by two different methods. In figure 7.10, a proposal for the decay scheme of ^{31}Ar is shown. Notice that the branching ratios are only for the β-delayed single proton branches.

The total β-delayed single proton branching ratio is 56(3)%. The feeding to the ground state of ^{31}Cl is 23(8)% [20], and the branching ratio of all the β-delayed two-proton emissions is 12(2)% [1]. Only 9(9)% of the decays are therefore not included in the assignments. Accordingly, only few events are lost in between unresolved energy levels. Moreover, we can conclude that the decay branches are well described by β-decay to the ground state, β-delayed proton emission and β-delayed sequential two-proton emission.

Table 7.4 shows the 19 energy levels proposed in ^{31}Cl and their single proton branching ratios.

No.	E_x (keV)	Intensity (%)	No.	E_x (keV)	Intensity (%)
1	1754(3)	8.9(8)	11	6534(3)	0.72(8)
2	2444(2)	26(2)	12	6669(2)	0.86(15)
3	2619(2)	1.05(12)	13	6841(17)	0
4	2695(4)	1.33(16)	14	7386(4)	1.4(2)
5	3649(4)	0.31(5)	15	7499(3)	0.42(5)
6	4052(2)	3.2(4)	16	7602(10)	0.13(2)
7	4455(3)	1.83(17)	17	9435(9)	0.06(5)
8	5390(3)	0.76(8)	18	12320(4)	0.35(4)
9	5624(2)	0.51(8)	19	12547(30)	0.009(1)
10	5762.5(18)	7.4(7)			

Table 7.4: Energy levels in ^{31}Cl. From the single proton data it has been possible to deduce in all 19 energy levels. The shown intensities include only the β-delayed single proton branching ratios.

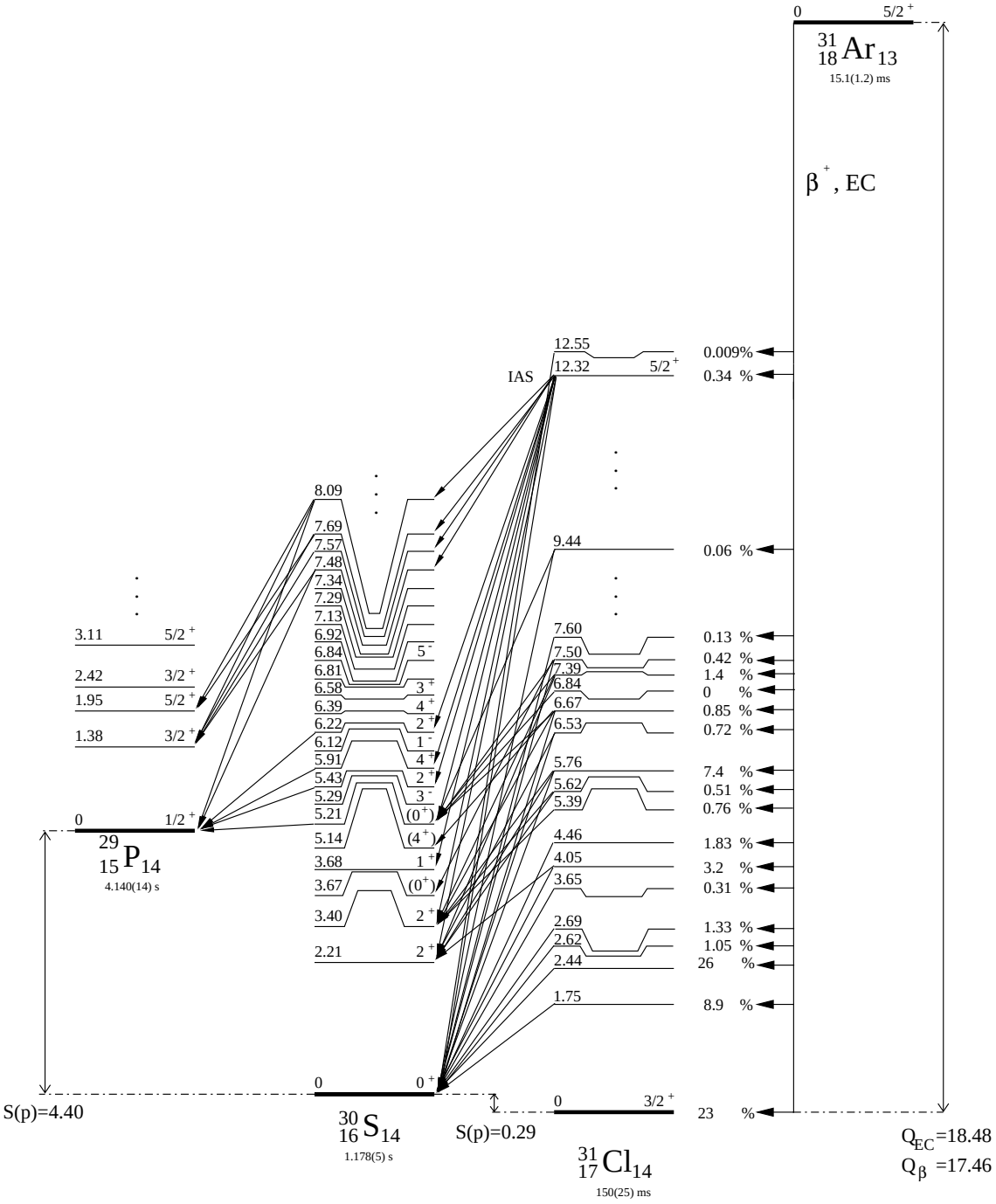

Figure 7.10: Decay scheme of ^{31}Ar. The shown transitions are only transitions which were seen in the single proton spectrum, i.e. the 42 peaks. The Branching ratios are only single proton branching ratios, the branching ratios for two-proton emission are given in [1]. All energy levels in ^{30}S are taken from Paddock [64] and Yokota *et al.* [65], except the two high energy levels at 7.693(4) MeV and 8.089(2) MeV.

7.4 The spin of the ground state of ^{31}Ar

The two most intensive peaks in the single proton spectrum are assigned to be transitions from respectively the second and third exited state in ^{31}Cl to the ground state in ^{30}S. Since these proton emissions are relatively strong, we can conclude that the β-decays feeding these states are allowed Gamow-Teller decays. From the comparison with the mirror nucleus we can conclude that the second excited state in ^{31}Cl is a $5/2^+$ state and the third excited state is a $3/2^+$ state, the ground state of ^{31}Ar is therefore forced to be either a $J^\pi = 3/2^+$ or $5/2^+$ state.

A fact that confirms the statement given above is that the mirror nucleus $^{31}_{13}\mathrm{Al}_{18}$ to $^{31}_{18}\mathrm{Ar}_{13}$ has a ground state with spin $J^\pi = 3/2^+$ or $5/2^+$, this is shown by Goosman and Alburger [68]. In this section, it will be shown that the ground state of ^{31}Ar is a $5/2^+$ state. This is made possible by using the unique method of observing the kinematic energy shift of the β-delayed protons. In chapter 5, this method was described and used on β-delayed protons from ^{32}Ar and ^{33}Ar, and it is now the time to use it on ^{31}Ar.

A spin of 5/2 for the IAS of the ground state of ^{31}Ar has previously been suggested in the paper [20]. This suggestion was based on an analysis of the angular correlation of the two emitted protons in β-delayed two-proton emission. However, a newer and more precise analysis of this angular correlation done by Fynbo shows no significant evidence for this suggestion [1].

In the following, we will investigate the decays of ^{31}Ar going through the second or third exited state of ^{31}Cl. Table 7.5 shows the different possible decay sequences

J^π sequences	L	Θ	τ	A
$\frac{3}{2}^+ \to \frac{3}{2}^+ \to 0^+$	2	1	8	$-\frac{13}{15}$
$\frac{3}{2}^+ \to \frac{5}{2}^+ \to 0^+$	2	$-\frac{7}{8}$	$\frac{64}{7}$	$\frac{1}{5}$
$\frac{5}{2}^+ \to \frac{3}{2}^+ \to 0^+$	2	$-\frac{1}{4}$	8	$-\frac{1}{5}$
$\frac{5}{2}^+ \to \frac{5}{2}^+ \to 0^+$	2	1	$\frac{64}{7}$	$-\frac{33}{35}$

Table 7.5: Parameters of the decay sequences. This table summarizes the possible decay sequences of ^{31}Ar going through the second or third exited state in ^{31}Cl and ending up in the ground state of ^{30}S. The first column shows the decay sequences, and the second column the angular momentum of the emitted proton; it is assumed that the lowest possible angular momentum is dominating. The parameters Θ, τ and the triple correlation coefficient A are displayed in the last three columns. The parameters are calculated as described in appendix C.

of these decays and the parameters Θ, τ and the triple correlation coefficient A.

In chapter 5 it was proved, that it is possible to deduce the triple correlation coefficient A by observing the kinematic energy shift of β-delayed protons. Moreover, the energy shift averaged over any direction of the neutrino and averaged over any kinetic energy of the β-particle is approximately a cosine. This cosine is a function of the angle between the proton and the β-particle. Let ε and t_{max} be defined by respectively equation 5.20 and equation 5.21 in section 5.2. By rewriting equation 5.22, we can deduce the following formula:

$$\frac{\varepsilon}{t_{max}} = \frac{3+2A}{12} \tag{7.4}$$

In the same way as in section 5.2, we compare the theory with measurements by plotting both sides of equation 7.4. This is done in figure 7.11.

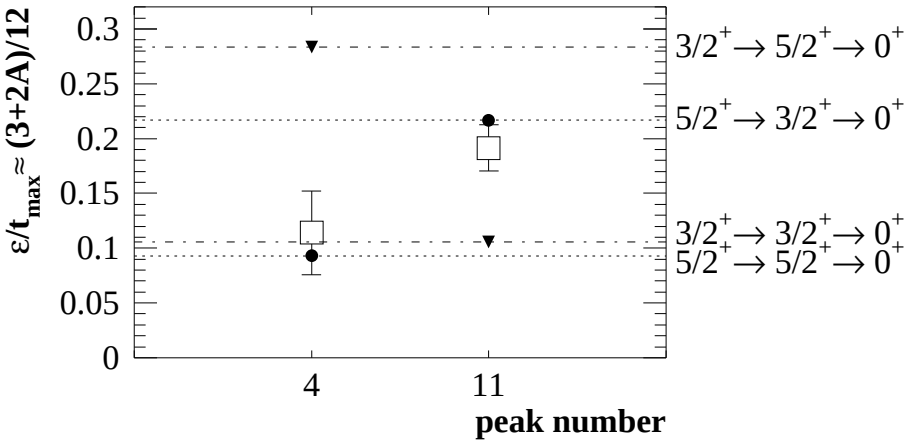

Figure 7.11: The spin of the ground state of ^{31}Ar. In this figure, the measured values of ε/t_{max} is compared with the theoretical values of $(3+2A)/12$ for the peaks 4 and 11. The four lines represent the different kinds of decay sequences shown to the right. The triangles display the expected values of a spin 3/2 ground state of ^{31}Ar, and the black dots show the expected values of a spin 5/2 ground state of ^{31}Ar.

In figure 7.11, it is clearly seen that the spin and parity of the ground state of ^{31}Ar is in accordance with a value of $5/2^+$. Remembering that the simple model used in this analysis only has a precision of about $m_\beta/T_{\beta,max}$, which in these two cases is of the order of 0.033-0.034, we can conclude that there is a significant difference between the two proposed values. Thus, the spin and parity of the ground state is $5/2^+$.

Add to this that shell-model calculations also indicate a spin $5/2^+$ for the ground state of ^{31}Ar [21, 69]. On this basis, it is doubtful that this result will prove to be wrong.

7.4.1 Spin assignments of energy levels in ^{31}Cl

By using the just established result of a spin and parity of $5/2^+$ for the ground state of ^{31}Ar, we can conclude that the IAS also has a spin of $5/2^+$. Moreover, it is possible to investigate the spin and parity of other states in ^{31}Cl. First of all, we only expect to observe allowed β-decays. Thus, the populated levels in ^{31}Cl are forced to have spin equal to $3/2^+$, $5/2^+$ or $7/2^+$. Secondly, only intensive proton peaks, which correspond to proton decays to the three lowest states in ^{30}S can be used. These states have either spin(parity) 0^+ or 2^+. The possible decay sequences are therefore as shown in table 7.6.

J^π sequences	L	Θ	τ	A
$\frac{5}{2}^+ \to \frac{3}{2}^+ \to 0^+$	2	$-\frac{1}{4}$	8	$-\frac{1}{5}$
$\frac{5}{2}^+ \to \frac{5}{2}^+ \to 0^+$	2	1	$\frac{64}{7}$	$-\frac{33}{35}$
$\frac{5}{2}^+ \to \frac{7}{2}^+ \to 0^+$	4	$-\frac{3}{4}$	$\frac{200}{21}$	$\frac{1}{7}$
$\frac{5}{2}^+ \to \frac{3}{2}^+ \to 2^+$	0	$-\frac{1}{4}$	0	$-\frac{1}{3}$
$\frac{5}{2}^+ \to \frac{5}{2}^+ \to 2^+$	0	1	0	$-\frac{1}{3}$
$\frac{5}{2}^+ \to \frac{7}{2}^+ \to 2^+ \left(\frac{3}{2}\right)$	2	$-\frac{3}{4}$	$\frac{400}{49}$	$\frac{11}{147}$
$\frac{5}{2}^+ \to \frac{7}{2}^+ \to 2^+ \left(\frac{5}{2}\right)$	2	$-\frac{3}{4}$	$\frac{200}{147}$	$-\frac{39}{147}$

Table 7.6: Possibly observable decay sequences of ^{31}Ar. In the first column, the decay sequence is shown. In the special case of a $5/2^+ \to 7/2^+ \to 2^+$ decay, it is a bit more complicated. This is due to the fact that there are two different possibilities of the total spin of the final nuclear state and the proton. The vector sum of the spin of the final nuclear state and the proton is shown in brackets. In the second column, the angular momentum of the emitted proton is shown; lowest order angular momentum is expected to be dominating. In the next three columns, the parameters Θ, τ and A are displayed.

In the cases where the final nucleus is a 2^+ state, there is no difference in the triple correlation coefficient A between a β-daughter nucleus with spin $3/2^+$ and $5/2^+$. Moreover, in the decay sequence: $5/2^+ \to 7/2^+ \to 2^+$ (5/2), the parameter $A = -39/147$. This value is inseparable from the value $-1/3$ in our experiment. Extremely precise measurements are needed to separate these two values.

It is therefore impossible to use this method to distinguish between decays with a β-daughter nucleus of spin $3/2^+$, $5/2^+$ or $7/2^+$, in cases with a final state with a spin equal to 2^+.

This is why we only investigate decays ending up in the ground state of ^{30}S. The result of this investigation of the five most clear peaks is shown in figure 7.12.

In the figure, one can see that all the data points lie a bit lower than the

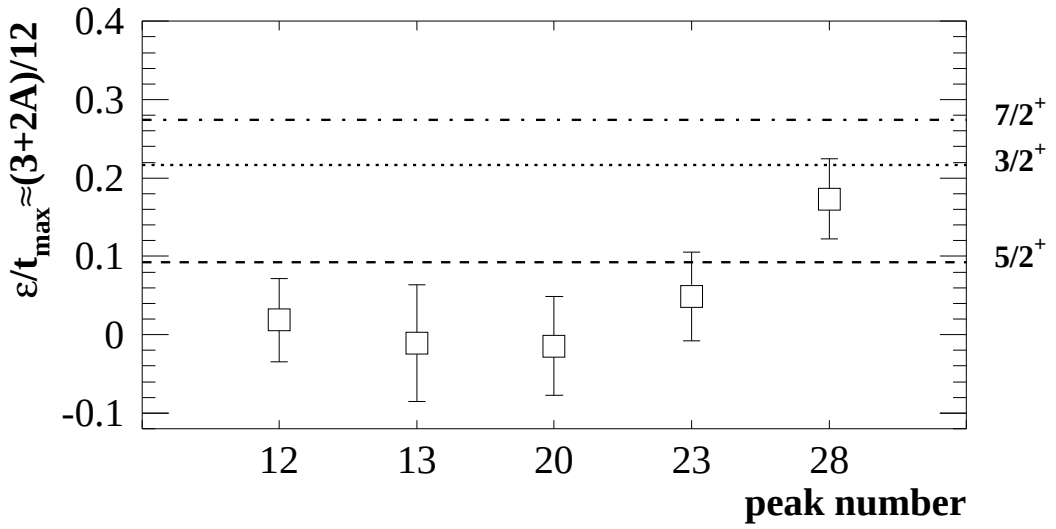

Figure 7.12: Spin assignments of energy levels in ^{31}Cl. This figure illustrates a comparison of ε/t_{max} with $(3+2A)/12$ for 5 different proton energies. All the studied decay sequences ends up in the ground state of ^{30}S. The open squares represent the values of ε/t_{max}. The 3 lines represent the values expected for decays respectively going through a $3/2^+$, $5/2^+$ or $7/2^+$ state in ^{31}Cl.

theoretic values. The systematic error of the approximations made to derive the theoretic formula is on the order of $m_\beta/T_{\beta,max}$, which in these five cases amounts to 0.034-0.044. From this, we can conclude that the four energy levels 2.62 MeV, 2.70 MeV, 4.05 MeV and 4.46 MeV belonging respectively to the peaks 12, 13, 20 and 23, are levels with spin and parity $5/2^+$. The last peak is connected to the energy level 5.75 MeV which most probably is a spin $3/2^+$ state, as a consequence of figure 7.12.

These spin assignments depend strongly on the energy assignments. If an energy assignment proves to be wrong, the matching spin assignment based on this method cease to be valid. Moreover, this analysis is very sensitive to underlying peaks. For instance, for the peaks 20 and 13 the deduced parameters ε are negative, which we think maybe is caused be partly underlying smaller peaks.

Chapter 8

Summary and perspectives

In the following, a short summary is given. The field of exotic nuclei, especially the proton rich side of the drip line, was introduced in chapter 2.

In chapter 3, the detector system was described and in chapter 4, it was analyzed. Naturally, we also had to calibrate the detectors, which was equally described in chapter 4. The strip detector, which is the key detector of the detector system was studied in greater details. For instance, in chapter 4 a simple method of comparison of the signal in the front and back strip was used to deduce a resolution of the strip detector to 17.2(14) keV (FWHM). Moreover, the interstrip effects; charge charging and charge losses were described, and at the end of the chapter, the strip-ESI telescope was used in the correction of high energy protons.

In chapter 5, we went on to study the kinematic shift in β-delayed proton emission. The first part of this chapter was theoretical, ending up with a simple formula describing the relation between the kinetic energy shift of the proton and the triple correlation coefficient (A). This formula was used in a comparison of the spin, isospin and energy of the three most intensive peaks in the proton spectrum of ^{32}Ar and ^{33}Ar with the predictions of the simple model. The result clearly showed that this method can be used to distinguish between allowed Fermi and Gamow-Teller decays.

In chapter 6, the half-lives of the three argon isotopes ^{31}Ar, ^{32}Ar and ^{33}Ar were measured to be respectively 17.0(17) ms, 104(2) ms and 170(6) ms, which is in agreement with previous measurements.

Thereafter, in chapter 7, the β-delayed single proton emission of ^{31}Ar was studied. Here, some examples of β-delayed two-proton emission were given because one cannot deduce the single proton spectrum without first understanding the two-proton spectrum. In that chapter, a decay scheme of the β-delayed single proton

emission of ^{31}Ar was constructed, including branching ratios. For this both, p-p coincidences and p-γ coincidences were used, and a comparison of energy levels in ^{31}Ar with the mirror nucleus was made.

Furthermore, by using the method of observing the β-ν recoil shift of β-delayed proton emission, it was shown in chapter 7 that the ground state of ^{31}Ar, and hence the IAS, is a spin $5/2^+$ state. This result was thereafter used to deduce the spin and parity of five other energy levels in ^{31}Cl.

In this thesis, it has been shown how the method of observing the kinematic energy shift of β-delayed protons can be used in spin and isospin assignments. This method is a simple qualitative method, based on a simple approximation.

We therefore propose a new method where one includes special designed β-detectors, for instance Si-detectors or plastic scintillators, maybe even a telescope detector containing a plastic scintillator mounted behind a doubled-sided Si-strip detector.

The only demands are: Reasonable separation possibilities of protons, β-particles and γ-rays, a uniformity of response to E_β, and a nearly 100 % efficiency in detecting β-particles. With such detectors it will be possible to perform the exact average over the β-spectrum and we thus have a method like the one shown in this thesis, except that this one can also be used in quantitative determination of the β-ν-p angular correlation, and thereby maybe we can gain new information about the interaction involved in the β-decay.

Previously, the investigations of the kinetic energy shift of β-delayed protons have been used in experimental verifications of the V-A form of the charged weak current. According to the Standard Model, nuclear weak processes are well described in terms of only the vector (V) and the axial-vector (A) interactions. However, there is still a small possibility of scalar (S) and tensor (T) type interactions.

At the present, the experimental upper limit (95% confidence level) for the T-interaction is at 9% [70], while it is 17% for the S-interaction [71]. This last result for the S-interaction is extracted from the measurements of Schardt and Riisager [34]. However, the limit is maybe worse than quoted, see comments in Egorov *et al.* [28]. The above comment shows that the research in the field of β-delayed particle emission is a good probe for the study of the character of the interaction involved in β-decay, and the proposed method will very possibly be used for this kind of investigation in the future.

Appendix A

Calibration tables

	Part1					
	Front strip		Back strip		Finish	
	b	a	b	a	b	a
1	−65.10(326)	2.9116(35)	−45.81(324)	5.3889(65)	−17.86(320)	2.4586(30)
2	−21.21(321)	2.8698(35)	−112.49(331)	5.4477(66)	−3.60(319)	2.5079(30)
3	−11.12(320)	2.9463(36)	−78.22(327)	5.5007(67)	−4.30(319)	2.3898(29)
4	−21.55(321)	2.8886(35)	34.90(314)	5.3766(65)	0	0
5	−20.51(321)	2.8052(34)	−101.66(330)	5.3541(65)	−45.64(324)	2.3984(29)
6	−25.97(321)	2.7711(34)	−114.76(332)	5.3588(65)	−59.82(325)	2.5024(30)
7	−8.64(319)	2.9529(36)	−39.47(323)	5.4432(66)	−59.91(325)	2.5375(31)
8	−36.93(323)	2.8463(34)	−126.36(333)	5.5219(67)	−31.20(322)	2.4447(30)
9	.96(318)	2.9887(36)	−48.59(324)	5.5213(67)	17.34(316)	2.2809(28)
10	−18.95(321)	3.2434(39)	−58.76(325)	5.2095(63)	21.72(316)	2.4967(30)
11	25.80(315)	3.1112(38)	−101.12(330)	5.1645(62)	−8.27(319)	2.4583(30)
12	−15.54(320)	2.8952(35)	−86.10(328)	5.4372(66)	−3.58(319)	2.5083(30)
13	17.50(316)	2.8378(34)	−5.43(319)	5.4000(65)	0	0
14	−13.00(320)	2.8514(34)	1.93(318)	5.3891(65)	−5.29(319)	2.4906(30)
15	11.98(317)	2.9031(35)	−66.32(326)	5.3051(64)	10.76(317)	2.4620(30)
16	−41.23(323)	2.9811(36)	−38.41(323)	5.3663(65)		

Table A.1: Energy calibration: $E_p = a \cdot Ch + b$

	Part2					
	Front strip		Back strip		Finish	
	b	a	b	a	b	a
1	−163.41(337)	5.6065(68)	−40.62(323)	5.3886(65)	−10.17(320)	2.4544(30)
2	−88.61(329)	5.5414(67)	−97.91(330)	5.4330(66)	−7.83(319)	2.5126(30)
3	−67.23(326)	5.6832(69)	−65.80(326)	5.5021(67)	−8.53(319)	2.3902(29)
4	−80.63(328)	5.5805(68)	29.97(315)	5.3884(65)	0	0
5	−81.06(328)	5.4295(66)	−88.50(329)	5.3409(65)	−50.06(324)	2.4012(29)
6	−111.03(331)	5.3706(65)	−110.82(331)	5.3625(65)	−56.67(325)	2.5004(30)
7	−52.57(325)	5.6956(69)	−32.55(322)	5.4384(66)	−51.55(324)	2.5299(31)
8	−105.48(331)	5.4910(66)	−120.19(332)	5.5143(67)	−20.51(321)	2.4453(30)
9	−41.21(323)	5.7750(70)	−42.12(323)	5.5174(67)	2.44(318)	2.2901(28)
10	−78.83(328)	6.0355(73)	−57.78(325)	5.2186(63)	24.89(316)	2.4962(30)
11	23.16(316)	5.9942(73)	−101.07(330)	5.1714(63)	−7.40(319)	2.4562(30)
12	−81.87(328)	5.5888(68)	−86.40(328)	5.4477(66)	1.34(318)	2.5013(30)
13	−17.54(320)	5.4888(66)	−2.30(319)	5.4057(65)	0	0
14	−103.71(330)	5.5323(67)	20.22(316)	5.3753(65)	−9.08(319)	2.4946(30)
15	−45.01(324)	5.6267(68)	−69.24(326)	5.3214(64)	6.83(318)	2.4651(30)
16	−137.68(334)	5.7620(70)	−29.05(322)	5.3572(65)		

Table A.2: Energy calibration: $E_p = a \cdot Ch + b$

	Part3					
	Front strip		Back strip		Finish	
	b	a	b	a	b	a
1	−168.21(338)	5.6150(68)	−33.14(322)	5.3775(65)	−11.73(320)	2.4596(30)
2	−88.33(329)	5.5421(67)	−96.81(330)	5.4326(66)	−8.52(319)	2.5127(30)
3	−66.86(326)	5.6832(69)	−63.80(326)	5.5029(67)	−.92(319)	2.3845(29)
4	−84.02(328)	5.5866(68)	27.01(315)	5.3887(65)	0	0
5	−83.95(328)	5.4335(66)	−91.41(329)	5.3475(65)	−49.62(324)	2.4011(29)
6	−108.90(331)	5.3654(65)	−110.26(331)	5.3639(65)	−56.68(325)	2.5022(30)
7	−57.21(325)	5.7041(69)	−29.65(322)	5.4347(66)	−51.49(324)	2.5298(31)
8	−103.46(330)	5.4874(66)	−115.24(332)	5.5025(67)	−23.31(321)	2.4489(30)
9	−40.77(323)	5.7746(70)	−40.00(323)	5.5151(67)	5.06(318)	2.2899(28)
10	−81.61(328)	6.0411(73)	−57.50(325)	5.2205(63)	24.03(316)	2.4969(30)
11	24.26(316)	5.9932(73)	−100.71(330)	5.1725(63)	−7.85(319)	2.4574(30)
12	−78.73(328)	5.5838(68)	−78.17(327)	5.4359(66)	4.64(318)	2.4995(30)
13	−15.06(320)	5.4834(66)	−2.84(319)	5.4065(65)	0	0
14	−104.11(331)	5.5325(67)	19.86(316)	5.3813(65)	−13.03(320)	2.4988(30)
15	−51.95(324)	5.6399(68)	−61.50(326)	5.3127(64)	3.96(318)	2.4685(30)
16	−141.95(335)	5.7699(70)	−29.65(322)	5.3604(65)		

Table A.3: Energy calibration: $E_p = a \cdot Ch + b$

Appendix B

Figures of checks and cuts

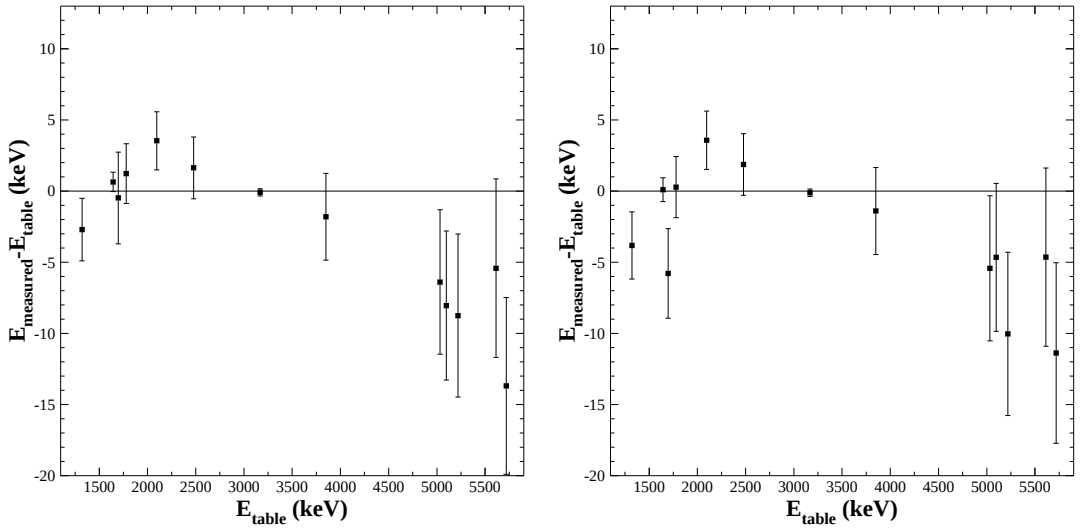

(a) front-strip, part 1

(b) back-strip, part 1

Figure B.1: Checks of the energy calibrations

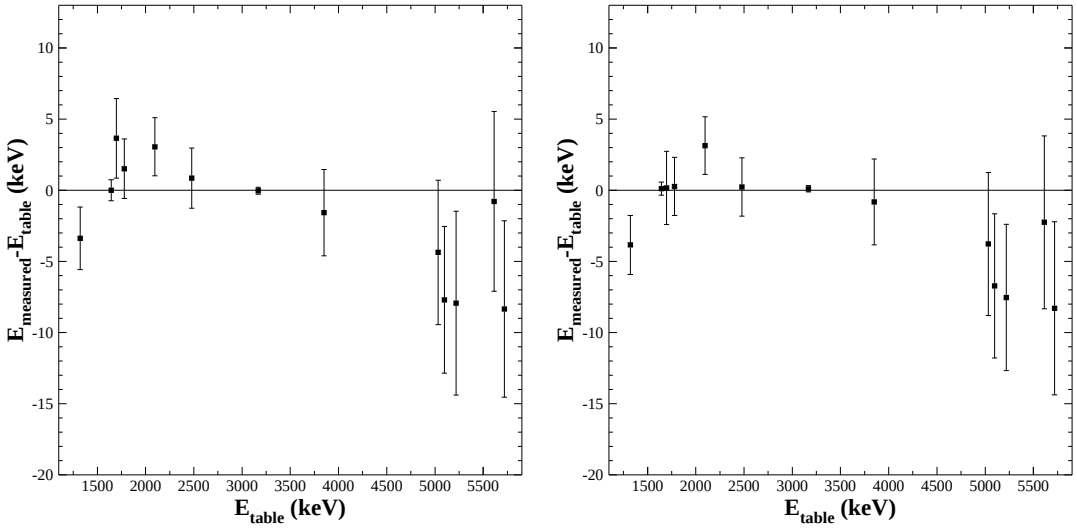

(a) FUTIS, part 1

(b) FUTIS, part 2

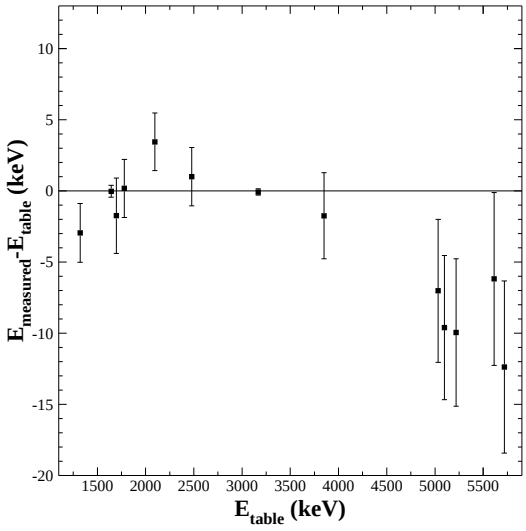

(c) front-strip, part 2

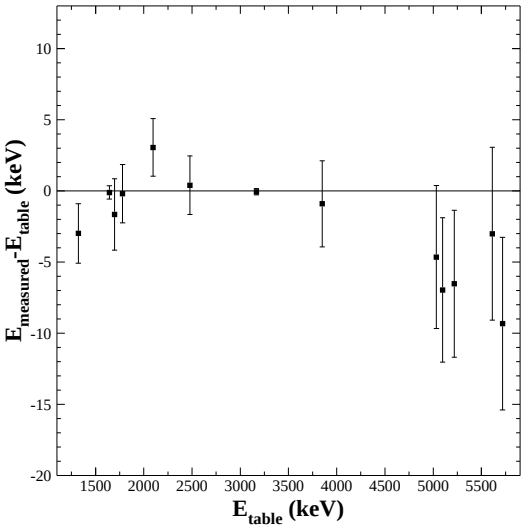

(d) back-strip, part 2

Figure B.2: Checks of the energy calibrations

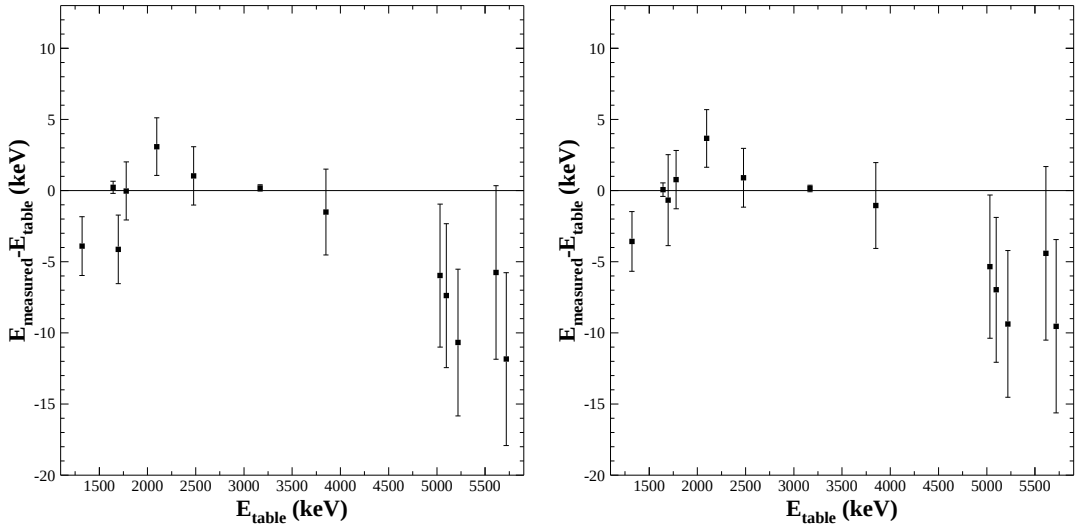

(a) front-strip, part 3

(b) back-strip, part 3

Figure B.3: Checks of the energy calibrations

Figure B.4: Different cuts of protons from the IAS of ^{33}Ar

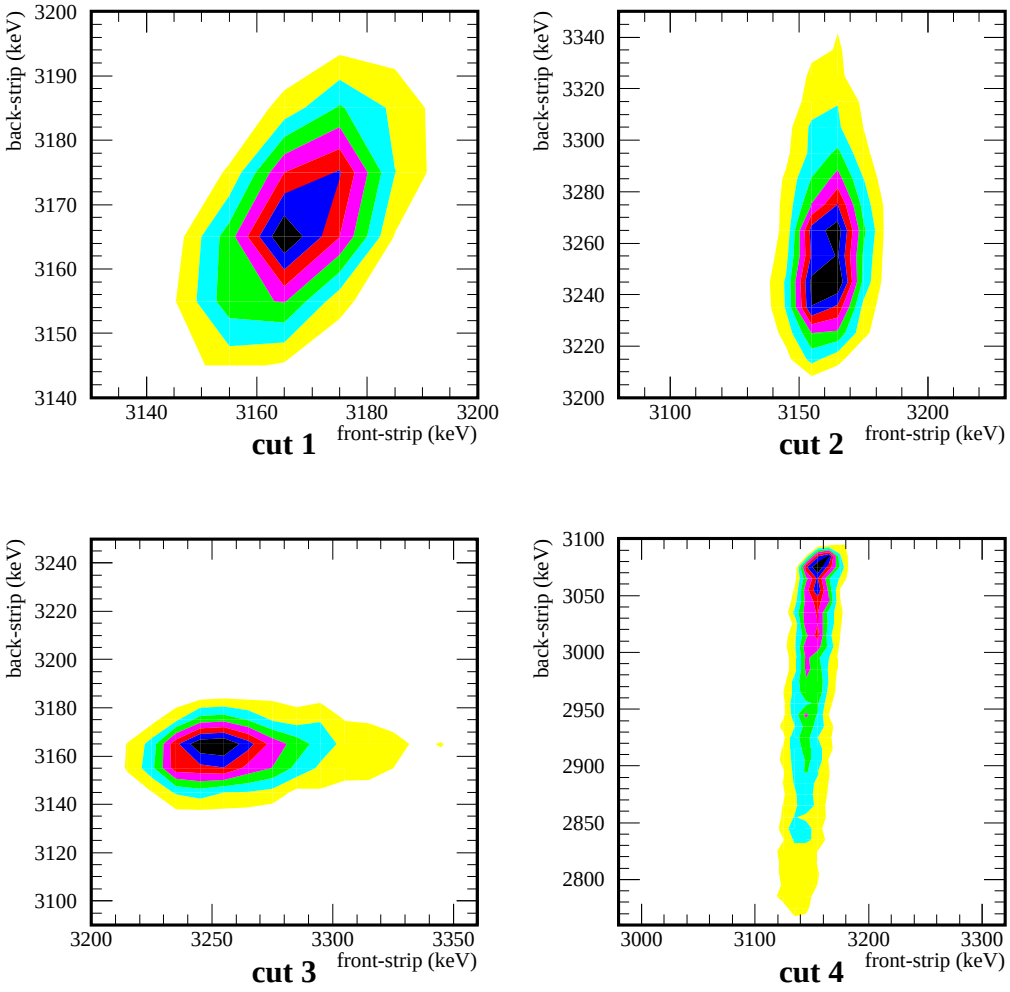

Figure B.5: Different cuts of protons from the IAS of ^{33}Ar

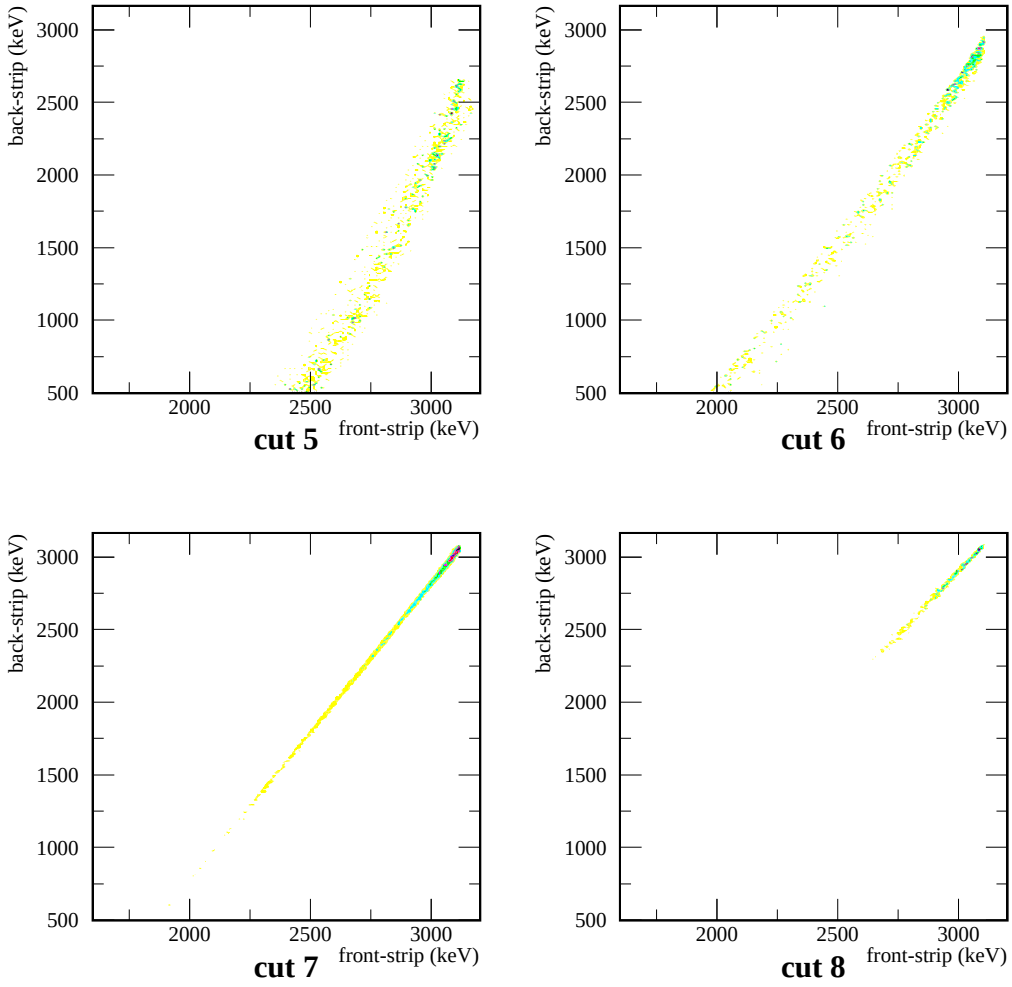

Appendix C

Spin sequence parameters

The triple correlation coefficient A is given by

$$A = \frac{g_V^2 B_F - (\frac{1}{3} + \frac{2}{30}\tau\Theta) g_A^2 B_{GT}}{g_V^2 B_F + g_A^2 B_{GT}} \tag{C.1}$$

A complete analysis of the triple correlation coefficient A is given by Holstein [56]. The two spin-dependent coefficients τ and Θ are reproduced here, in a manner like the one used by Schardt and Riisager [34]. The coefficient Θ depends on the nuclear spin of the parent and the daughter nucleus. Let J be the nuclear spin of the parent nucleus and J' that of the daughter nucleus, then:

$$\Theta = \begin{cases} -\dfrac{J'+1}{2J'-1} & \text{for} \quad J' = J+1 \\ 1 & \text{for} \quad J' = J \\ -\dfrac{J'}{2J'+3} & \text{for} \quad J' = J-1 \end{cases} \tag{C.2}$$

The coefficient τ depends on the angular momentum involved in the proton emission. Let L be the orbital angular momentum of the emitted proton, J' the spin of the β-daughter nucleus and J'' the vector sum of the spin of the final nuclear state and the spin of the proton ($S = 1/2$):

$$\tau = 10\sqrt{\frac{L(L+1)(2L+1)}{(2L-1)(2L+3)}}\sqrt{\frac{(2J'-1)(2J'+1)(2J'+3)}{J'(J'+1)}} W(2J'LJ''; J'L) \tag{C.3}$$

where W is a Racah coefficient. Sometimes it can be helpful to rewrite the Racah coefficients in more symmetrical coefficients, the so-called $6J$ symbols:

$$W(J_1 J_2 L_2 L_1; J_3 L_3) = (-1)^{-J_1-J_2-L_1-L_2} \begin{Bmatrix} J_1 & J_2 & J_3 \\ L_1 & L_2 & L_3 \end{Bmatrix} \tag{C.4}$$

Notice that τ is zero for s-wave protons.

Appendix D

Fitting procedure for Poisson statistics

In this appendix, we will take a closer look at the statistics of Poisson distributed Random variables.

Let us first consider a one-dimensional histogram having n bins labelled by the index i running from 1 to n. Let X_i be the random variables representing each of the n bins and let x_i be the measured counts in the i'th bin. In the case where each of the random variables X_1,X_2, ... ,X_k are independent and normally distributed ($X_i \sim N(\mu_i, \sigma_i)$)*, we get the commonly used result of least-squares fitting:

$$\chi^2 = \sum_{i=1}^{n} \left(\frac{x_i - \mu_i}{\sigma_i} \right)^2 \tag{D.1}$$

However, in physics one more often uses counting statistics where the random variables X_i are Poisson distributed. In these cases, one often see Neyman's χ^2 or Pearson's χ^2 being used. By using an ad hoc argument we can derive these functions. If the random variable X is Poisson distributed ($X \sim po(\lambda)$), the mean value is equal to λ and the variance σ^2 is equal to λ. Thus, if we put σ_i^2 equal to x_i in equation D.1 we get Neyman's χ^2:

$$\chi^2 = \sum_{i=1}^{n} \frac{(x_i - \mu_i)^2}{x_i} \tag{D.2}$$

and if we put σ_i^2 equal to μ_i in equation D.1 we get Pearson's χ^2:

$$\chi^2 = \sum_{i=1}^{n} \frac{(x_i - \mu_i)^2}{\mu_i} \tag{D.3}$$

*the normal distribution is also called the Gaussian distribution.

Both results are only approximations giving estimates of parameters and errors which go asymptotically to the true value for a infinite sample size ($\mu_i \to \infty$). For small sample sizes one has to be very careful. Instead of using Neyman's or Pearson's χ^2-functions, one can use an approximation shown in Baker and Cousins [63].

In the case where each of the random variables X_1,X_2, ... ,X_k are independent and Poisson distributed ($X_i \sim po(\mu_i)$), one can deduce the likelihood ratio and construct a function that asymptotically obeys a χ^2-distribution. This it done by using the likelihood ratio test theorem. This Poisson likelihood χ^2-function is given by [63]:

$$\chi^2 = 2\sum_{i=1}^{n}\left(\mu_i - x_i + x_i \ln\left(\frac{x_i}{\mu_i}\right)\right) \tag{D.4}$$

Hereby we can fit curves by the usual method of minimization of the χ^2-function and moreover use the common methods to deduce parameters and errors for χ^2-statistics.

In Jading and Riisager [72], you can find a comparison of the different methods of fitting Poisson distributed data. They use n independent random variables X_1,X_2, ... ,X_n which all have identical Poisson distributions ($X_i \sim po(\mu)$). They found out that in the limit $n \to \infty$, the expectation value obtained with Neyman's χ^2 is: $\mu_N \simeq \mu - 1$, and with Pearson's χ^2: $\mu_P \simeq \mu + 1/2$. We can therefore conclude that especially when the number of counts in each bin is small, the discrepancy of the expectation values of Neyman's χ^2 and Pearson's χ^2 are too large. It should therefore be avoided to use these methods for the determination of parameter values when the sample sizes are small.

In using equation D.4, one has to be careful because the logarithm is only properly defined as a function of a positive parameter. Since physical quantities normally can be chosen to be positive, this means one has to provide that:

$$\forall i = 1, 2, \ldots, n : \mu_i > 0 \tag{D.5}$$

For further reading about statistics, I can recommend "Statistical Methods In Experimental Physics" by Eadie *et al.* [73].

Appendix E

Selection rules for proton, β and γ decays

This appendix contains a summary of the selection rules for different kinds of decays. In all formulas vectors are represented boldfaced.

The total angular momentum of an object $\boldsymbol{J}$ is given by: $\boldsymbol{J} = \boldsymbol{L} + \boldsymbol{S}$, where $\boldsymbol{L}$ is the orbital angular momentum and $\boldsymbol{S}$ is the spin angular momentum. The parity of a state is called π. Each of these parameters can have different subscripts: I for initial nucleus, F for final nucleus, p for proton, β for beta particle, ν for neutrino and γ for gamma particle.

Classification of proton emission

$$\boldsymbol{J}_I = \boldsymbol{J}_F + \boldsymbol{L}_p + \boldsymbol{S}_p \qquad \wedge \qquad S_p = 1/2 \qquad \wedge \qquad \pi_I = \pi_F(-1)^{L_p} \tag{E.1}$$

The protons are tunneling through the Coulomb barrier. Protons with high orbital angular momentum L_p also have to penetrate the centrifugal barrier, therefore lowest orders of orbital angular momentum L_p are emitted with a higher probability.

Classification of allowed β decay

In allowed transitions $L_{\beta\nu} = 0$, in first forbidden transitions $L_{\beta\nu} = 1$ and in second forbidden transitions $L_{\beta\nu} = 2$ etc. Beside that, the decays are separated in Fermi decays: $S_{\beta\nu} = 0$ and Gamow-Teller decays: $S_{\beta\nu} = 1$. Moreover, we have that:

$$\boldsymbol{J}_I = \boldsymbol{J}_F + \boldsymbol{L}_{\beta\nu} + \boldsymbol{S}_{\beta\nu} \qquad \wedge \qquad \pi_I = \pi_F(-1)^{L_\beta} \tag{E.2}$$

Only the selection rules for allowed transitions will here be given in details.

Allowed transitions ($L_{\beta\nu} = 0$, $\pi_I = \pi_F$)

Fermi decay ($S_{\beta\nu} = 0$)	Gamow-Teller decay ($S_{\beta\nu} = 1$)
$\boldsymbol{J}_I = \boldsymbol{J}_F$	$\boldsymbol{J}_I = \boldsymbol{J}_F + \boldsymbol{1}$
$\lvert\Delta J\rvert = 0$	$\lvert\Delta J\rvert = 0, 1$: no $0^+ \to 0^+$
$0^+ \to 0^+$: superallowed	$0^+ \to 1^+$: unique Gamow-Teller

Classification of γ decay

In γ decay, one uses the special symbols of classical multipole radiation. Let l be the index of the radiation, then the order of multipole radiation will be 2^l and the transfered angular momentum will be l per photon. There are two types of multipoles; the electric and the magnetic. They are represented by respectively the letter E or M followed by the index number l, for example E1 represents electric dipole radiation and M2 represents magnetic quadrupole radiation.

$$\boldsymbol{J}_I = \boldsymbol{J}_F + \boldsymbol{l} \qquad \wedge \qquad \pi(El) = (-1)^l \qquad \wedge \qquad \pi(Ml) = (-1)^{l+1} \tag{E.3}$$

The selection rules are written in a more detailed fashion below.

$\lvert J_I - J_F\rvert \leq l \leq J_I + J_F$	(no $l = 0$)
$\Delta\pi$ =no:	even electric, odd magnetic
$\Delta\pi$ =yes:	odd electric, even magnetic

References

[1] L. Axelsson, J. Äystö, U. C. Bergmann, M. J. G. Borge, L. M. Fraile, H. O. U. Fynbo, A. Honkanen, P. Hornshøj, Y. Jading, A. Jokinen, B. Jonson, I. Martel, I. Mukha, T. Nilsson, G. Nyman, M. Oinonen, K. Riisager, T. Siiskonen, M. H. Smedberg, O. Tengblad, J. Thaysen and F. Wenander: *"β-Delayed Particle Emission in the Decay of ^{31}Ar: The Mechanism of the Two-Proton Emission Resolved"*. in preparation.

[2] J. Thaysen, L. Axelsson, J. Äystö, M. J. G. Borge, L. M. Fraile, H. O. U. Fynbo, A. Honkanen, P. Hornshøj, Y. Jading, A. Jokinen, B. Jonson, I. Martel, I. Mukha, T. Nilsson, G. Nyman, M. Oinonen, K. Riisager, T. Siiskonen, M. H. Smedberg, O. Tengblad and F. Wenander: *"Determination of the Spin of ^{31}Ar"*. in preparation.

[3] K. Riisager: *"Nuclear Halo States"*. Rev. Mod. Phys. **66**, 1105 (1994).

[4] P. G. Hansen, A. S. Jensen and B. Jonson: *"Nuclear Halos"*. Ann. Rev. Nucl. Sci. **45**, 591 (1995).

[5] I. Tanihata: *"Neutron Halo Nuclei"*. J. Phys. G **22**, 157 (1996).

[6] V. I. Gol'danskii: *"On Neutron-Deficient Isotopes of Light Nuclei and The Phenomena of Proton and Two-Proton Radioactivity"*. Nucl. Phys. **19**, 482 (1960).

[7] G. Audi and A. H. Wapstra: *"The 1993 Atomic Mass Evaluation (II) Nuclear-reaction and Separation Energies"*. Nucl. Phys. A **565**, 66 (1993).

[8] R. A. Kryger, A. Azhari, M. Hellström, J. H. Kelley, T. Kubo, R. Pfaff, E. Ramakrishnan, B. M. Sherrill, M. Thoennessen, S. Yokoyama, R. J Charity, J. Dempsey, A. Kirov, N. Robertson, D. G. Sarantites, L. G. Sobotka and J. A. Winger: *"Two-Proton Emission from the Ground State of ^{12}O"*. Phys. Rev. Lett. **74**, 860 (1995).

[9] A. Azhari, R. A. Kryger and M. Thoennessen: *"Decay of the ^{12}O ground state"*. Phys. Rev. C **58**, 2568 (1998).

[10] O. V. Bocharev, A. A. Korsheninnikov, E. A. Kuz'min, I. G. Mukha, L. V. Chulkov and G. B. Yan'kov: *"Experimental Study of Three-particle Decays of $^6Be(0^+)$ and $^6Be^*(2^+)$"*. Sov. J. Nucl. Phys. **55**, 955 (1992).

[11] V. I. Gol'danskii: *"Neutron-Excessive Nuclei and Two-Proton Radioactivity"*. Phys. Lett. B **212**, 11 (1988).

[12] B. J. Cole: *"Proton and Two-Proton Drip Lines in the sd Shell"*. Phys. Rev. C **58**, 2831 (1998).

[13] R. E. Azuma, L. C. Carrez, P. G. Hansen, B. Jonson, K.-L. Kratz, S. Mattsson, G. Nyman, H. Ohm, H. L. Ravn, A. Schröder and W. Ziegert: *"First Observation of Beta-Delayed Two-Neutron Radioactivity: ^{11}Li"*. Phys. Rev. Lett. **43**, 1652 (1979).

[14] V. I. Gol'danskii: *"Emission of β^+-Delayed Pairs of Protons and Doubly β^+-Delayed Protons and α particles"*. JETP Lett. **32**, 554 (1980).

[15] V. Borrel, J. C. Jacmart , F. Pougheon, A. Richard, R. Anne, D. Bazin, H. Delagrange, C. Détraz, D. Guillemaud-Mueller, A. C. Mueller, E. Roeckl, M. G. Saint-Laurent, J. P. Dufour, F. Hubert and M. S. Pravikoff: *"Beta-Delayed Proton Decay of the $T_z = -\frac{5}{2}$ Isotope ^{31}Ar"*. Nucl. Phys. A **473**, 331 (1987).

[16] J. E. Reiff, M. A. C. Hotchkis, D. M. Moltz, T. F. Lang, J. D. Robertson and J. Cerny: *"A Fast In-Beam Recoil Catcher Wheel and the Observation of Beta-Delayed Two-Protron Emission from ^{31}Ar"*. Nucl. Instr. Meth. A **276**, 228 (1989).

[17] V. Borrel, J. C. Jacmart , F. Pougheon, R. Anne, C. Détraz, D. Guillemaud-Mueller, A. C. Mueller, D. Bazin, R. Del Moral, J. P. Dufour, F. Hubert, M. S. Pravikoff and E. Roeckl: *"^{31}Ar and ^{27}S Beta-Delayed Two-Proton Emission and Mass Excess"*. Nucl. Phys. A **531**, 353 (1991).

[18] M. J. G. Borge, H. Gabelmann, L. Johannsen, B. Jonson, G. Nyman, K. Riisager and O. Tengblad: *"The Decay of ^{31}Ar"*. Nucl. Phys. A **515**, 21 (1990).

[19] D. Bazin, R. Del Moral, J. P. Dufour, A. Fleury, F. Hubert, M. S. Pravikoff, R. Anne, P. Bricault, C. Détraz, M. Lewitowicz, Y. Zheng, D. Guillemaud-Mueller, J. C. Jacmart , A. C. Mueller, F. Pougheon and A. Richard: *"Decay Modes of ^{31}Ar and First Observation of β-Delayed Three-Proton Radioactivity"*. Phys. Rev. C **45**, 69 (1992).

[20] L. Axelsson, J. Äystö, U. C. Bergmann, M. J. G. Borge, L. M. Fraile, H. O. U. Fynbo, A. Honkanen, P. Hornshøj, A. Jokinen, B. Jonson, I. Martel, I. Mukha, T. Nilsson, G. Nyman, B. Petersen, K. Riisager, M. H. Smedberg and O. Tengblad: *"Two-Proton Emission in the Decay of ^{31}Ar"*. Nucl. Phys. A **628**, 345 (1998).

[21] L. Axelsson, J. Äystö, M. J. G. Borge, L. M. Fraile, H. O. U. Fynbo, A. Honkanen, P. Hornshøj, A. Jokinen, B. Jonson, P. O. Lipas, I. Martel, I. Mukha, T. Nilsson, G. Nyman, B. Petersen, K. Riisager, M. H. Smedberg and O. Tengblad: *"Beta Decay of ^{31}Ar"*. Nucl. Phys. A **634**, 475 (1998), Erratum ibib Nucl. Phys. A **641**, 529 (1998).

[22] M. D. Cable, J. Honkanen, R. F. Parry, S. H. Zhou, Z. Y. Zhou and J. Cerny: *"Discovery of Beta-Delayed Two-Proton Radioactivity: ^{22}Al"*. Phys. Rev. Lett. **50**, 404 (1983).

[23] B. Blank, F. Boué, S. Andriamonje, S. Czajkowski, R. Del Moral, J. P. Dufour, A. Fleury, P. Pourre, M. S. Pravikoff, E. Hanelt, N. A. Orr and K.-H. Schmidt: *"Spectroscopic Studies of the βp and $\beta 2p$ Decay of ^{23}Si"*. Zeit. Phys. A **357**, 247 (1997).

[24] I. Mukha, L. Axelsson, J. Äystö, U. C. Bergmann, M. J. G. Borge, L. M. Fraile, H. O. U. Fynbo, A. Honkanen, P. Hornshøj, Y. Jading, B. Jonson, A. Jokinen, I. Martel, M. Oinonen, T. Nilsson, G. Nyman, B. Petersen, K. Riisager, T. Siiskonen, M. H. Smedberg, O. Tengblad and F. Wenander: *"Two-Proton Decay of the Isobaric Analogue State of ^{31}Ar"*. Nucl. Phys. A **630**, 394c (1998).

[25] C. H. Johnson, F. Pleasonton and T. A. Carlson: *"Precision Measurement of the Recoil Energy Spectrum from the Decay of ^{6}He"*. Phys. Rev. **132**, 1149 (1963).

[26] J. S. Allen, R. L. Burman, W. B. Herrmannsfeldt and P. Stähelin: *"Determination of the Beta-Decay Interaction from Electron-Neutrino Angular Correlation Measurements"*. Phys. Rev. **116**, 134 (1959).

[27] J. A. Behr, A. Gorelov, T. Swanson, O. Häusser, K. P. Jackson, M. Trinczek, U. Giesen, J. M. D'Auria, R. Hardy, T. Wilson, P. Choboter, F. Leblond, L. Buchmann, M. Dombsky, C. D. P. Levy, G. Roy, B. A. Brown and J. Diling: *"Magneto-optic Trapping of β-Decaying $^{38}K^m$, ^{37}K from an on-line Isotope Separator"*. Phys. Rev. Lett. **79**, 375 (1997).

[28] V. Egorov, Ch. Briançon, V. Brudanin, J. Dionisio, J. Deutsch, V. Gorozhankin, Yu. Gurov, R. Prieels, V. Sandukovsky, N. Severijns, M. Simoes, Yu Shitov, Ch. Vieu, V. Vorobel, Ts. Vylov, I. Yutlandov and Sh. Zaparov: *"Beta-Neutrino Angular Correlation in the Decay of ^{18}Ne"*. Nucl. Phys. A **621**, 745 (1997).

[29] C. J. Bowers, S. J. Freedman, B. Fujikawa, A. O. Macchiavelli, R. W. MacLeod, J. Reich, S. Q. Shang, P. A. Vetter and E. Wasserman: *"New Measurements of β-γ Directional Correlation in ^{22}Na"*. Phys. Rev. C **59**, 1113 (1999).

[30] R. B. Firestone: *"Table of Isotopes"* volume II. John Wiley & sons, inc. eighth edition (1996).

[31] T. Björnstad, M. J. G. Borge, P. Dessagne, R.-D. von Dincklage, G. T. Ewan, P. G. Hansen, A. Huck, B. Jonson, G. Klotz, A. Knipper, P. O. Larsson, G. Nyman, H. L. Ravn, C. Richard-Serre, K. Riisager, D. Schardt and G. Walter: *"Study of the Giant Gamow-Teller Resonance in Nuclear β-Decay: The case of ^{32}Ar"*. Nucl. Phys. A **443**, 283 (1985).

[32] M. J. G. Borge, P. Dessagne, G. T. Ewan, P. G. Hansen, A. Huck, B. Jonson, G. Klotz, A. Knipper, S. Mattsson, G. Nyman, C. Richard-Serre, K. Riisager and G. Walter: *"Study of the Giant Gamow-Teller Resonance in Nuclear Beta Decay: The Case of ^{33}Ar"*. Phys. Scr. **36**, 218 (1987).

[33] J. C. Hardy, J. E. Esterl, R. G. Sextro and J. Cerny: *"Isospin Purity and Delayed-Protron Decay: ^{17}Ne and ^{33}Ar"*. Phys. Rev. C **3**, 700 (1971).

[34] D. Schardt and K. Riisager: *"Beta-Neutrino Recoil Broadening in β-Delayed Proton Emission of ^{32}Ar and ^{33}Ar"*. Zeit. Phys. A **345**, 265 (1993).

[35] A. Honkanen, L. Axelsson, J. Äystö, M. J. G. Borge, B. Jonson, A. Jokinen, I. Martel, G. Martínez-Pinedo, I. Mukha, T. Nilsson, G. Nyman, B. Petersen, A. Poves, M. H. Smedberg, A. Teijeiro and O. Tengblad: *"Fine Structure in the Beta-Delayed Protron Decay of ^{33}Ar"*. Nucl. Phys. A **611**, 47 (1996).

[36] E. Hagberg, P. G. Hansen, J. C. Hardy, A. Huck, B. Jonson, S. Mattsson, H. L. Ravn, P. Tidemand-Petersson and G. Walter: *"Decay of a T_z= -2 Nucleus: Argon-32"*. Phys. Rev. Lett. **39**, 792 (1977).

[37] M. Langevin, A. C. Mueller, D. Guillemaud-Mueller, M. G. Saint-Laurent, R. Anne, M. Bernas, J. Galin, D. Guerreau, J. C. Jacmart, S. D. Hoath, F. Naulin, F. Pougheon, E. Quiniou and C. Détraz: *"Mapping of the Proton Drip-Line up to Z=20: Observation of the $T_z = -\frac{5}{2}$ Series ^{23}Si, ^{27}S, ^{31}Ar and ^{35}Ca"*. Nucl. Phys. A **455**, 149 (1986).

[38] H. O. U. Fynbo, L. AxelssonJ. Äystö, M. J. G. Borge, L. M. Fraile, A. Honkanen, P. Hornshøj, Y. Jading, A. Jokinen, B. Jonson, I. Martel, I. Mukha, T. Nilsson, G. Nyman, M. Oinonen, K. Riisager, T. Siiskonen, M. H. SmedbergO. Tengblad and F. Wenander: *"^{31}Ar Examined: New Limit on the β-Delayed Three-Proton Branch"*. Phys. Rev. C page 2257 (1999).

[39] E. Kugler, D. Fiander, B. Jonson, H. Haas, A. Przewloka, H. L. Ravn, D. J. Simon and K. Zimmer: *"The New CERN-ISOLDE on-line Mass-Separator Facility at the PS-Booster"*. Nucl. Inst. and Meth. B **70**, 41 (1992).

[40] T. Bjørnstad, E. Hagebø, P. Hoff, O. C. Jonsson, E. Kugler, H. L. Ravn, S. Sundell and B. Vosicki: *"Methods for Production of Intense Beams of Unstable Nuclei: New Developments at ISOLDE"*. Phys. Scr. **34**, 578 (1986).

[41] H. O. U. Fynbo: *"β-Delayed Two- and Three-Proton Emission from ^{31}Ar. First Results from the June 1997 Experiment"*. Status Report Århus University, Denmark (1997). *unpublished.*

[42] A. M. Litke and A. S. Schwarz: *"The Silicon Microstrip Detector"*. Scientific American page 56 (May 1995).

[43] PAW: *"Physics Analysis Workstation, An Introductory Tutorial"*. CERN Program Library Long Writeup Q121, CERN Geneva, Switzerland (1995).

[44] W. N. Lennard, H. Geissel, K. B. Winterbon, D. Phillips, T. K. Alexander and J. S. Forster: *"Nonlinear Response of Si Detectors for Low-Z Ions"*. Nucl. Instr. Meth. A **248**, 454 (1986).

[45] W. N. Lennard and K. B. Winterbon: *"Response of Silicon Detectors to ^1H and ^4He Ions"*. Nucl. Instr. Meth. B **24/25**, 1035 (1987).

[46] P. M. Endt: *"Energy Levels of A=21-44 Nuclei (VII)"*. Nucl. Phys. A **521**, 1 (1990).

[47] G. Hall: *"Semiconductor Particle Tracking Detectors"*. Rep. Prog. Phys. **57**, 481 (1994).

[48] T. Davinson, Department of Physics and Astronomy, University of Edinburgh: Privat communication (1998).

[49] J. Yorkston, A. C. Shotter, D. B. Syme and G. Huxtable: *"Interstrip Surface Effects in Oxide Passivated Ion-Implanted Silicon Strip Detectors"*. Nucl. Instr. Meth. A **262**, 353 (1987).

[50] J. F. Ziegler and J. P. Biersack: *"The Stopping and Range of Ions in Solids"*. Pergamon Press, New York (1985).

[51] C. S. Wu and S. .A. Moszkowski: *"Beta decay"*. Interscience (1966).

[52] T. D. Lee and C. N. Yang: *"Question of Parity Conservation in Weak Interaction"*. Phys. Rev. **104**, 254 (1956).

[53] C. S. Wu, E. Ambler, R. W. Hayward, D. D. Hoppes and R. P. Hudson: *"Experimental Test of Parity Conservation in Beta Decay"*. Phys. Rev. **105**, 1413 (1957).

[54] E. T. H. Clifford, E. Hagberg, J. C. Hardy, H. Schmeing, R. E. Azuma, H. C. Evans, V. T. Koslowsky, U. J. Schrewe, K. S. Sharma and I. S. Towner: *"The Decay of ^{20}Na"*. Nucl. Phys. A **493**, 293 (1989).

[55] M. Morita: *"Beta-Neutrino-Alpha Directional Correlation"*. Phys. Rev. Lett. **1**, 112 (1958).

[56] B. R. Holstein: *"Recoil Effects in Allowed Beta Decay: The Elementary Particle Approach"*. Rev. Mod. Phys. **46**, 789 (1974).

[57] E. T. H. Clifford, J. C. Hardy, H. Schmeing, R. E. Azuma, H. C. Evans, T. Faestermann, E. Hagberg, K. P. Jackson, V. T. Koslowsky, U. J. Schrewe, K. S. Sharma and I. S. Towner: *"Kinematic Shifts in the β-Delayed Particle Decay of ^{20}Na and the β-ν Angular Correlation"*. Phys. Rev. Lett. **50**, 23 (1983).

[58] P. M. Endt: *"Supplement to Energy Levels of A=21-44 Nuclei (VII)"*. Nucl. Phys. A **633**, 1 (1998).

[59] R. D. Macfarlane, N. S. Oakey and R. J. Nickles: *"Beta-Neutrino Correlations and Longitudinal Nuclear Aligment in the Decay of ^{20}Na"*. Phys.Lett. B **34**, 133 (1971).

[60] G. Nyman, R. E. Azuma, P. G. Hansen, B. Jonson, P. O. Larsson, S. Mattsson, A. Richter, K. Riisager, O. Tengblad and K. Wilhelmsen: *"The Beta Decay of ^9Li to Levels in ^9Be"*. Nucl. Phys. A **510**, 189 (1990).

[61] C. A. Barnes, W. A. Fowler, H. B. Greenstein, C. C. Lauritsen and M. E. Nordberg: *"Nature of the ^8Li Beta-Decay interaction"*. Phys. Rev. Lett. **1**, 328 (1958).

[62] R. D. McKeown, G. T. Garvey and C. A. Gagliardi: *"Beta-Alpha angular correlations in mass 8"*. Phys. Rev. C **22**, 738 (1980).

[63] S. Baker and R. D. Cousins: *"Clarification of the use of Chi-Square and Likelihood Functions in Fits to Histograms"*. Nucl. Instr. Meth. A **221**, 437 (1984).

[64] R. A. Paddock: *"(p,t) Reaction on Even-Even N=Z Nuclei in the $2s1d$ Shell"*. Phys. Rev. C **5**, 485 (1972).

[65] H. Yokota, K. Fujioka, K. Ichimaru, Y. Mihara and R. Chiba: *"The T=1, Isospin Triplet States in A=30 Nuclei"*. Nucl. Phys. A **383**, 298 (1982).

[66] B. Petersen: *"The Decay of ^{31}Ar. The Analysis of the Gamma-Ray Spectrum"*. Master's thesis Århus University, Denmark (1996). *unpublished.*

[67] E. Kuhlmann, W. Albrecht and A. Hoffmann: *"The γ-Ray Decay of Levels in ^{30}S"*. Nucl. Phys. A **213**, 82 (1973).

[68] D. R. Goosman and D. E. Alburger: *"New Aluminum Isotope; Mass and β Decay of the $T_z = 5/2$ Nuclide ^{31}Al and the Mass of ^{34}P"*. Phys. Rev. C (1973).

[69] B. H. Wildenthal: *"Empirical Strengths of Spin Operators in Nuclei"*. Prog. Part. Nucl. Phys. **11**, 5 (1984).

[70] A. I. Boothroyd, J. Markey and P. Vogel: *"Status of the Standard Vector—Axial-vector Model for Nuclear Beta Decay"*. Phys. Rev. C **29**, 603 (1984).

[71] E. G. Adelberger: *"Improved Limits on Scalar Weak Couplings"*. Phys. Rev. Lett. **70**, 2856 (1993).

[72] Y. Jading and K. Riisager: *"Systematic Errors in χ^2-Fitting of Poisson Distibutions"*. Nucl. Instr. Meth. A **372**, 289 (1996).

[73] W. T. Eadie, D. Drijard, F. E. James, M. Roos and B. Sadoulet: *"Statistical Methods in Experimental Physics"*. North-Holland, Amsterdam, London (1971).